HIGH QUALITY 3D SHAPE RECONSTRUCTION VIA DIGITAL REFOCUSING AND PUPIL APODIZATION IN MULTI-WAVELENGTH HOLOGRAPHIC INTERFEROMETRY

by

Li Xu

A dissertation submitted in partial fulfillment
of the requirements for the degree of
Doctor of Philosophy
(Mechanical Engineering)
in The University of Michigan
2012

Doctoral Committee:

Professor Jun Ni, Chair
Professor Jeffrey A. Fessler
Professor L. Jay Guo
Associate Professor Wei Lu

Dedication

To my family and my faithful friends

Acknowledgements

My deepest gratitude is to my advisor, Professor Jun Ni, who has guided me both in academic research and human dignity. His patience and wisdom helped me overcome many difficult situations during the past 4 years. While encouraging me to grow as a specialist and independent thinker within my research field, his mentorship has been paramount in guiding me with profound philosophy of how to become an engineering expert of respectable personality.

I would like to give my faithful thank to the School of Engineering at University of Michigan, especially the members of my doctoral committee, Professor Jeffrey A. Fessler, Professor Lingjie Guo and Professor Wei Lu, for their insightful input and thought-provoking discussions.

I would like to thank people from Coherix Inc. and Precision Engineering and Manufacturing Alliance (PEMA), especially Mike Mater and Carl Aleksoff, whose insights contribute significantly in my work.

My thanks also go to my comrades and colleagues at S.M. Wu Manufacturing Research Center, as well as in the “2 micron” ATP program, whose constructive criticisms and persisting efforts encourage me day and night.

Table of Contents

List of Figures

List of Tables

Abstract

Multi-wavelength holographic interferometry (MWHI) has good potential for evolving into a high quality 3D shape reconstruction technique. There are several remaining challenges, including 1) depth-of-field limitation, leading to axial dimension inaccuracy of out-of-focus objects; and 2) smearing from shiny smooth objects to their dark dull neighbors, generating fake measurements within the dark area. This research is motivated by the goal of developing an advanced optical metrology system that provides accurate 3D profiles for target object or objects of axial dimension larger than the depth-of-field, and for objects with dramatically different surface conditions.

The idea of employing digital refocusing in MWHI has been proposed as a solution to the depth-of-field limitation. One the one hand, traditional single wavelength refocusing formula is revised to reduce sensitivity to wavelength error. Investigation over real example demonstrates promising accuracy and repeatability of reconstructed 3D profiles. On the other hand, a phase contrast based focus detection criterion is developed especially for MWHI, which overcomes the problem of phase unwrapping. The combination for these two innovations gives birth to a systematic strategy of acquiring high quality 3D profiles. Following the first phase contrast based focus detection step, interferometric distance measurement by MWHI is implemented

as a next step to conduct relative focus detection with high accuracy. This strategy results in ±100mm 3D profile with micron level axial accuracy, which is not available in traditional extended focus image (EFI) solutions.

Pupil apodization has been implemented to address the second challenge of smearing. The process of reflective rough surface inspection has been mathematically modeled, which explains the origin of stray light and the necessity of replacing hard-edged pupil with one of gradually attenuating transmission (apodization). Metrics to optimize pupil types and parameters have been chosen especially for MWHI. A Gaussian apodized pupil has been installed and tested. A reduction of smearing in measurement result has been experimentally demonstrated.

Chapter 1

Introduction

1.1 Motivation

Digital holography (DH) has been recognized as an emerging interferometric imaging and testing technology for its non-contact, high accuracy, whole-field and high speed properties [Huang, 2006]. Applications of digital holography have been demonstrated in many fields, including biological sample imaging [Malkiel, 1999; Popescu, 2004], particle tracking and velocimetry [Adams, 1998; Kemper, 2009; Lebrun, 2003], surface shape measurement and tomography [Yamaguchi, 2006; Yu, 2009], and MEMS/MOEMS structure observation [Kebbel, 2001; Ferraro, 2005].

DH applying dual / multiple wavelengths has experienced substantial development in recent years. Kim reported improvement of axial resolution by conducting multi-wavelength interference in tomography [Kim, 1999]. Montfort et al. experimentally demonstrated the constructive effect of multiple complex waves at a selected plane, while destructive effect could be clearly observed at other planes within the axial extent determined by wavelength interval [Montfort, 2006]. Gass et al. proposed a novel noise reduction algorithm for reconstructing multi-wavelength topography [Gass, 2003]. A variety of methods have been developed to reduce

recording time, whose ultimate goal is to achieve real-time multi-wavelength holography [Zou, 1996; Kuhn, 2007; Rinehart, 2010]. Demonstrated applications of multi-wavelength digital holography (MDH) involve, for example, observing bio samples and bio structures [Kim, 2000; Khmaladze, 2008; Kuhn, 2009], contouring mechanical objects [Carl, 2009] and developing endoscopic equipment [Kandulla, 2004]. Among all these reported developments, a core advantage of MDH technology is that, by greatly expanding unambiguous range, phase wrapping problems can be overcome in practice.

In the field of metrology, the introduction of multi-wavelength technique into DH has greatly enlarged its absolute axial measurement range (commercially available at ±5mm), while preserving a high axial resolution up to micron level [Aleksoff, 2006]. Smoothness and continuity of the object to be measured is no longer indispensable, as it is in many single wavelength cases [Ferraro, 2005]. As a powerful surface quality monitoring tool, multi-wavelength holographic interferometry (MWHI) has demonstrated significant applications in auto industry [Huang, 2006]. A commercialized system has been developed for in-line, full surface inspection purpose (Coherix Inc.). Fig 1.1 shows a conceptual example of measuring a combustion chamber over cylinder heads with MWHI, which is proposed to monitor chamber volume variation among different parts for quality control purpose. Compared with traditional 3D metrology methods, MWHI's advantages are summarized in Fig 1.2.

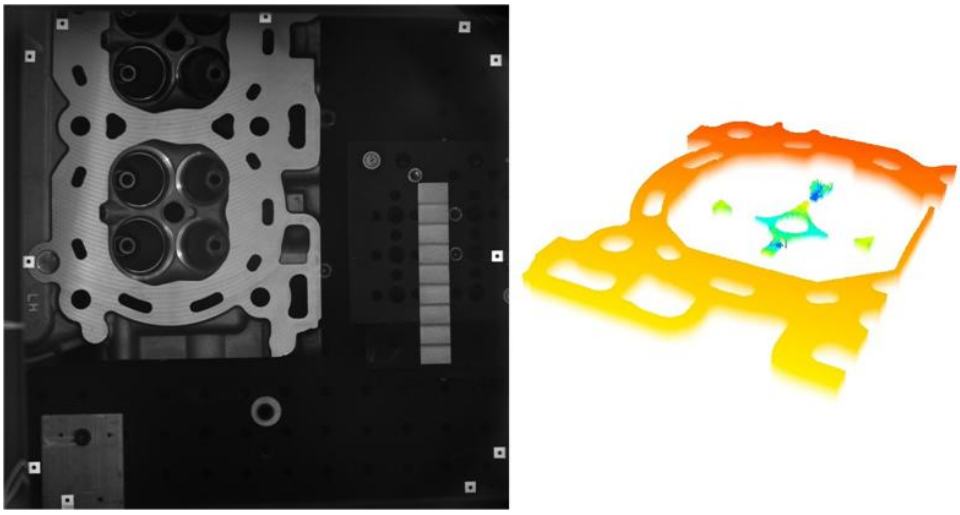

Fig 1.1 3D map of combustion chamber measurement

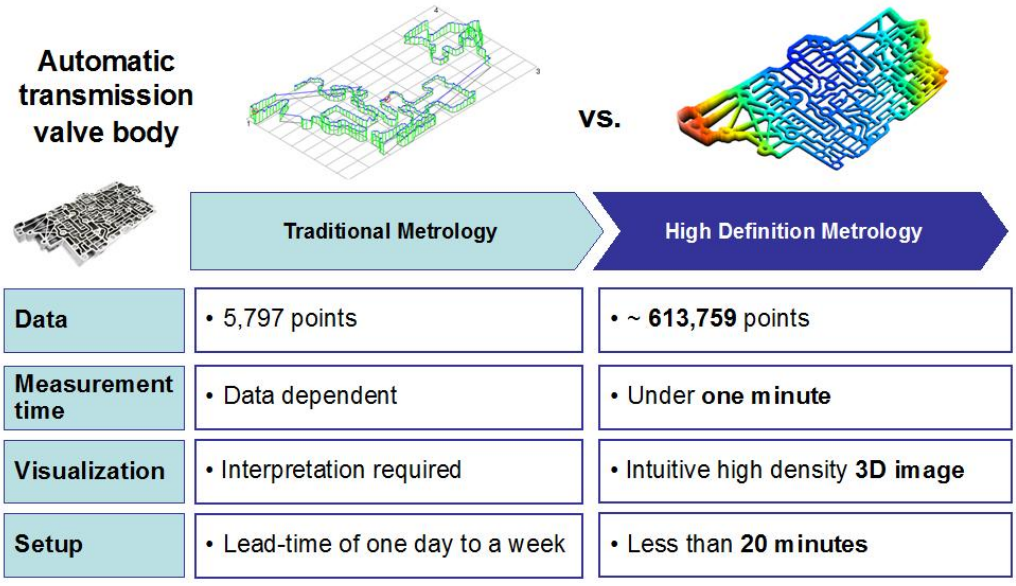

Fig 1.2 Advantages of MWHI (referred to as "High Definition Metrology") over traditional metrology methods (courtesy of Coherix. Inc.)

With the help of either wavelength monitoring equipment or real time calibration setup, MWHI with tunable laser source can reach an absolute axial range of over ±100 mm [Yu, 2011]. MWHI has been expected to reach an even larger unambiguous range by using advanced laser sources [Falaggis, 2009], which will definitely bring further inviting applications in the future.

One potential development of MWHI is to measure 3D shape of large-scaled objects with high precision, which is highly desirable in metrology. To achieve the goal, current MWHI technique is faced with two challenges. The first one is the depth-of-field limitation, leading to a consequential inaccuracy for out-of-focus objects. A second challenge is smearing from shiny smooth objects to their dark dull neighbors, which would result in fake measurements within the dark area, due to truncation effect by traditional hard-edged pupils.

A major challenge for further developing MWHI is that the technique depends on an image system to depict object profile, and thus axial measurement results are affected by the lateral imaging clarity, which is dependent on system's depth-of-field. Accurate 3D measurements can only be generated for those features within the depth-of-field. Once targets of interest are placed out-of-focus, their images may be blurred, resulting in inaccurate measurements. Fig 1.3 shows a penny and its in-focus vs. out-of-focus measurement results. It is obvious that the pillars are not visible when the penny is placed out of focus, and their 3D heights cannot be measured (more detailed descriptions in Chapter 2). In a more general case, for instance, over one machined part, there can be several separated surfaces of inspection interest. These targets can be far from each other in the axial direction, and thus not every one of them can be measured in-focus. Due to either measurement time restrictions or geometric structure limitations, mechanical refocusing is not always a viable solution. An advanced system is highly desired, that can measure multiple targets distributed in a relatively large height range in a single shot, while preserving high 3D measurement

accuracy for all targets.

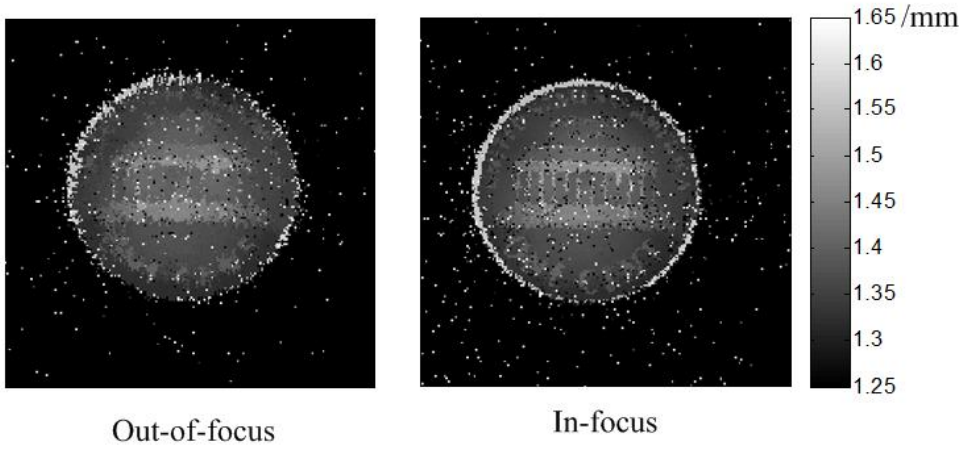

Fig 1.3 In-focus vs. out-of-focus measurement of a penny

Another challenge in current 3D profile measurement via MWHI derives from the difference in surface qualities of two laterally adjacent objects. In practice, the measurement of a dull rough surface often appears to be affected by its shiny smooth neighbor. As shown in Fig 1.4, gauge blocks of mirror-like surface quality are placed in the vicinity of a ground surface (Ra in the range of 8~16μm). From the MWHI measurement result, it can be observed that a large area of the ground surface is "measured" to be of the same height of its mirror-like neighbors.

This research is motivated by the goal of developing an advanced optical metrology system that provides accurate 3D profiles for target object or objects of axial dimension larger than the depth-of-field and for objects with dramatically different surface conditions. Digital refocusing is introduced as a solution to the first challenge, while pupil apodization is implemented to address the second one.

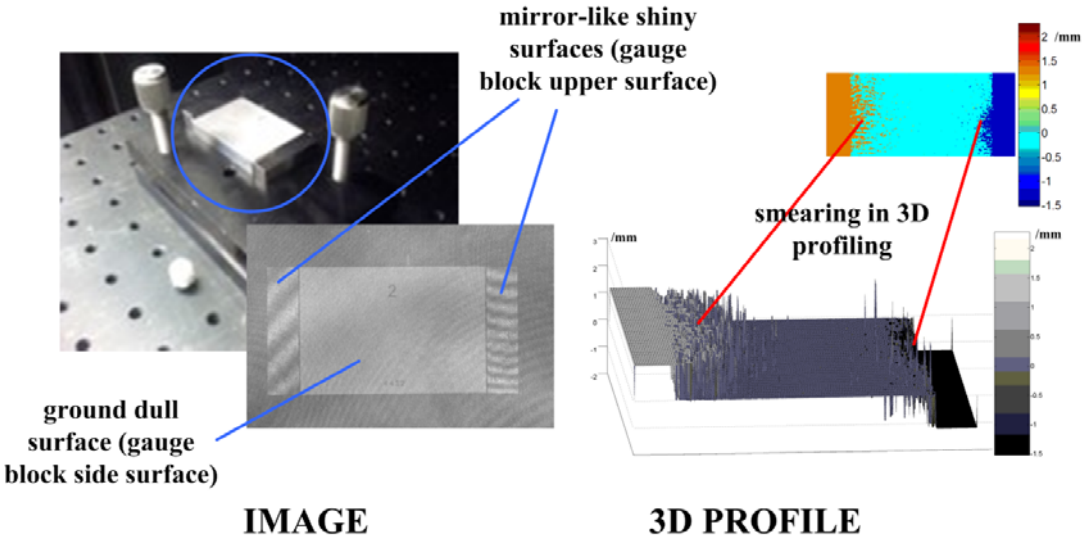

Fig 1.4 Observed measurement smearing from mirror-like (shiny/smooth) surfaces to ground (dull/rough) surface

1.2 Literature review

In this section, a brief literature review is provided to outline the current state-of-the-art in related fields and clarify the tasks of the proposed research.

1.2.1 Large range accurate axial information via digital refocusing

Researchers have long realized that with digital holography, optical information far away from the camera plane in a non-imaging system, or the focal plane in an imaging system, can be reconstructed by a computer [Gabor, 1948; Schnars, 1994(1); Yamaguchi, 1997; Adams, 1998; Hogenboom, 1998; Nilsson, 1998; Zhang, 1998; Cuche, 1999]. This idea has been applied in microscopy as a refocusing tool, for example, to determine the sizes and positions of small particles [Adams, 1998; Zhang, 1998], or to observe better resolved intensity images of magnified biological objects and resolution targets [Dubois, 1999; Yamaguchi, 2001]. In some early works,

reconstructions of phase information were also demonstrated, more or less as capability proofs, rather than useful information. Later publications have shown certain applications of phase information reconstruction [Dubois, 2006], for example, using sharp phase contrast, instead of vague intensity contrast, to observe transparent biological examples. However, the accuracy of the reconstructed phase / axial information was still not emphasized, as there was no clear application for it.

Applications of accurate phase information via holographic refocusing are rarely reported until recently [Ferraro, 2005; Colomb, 2010]. The reason why it is not highlighted as much as in other interferometric metrology or phase contrast imaging cases, probably lies in the following fact that in majority cases without multi-wavelength technology, the absolute axial measurement range would be limited, so that only slowly and continuously varying axial structures can be measured via interferometric based technology. Usually, such structures are either simple in lateral dimensions, or having limited axial range and thus stays within the system's depth-of-field. In either of such cases, refocusing will not provide evident advantages.

By greatly expanding axial measurement range, MWHI breaks the requirement of smoothness and continuity of the object to be measured. Large objects with complicated 3D shapes are targeted, and phase accuracy during refocusing emerges as a new topic worth studying.

A first task of the proposed research is that, with multi-wavelength technology, the accuracy of reconstructed phase and axial information via digital refocusing will

be highlighted, since it is directly related to height measurement result from a metrology point of view. The traditional digital refocusing formula needs to be modified to meet robustness requirement against realistic wavelength uncertainty.

1.2.2 Advanced focal plane detection criterion for multi-wavelength synthetic 3D map

One key parameter in MWHI refocusing is the refocus distance between current imaging plane and the best focal plane. In many practical applications, this distance is not given. A focus detection criterion should therefore be employed to determine the location of the best focal plane.

Applications of focus detection in holographic imaging have been reported in quite a few articles, most of which use amplitude maps. Typical focus detection criteria are based on a series of reconstructed frames along the axial direction, and determine the best focused frame via a certain kind of "sharpness indicator". The sharper the image is, the closer its position to the best focus. Commonly adopted indicators include: entropy indicator [Gillespie, 1989], variance indicator [Groen, 1985; Ozgen, 2004; Sun, 2004; Thelen, 2005], spectral based indicator [Langehanenberg, 2008], gradient based indicator [Yu, 2001], and correlation coefficient indicator [Choo, 2006; Yang, 2007; Yang, 2008]. Although computationally intensive, Fresnelet based decomposition has also been introduced to construct sharpness metric, which depends on the sparsity of its wavelet coefficients to determine the best focal plane [Liebling, 2004].

The majority of focus-finding applications are based on amplitude analysis, even though in many cases it is phase contrast that is actually of interest. As reported in [Dubois, 2006], the best focus with sharpest phase contrast could be determined, when it corresponded to the lowest amplitude contrast. Such objects were referred to as "pure phase" objects. In more comprehensive cases, however, when phase contrast is not strongly dependent on amplitude contrast, the task of determining "the sharpest phase contrast plane" is difficult.

Examples of using phase information for refocusing purpose have been limited to a few simple cases, such as MEMS structures reported in [Ferraro, 2005; Colomb, 2010], where refocusing distances were determined by counting phase wrapping fringes. This method can be performed only when the object slope is continuous and gentle, so that phase fringes are continuous and clear enough to be counted. It is even believed that phase contrast is not usable for more complicated focus-finding purposes, such as step like height structures, since jumps at 2π caused by phase wrapping would be misunderstood as real sharp features [Langehanenberg, 2008]. Phase unwrapping algorithms are available, yet they are not satisfactory solutions, since unwrap errors would significantly reduce the accuracy of the detection.

MWHI needs phase contrast based focus detection because dependence between amplitude contrast and phase contrast can be fairly loose due to flatness and roughness variation. Thus indirect focus detection criteria are not always a viable choice. At the same time, fringe-counting strategy is also made impossible due to

discontinuities and shape-complexity of surfaces.

A second task of the proposed research is to set up a new phase contrast based focus detection criterion, by taking the advantage of MWHI. The major challenge of achieving reliable focus detection lies in how to separate useful phase contrast information from its noisy background, including salt-and-pepper noise and measurement uncertainty. Instead of detecting a maximum sharpness point as many previous criteria do, the criterion developed here aims to find a zero-crossing point that indicates the best focus plane.

1.2.3 Multi-target / multi-range method for high precision 3D shape reconstruction

To depict multiple targets distributed in a wide axial range, or a single object with axial dimension larger than the depth-of-field, in high accuracy within one shot, a multi-target/multi-range height map merging algorithm should be developed. The targets of interest should be segregated based on their measured height, then refocused respectively to their best focal planes, and finally merged back to form a high precision 3D shape result.

There have been several attempts of sectioning and merging holographic images. For example, Cuong et al [Cuong, 2005; Javidi, 2006; Cuong, 2007] previously proposed independent component analysis (ICA) [Hyvarinen, 2000; Hyvarinen, 2007] or discrete wavelet transform (DWT) based image fusion algorithms in processing

out-of-focused holographic images. Their methods incurred the problem of blurring, since their merged image had to, more or less, take out-of-focus images into account. This will bring inaccuracy in metrology and thus is not considered as a viable solution. Another series of worthy attempts were performed on optical scanning holography [Kim, 2006; Zhang, 2008; Zhang, 2009], which modeled the task of sectioning as an inverse problem. Wiener filtering or iterative algorithms were implemented. Remarkable segregation effect of pure amplitude targets was achieved experimentally. However, their method only worked for amplitude recovery. Holographic phase information was lost during their signal collection step.

The idea of separating the whole image into small blocks and applying focal detection algorithm one by one was described in [Mc Elhinney, 2005] and [Tachiki, 2008]. Focal measurement algorithms were applied to each of the individual blocks, the best focal positions were calculated, and then blocks from their best focal positions could be used to stitch an extended focus image (EFI). However, this idea has significant difficulties in getting correct best focal distances for featureless blocks.

With extended absolute height range generated by MWHI, the target segregation step can be replaced by generating a preliminary 3D height map. And then the conjunctive locations of other features within the valid height range will be available for the refocusing operation. The uniqueness of this idea is that the relative refocusing distance is based on measured height via MWHI, rather than estimated focal distance, which highly depends on surface feature sharpness.

A third task of the proposed research is to develop an effective algorithm to reconstruct high precision 3D shapes from multi-target / multi-range 3D measurement.

1.2.4 Pupil apodization to restrain smearing in MWHI

Fig 1.4 illustrates that there is stray light from the shiny surfaces to their neighboring area, which carries phase information leading to smeared measurement. Based on the mathematical modeling of facets, it is concluded that the stray light originates from truncation effect by hard-edged pupil, and a transmission attenuated pupil (apodized pupil) would likely be effective to reduce this effect.

The idea of apodization has been proposed previously. A comprehensive review of this subject can be found as early as in 1964 [Jacquinot, 1964]. In recent years, the majority of reported applications of apodization in optics have been focused on astronomical observation [Guyon, 2003; Carlotti, 2008; Martinez, 2010], especially the detection of exoplanets with strong star background [Nisenson, 2001]. Other reported applications of apodization include atmospheric remote sensing [MacDonald, 2002], confocal microscopy [Martinez-Corral, 2003], and optical data storage [Canales, 2009], to name a few. One significant difference is that, generally speaking, asymmetric shaped pupils are not applicable in MWHI 3D profile reconstruction, as they are in astronomical detection tasks [Kasdin, 2003]. This is because that, rather than isolated in dark background, the observation targets (facets) are now densely distributed within the whole field of view. As the observation task is to characterize

the property of each facet or group of facets correctly, an edge-free, azimuthally symmetric pupil is highly desired, for the sake of generating a diffraction-limited point spread function (PSF).

Another key difference in MWHI is that, as an interferometric system, it is now phase (rather than amplitude or irradiance) of the captured holograms that carries useful information (object height). This difference in signal of interest leads to a change in metrics while evaluating performances of pupil functions.

A fourth task of the proposed research is that, based on mathematical analysis, we can explain the phenomena of smearing from shiny smooth surface to dull rough surface. New metrics for replacing hard-edged pupil with apodized pupil have been proposed, to restrain smearing effect in interferometric imaging systems. It is, to the best of the author's knowledge, the first time that pupil apodization has been implemented in a MWHI imaging system.

1.3 Research objective and frameworks

The objective of this study is to develop an advanced optical metrology system that can provide 3D measurement results with both extended measurement clarity range and high axial accuracy, for target object or objects of axial dimension larger than the depth-of-field, typically in a decimeter-level axial range. Multi-wavelength holographic refocusing will be used to overcome out-of-focus blurring and consequential degradation of 3D clarity, while pupil apodization will be the tool to

address the smooth-rough smearing phenomena. These studies are presented through chapters 2 to 5. Refocusing related studies are discussed in chapters 2 to 4. Chapter 5 is on pupil apodization.

In Chapter 2, the methodology of reconstructing an out-of-focus multi-wavelength holographic measurement result has been proposed, with defocusing distance d assumed to be known. Limitations of the maximum out-of-focus range are derived, and the influence of system noise is also discussed. As a metrology technology, accuracy and repeatability are compared between the reconstructed measurement results and in-focus measurement results. Results by a mechanical contact profiler of micron level accuracy are provided as the reference.

In Chapter 3, the study focuses on how to find an estimation criterion for defocusing distance d when it is not provided. Differences among criteria are compared. A new criterion based on synthetic height information is proposed and its performance is demonstrated. Possible further developments of the criterion are discussed.

In Chapter 4, a more general case is addressed, where an object with axial dimension larger than the depth-of-field, or multiple objects of different axial positions are to be measured simultaneously. The strategy to generate high precision 3D profile via relative locating is suggested. First locate one of the targets in the axial direction, and then locate all other targets within the absolute height measurement range around it. Refocusing distance of the other targets will be calculated based on

MWHI measured height, rather than applying refocusing criterion to these targets respectively. The strategy is designed to be especially beneficial for weak feature or featureless targets. Preliminary performance evaluation experiment has been demonstrated. Possible future improvements of the technology are discussed.

Chapter 5 first describes a reflection model of facets, based on which the smearing phenomenon is explained conceptually. Mathematical derivation of the reflective imaging process is then provided. Metrics selected for interferometric system have been discussed, in comparison with those used in astronomical observation tasks. Performance of different kinds of pupils has been simulated for the selected metrics, and type and size of the preferred apodized pupil are optimized. Experimental results have shown evident restrain of smearing effect, validating the proposed solution.

Chapter 6 provides a summary of the proposed study of the dissertation as well as the possible future works and applications.

The appendix discusses a first thought about how further enhancement of lateral resolution may be achieved via “sub-pixel” shifting and deconvolution in MWHI has been briefly discussed, which can be a potential future work.

Chapter 2

Multi-wavelength Holographic Refocusing with Known Best Focal Plane

2.1 Introduction

Multi-wavelength holographic interferometry (MWHI, briefly reviewed in 2.2.1), has been implemented in the auto industry as a surface quality investigation technique. Its experimental absolute height measurement range is around ±5mm currently with micron level accuracy. With the help of either wavelength monitoring equipment or real time calibration setup, MWHI with tunable laser source can reach an absolute axial range of over ±100 mm [Yu, 2011]. The technique has a very promising future of having much larger potential unambiguous measurement range [Falaggis, 2009], if advanced laser sources are implemented. Another highlight of this technology is that it has an evident speed advantage over traditional investigation method, such as coordinate measurement machine (CMM). The state-of-the-art technology can typically finish investigating a 288mm by 288mm area within 1 minute (Coherix Inc.). Because of this, MWHI can achieve 100% measurement practically, which is highly demanded by in-line statistical quality control.

As discussed in the previous chapter, the inspection quality of MWHI is limited

by the system's depth-of-field, in a way similar to many other imaging techniques. Once targets of interest are located out of focus, they may be heavily blurred and hence result in inaccurate measurements. The value of digital refocusing lies in the fact that not every surface can be measured in-focus. Due to either measurement time restrictions or geometric structure limitations, mechanical refocusing is not always viable, especially for machined individual parts that have several separated surfaces of inspection interest.

In this chapter, digital holographic refocusing is proposed as a solution to out-of-focus investigation in practical cases. Digital refocusing (reviewed in 2.2.2) has been applied in microscopy mainly for improving amplitude imaging quality [Zhang, 1998; Dubois, 1999; Yamaguchi, 2001; Dubois, 2006]. Here in MWHI, with multiple wavelengths adopted, it is proposed to acquire superior measurement clarity range and consequentially more accurate height results of a 3D object. For all wavelengths involved, this task requires a high accuracy of holographic phase reconstruction, as well as robustness towards wavelength error.

In what follows the principles of both MWHI imaging and digital refocusing are briefly described, followed by discussion and simulation on maximum refocusing distance limitation and reconstruction robustness with respect to wavelength error. Experimental result with refocusing distance of 200mm is achieved with measurement repeatability of 2μm, proving that the proposed process is sufficiently robust to noise in practical cases. The work presented in this chapter has been summarized in [Xu,

2012(1)].

2.2 Literature review

2.2.1 Multi-wavelength holographic interferometry (MWHI)

In the field of interferometry, the idea of applying multi-wavelength to achieve extended absolute height measurement range has long been recognized [Cheng, 1985]. The key advantage of using more than one wavelength over traditional single wavelength interferometry [Bruning, 1978; Koliopoulos, 1981; Schwider, 1983] is that the absolute height measurement range can be enlarged. For example, if two wavelengths λ_1 and λ_2 are implemented, the synthetic wavelength of the measurement system is $\frac{\lambda_1\lambda_2}{|\lambda_1-\lambda_2|}$, larger than either of λ_1 and λ_2, and thus can measure a longer range without incurring a 2π phase wrapping problem. Theoretically, two close enough wavelengths are sufficient to measure any height. However, noise comes into play and error amplification effect leads to poor measurement precision [Cheng, 1984]. Thereby more wavelengths are introduced to guarantee a good precision while achieving large height measurement range.

Many experimental MWHI systems are based on multiple independent laser sources [Daendliker, 1995; Kumar, 2008; Mann, 2008; Lee, 2009]. Precision measurement capability up to 1.5m has been experimentally achieved by using three stabilized lasers [Lewis, 1994]. However such optical setups are complex. And the freedom of selecting certain wavelengths combination is limited. In recent years, with

the development of laser technology, tunable lasers are more often employed [Lu, 2002; Aleksoff, 2006]. Commercially available external cavity diode laser, for example, New Focus Velocity™ Widely Tunable Lasers, provides a tuning range of several-tens of nanometers, with a tuning resolution of approximately 0.02nm. Typical height measurement range of systems applying this kind of laser source is around tens of millimeter level, with micron level uncertainty. Its affordable cost with relative high performance provides MWHI systems more chance in commercialized products. The development of future MWHI will benefit from technology that can generate larger number of wavelengths with finer frequency interval, such as the technology of optical frequency comb lasers [Jin 2006; Kim, 2009; Wang, 2010].

2.2.2 Digital holographic refocusing

The idea of digital holographic refocusing originates from the basic purpose of holography: reconstruct the object field from the recorded interference phase [Schnars, 2002]. The development of computer technology and charge coupled device (CCD) sensors makes it possible to process holographic information completely via numerical calculation. There are mainly two types of reconstruction algorithms. The Fresnel approach, as proposed by [Schnars, 1994(2)], requires a reduction of image size with longer reconstruction distance, and hence limits the resolution of reconstruction. The convolution approach [Demetrakopoulos, 1974], on the other hand, always keeps the same size in the reconstruction series. Thereby the convolution approach is commonly adopted in digital holographic reconstruction.

After the idea of holographic microscopy was proposed by Haddad et al [Haddad, 1992], people realized that with digital reconstruction, accurate mechanical adjustment to find the focal plane is no longer necessary, since image at any distance can be numerically calculated. Applications of digital refocusing have been demonstrated, to achieve sharp contrast images of resolution targets and bio objects [Zhang, 1998; Yamaguchi, 2001], and to track small particles and living cells [Dubois, 1999; Langehanenberg, 2009] based on clarity.

2.3 Principles of MWHI and digital refocusing

2.3.1 MWHI imaging

MWHI imaging generates a set of holograms, each of which is of a different wavelength for the same object. A typical system arrangement is shown in Fig 2.1. A wavelength tunable laser (New Focus, TLB-6316, 838nm~853nm wavelength range) serves as the coherent light source. Its output is separated into a reference beam and an object beam. The reference beam contains a controllable phase shifter to generate phase shifted interferograms. In the object beam, part to be measured (object), parabolic mirror (for off-axis aberration correction purpose) and lens, and the camera (Kodak, KAI-4021, 2048 by 2048 pixels) form a reflective imaging system.

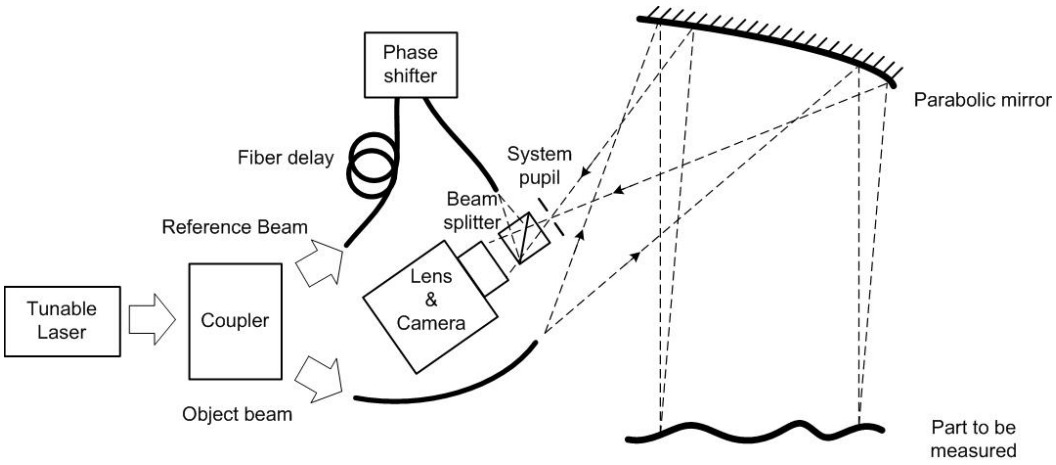

Fig 2.1 Optical arrangement of a typical MWHI imaging system

For each wavelength λ, its hologram can be generated by applying phase shifted interferometry (PSI) to every point over the whole field of view [Carre, 1966; Bruning, 1974]: Interferograms captured by CCD can be expressed as [Aleksoff, 2006]:

$$I(\varphi) = I_{obj} + I_{ref} + 2\sqrt{I_{obj} I_{ref}} \cos[(\gamma_{obj} - \gamma_{ref}) - \varphi] \tag{2.1}$$

where I_{obj} / γ_{obj} and I_{ref} / γ_{ref} stands for the intensity / phase of the object and reference beam, respectively. φ is a phase shift term generated by the phase shifter. The phase difference term (γ_{obj} - γ_{ref}) physically results from the optical path difference H between the object and reference beams:

$$\gamma_{obj} - \gamma_{ref} = 2\pi \frac{H}{\lambda} = 2n\pi + \theta \tag{2.2}$$

where n is an integer, and θ is the residual phase angle ranging from $-\pi$ to π. θ can be deduced from phase shifted interferograms $I(\varphi_q)$ [Schodel, 2002; Bothe, 1997]. In a general case, if the phase shift step intervals are all taken to be $2\pi / Q$, i.e., φ_q=0,

$2\pi/Q$, $4\pi/Q$, …, $2(q-1)\pi/Q$, …, $2(Q-1)\pi/Q$, then [Howard W. Sams & Co. Engineers, 1975]

$$\theta = \text{atan}\,2\left(\frac{\sum_{q=1}^{Q} I(\varphi_q)\sin(2(q-1)\pi/Q)}{\sum_{q=1}^{Q} I(\varphi_q)\cos(2(q-1)\pi/Q)}\right) \tag{2.3}$$

where atan2 is a four-quadrant inverse tangent function in accordance with the definition in MATLAB. For example, if φ is set to be 0, π/2, π and 3π/2, then [Dubois, 1999]:

$$\theta = \text{atan}\,2\left(\frac{I(3\pi/2)-I(\pi/2)}{I(0)-I(\pi)}\right) \tag{2.4}$$

which is a commonly adopted form of PSI. The calculated hologram of wavelength λ can then be represented by a complex field:

$$E(x,y) = 2\sqrt{I_{obj}(x,y)I_{ref}}\,e^{i\theta(x,y)} \tag{2.5}$$

where $2\sqrt{I_{obj}(x,y)I_{ref}}$ is the amplitude term and $\theta(x,y)$ is the phase term for each pixel of the camera.

In a single wavelength case, due to the periodicity of the cosine function in Eq. 2.1, H remains undefined to the additive 2nπ as shown in Eq. 2.2. The unambiguous measurement range of object height (axial distance) h, which equals to half of H in the shown system, is thereby limited to λ/2. Multi-wavelength technology is employed to overcome this phase wrapping problem. For the same h to be measured, if multiple

pairs of λ_p and θ_p (footnote p denotes different wavelengths) are known, a Fourier transform based axial distance scanning envelope function [Aleksoff, 2006]:

$$S(h) = \left| \frac{1}{P} \sum_{p=1}^{P} \exp[j(4\pi \frac{h}{\lambda_p} - \theta(\lambda_p))] \right| \tag{2.6}$$

can be depicted for each and every point over the whole field of view, in order to deduce the correct value of h, which is consistent with the highest peak position of S(h). The relation between axial measurement accuracy and the selection of wavelengths λ_p is still being studied [Falaggis, 2009; Towers, 2004], which in general indicates that the selection of wavelength shift steps, as well as the accuracy of the wavelength settings, plays a key role. Experimentally, applying 14 selected wavelengths ranging from 838 to 853nm with pm level accuracy would result in over ±100mm unambiguous measurement range [Yu, 2011].

2.3.2 Digital refocusing

Similar to single wavelength holographic imaging, MWHI imaging of an out-of-focus object would result in blurred details. According to the Fresnel diffraction theorem [Born and Wolf, 1999], for a certain wavelength λ, light propagation from an out-of-focus plane to the camera can be divided into two successive processes (as shown in Fig 2.2): first, free space propagation from the out-of-focus plane to the in-focus plane; and secondly, an imaging process just the same as in-focus imaging. The task of digital refocusing is to back calculate the complex optical field at the out-of-focus plane, based on that at the in-focus plane.

Relation between the two complex fields is mathematically expressed by the Kirchhoff–Fresnel equation [Dubois, 1999]:

$$E_2(x',y') = \exp(-jkd)\,\mathcal{F}^{-1}_{x',y'}\{\exp[\frac{jkd\lambda^2}{2}(u^2+v^2)]\times[\mathcal{F}^{+1}_{u,v}E_1(x,y)]\} \qquad (2.7)$$

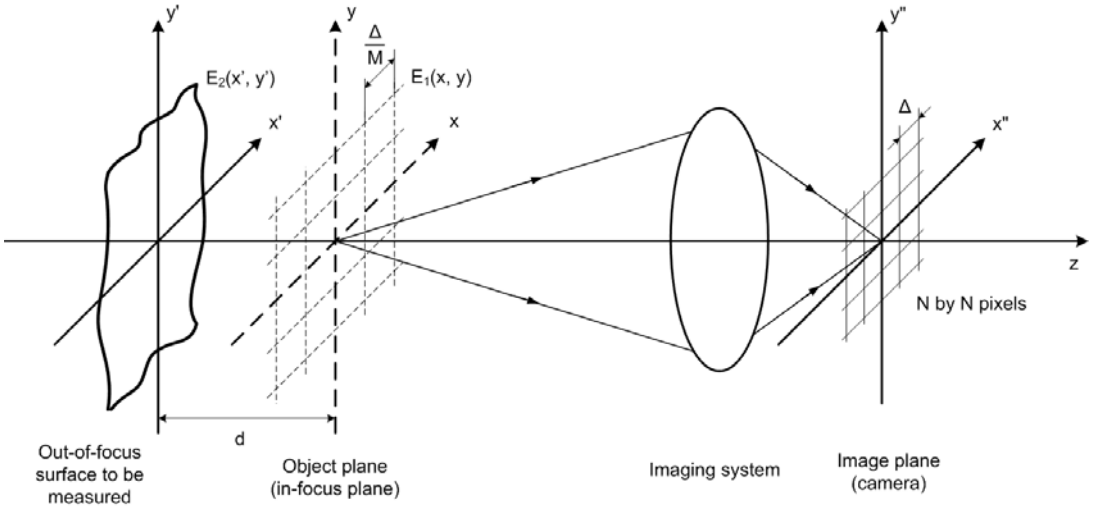

Fig 2.2 Coordinate system for digital refocusing

where $E_2(x',y')$ and $E_1(x,y)$ stands for the out-of-focus and in-focus complex hologram respectively (Fig 2.2). d is the distance between the planes. k is wave number, which equals to 2π/λ. u and v are spatial frequencies along x and y axis, respectively. $\mathcal{F}^{\pm1}_{\eta,\xi} f(\alpha,\beta)$ denotes 2D Fourier and inverse Fourier transform:

$$\mathcal{F}^{\pm1}_{\eta,\xi} f(\alpha,\beta) = \int_{-\infty}^{\infty}\int_{-\infty}^{\infty} \exp[\mathrm{m}\, j2\pi(\alpha\eta+\beta\xi)]\, f(\alpha,\beta)\, d\alpha\, d\beta \qquad (2.8)$$

Eq. 2.7 can be viewed as a multiplication operation in frequency domain, which is equivalent to convolution in space domain. It will have a numerically convenient discrete expression by setting

$$x' = \frac{X'\Delta}{M}, \quad y' = \frac{Y'\Delta}{M}$$
$$x = \frac{X\Delta}{M}, \quad y = \frac{Y\Delta}{M}$$
$$u = \frac{UM}{N\Delta}, \quad v = \frac{VM}{N\Delta}$$

in which the total field of view contains N by N pixels. Δ is the pixel spacing interval distance, M is the magnification of the imaging system, X', Y', X and Y are dimensionless quantities that all range from 0 to N-1. Discrete values U and V also range from 0 to N-1. The resultant discrete form of Eq. 2.7 is

$$E_2(\frac{X'\Delta}{M}, \frac{Y'\Delta}{M}) = \exp(-j\frac{2\pi d}{\lambda}) \sum_{X,Y,U,V=0}^{N-1} \frac{1}{N^2} E_1(\frac{X\Delta}{M}, \frac{Y\Delta}{M}) \times$$

$$\times \exp[j\frac{\pi\lambda d M^2}{N^2\Delta^2}(U^2+V^2)] \times \exp\{-j\frac{2\pi}{N}[(X-X')U+(Y-Y')V]\} \quad (2.9)$$

2.4 Estimation and Simulation

There are two key factors that need to be estimated before experimental work: First, the maximum refocusing distance d_{max}, which indicates a theoretical upper limit of the capability of digital refocusing; secondly, sensitivity of the phase terms to wavelength errors, $\delta\theta_p/\delta\lambda_p$, which indicates the robustness of the refocusing process. In what follows, numerical calculations of the factors are based on the same set of parameters as the experimental system.

2.4.1 Estimation of d_{max}

Eq. 2.9 places a theoretical limitation on the maximum reconstruction distance d [Dubois, 1999]. If the maximum phase shift caused by the quadratic term in Eq. 2.9

between two successive pixels exceeds 2π, or equivalently, exceeds π in either x or y direction, unwrapping errors are introduced and the phase information will not be reconstructed correctly. Therefore,

$$\frac{\pi\lambda d M^2}{N^2\Delta^2}[U_{\max}^2-(U_{\max}-1)^2]\le\pi \tag{2.10}$$

Since U_{max}=N-1≈N,

$$d\le\frac{N\Delta^2}{2\lambda M^2}=d_{\max} \tag{2.11}$$

Eq. 2.11 shows that d_{max} is inversely proportional to M^2, the square of magnification of the imaging system. This means that a broader field of view (a smaller magnification) can lead to a larger refocusing range. In our system, where N=2048, Δ=7.5μm, λ≈850nm, the M —— d_{max} relationship is shown in Fig 2.3. When M=1/20, d_{max} can be as large as 27.1m.

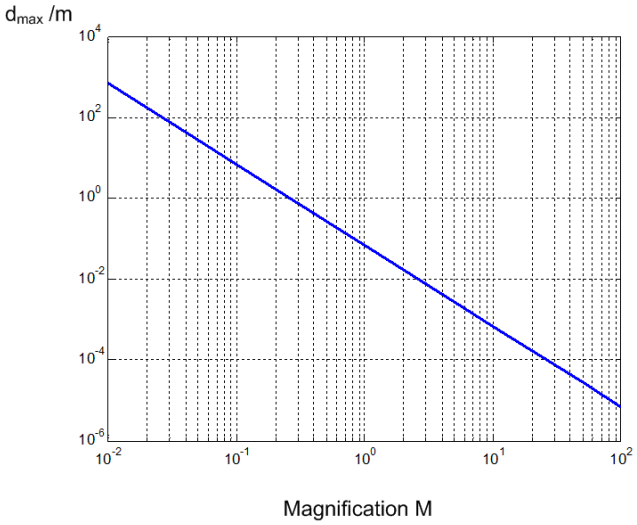

Fig 2.3 Maximum refocusing distance d_{max} and magnification (N=2048, Δ=7.5μm, λ=850nm)

2.4.2 Estimation of $\delta\theta_p/\delta\lambda_p$

Eq. 2.9 is theoretically correct. However, it is impractical to apply it directly in MWHI imaging, since it is very sensitive to wavelength errors $\delta\lambda_p$.

The influence of $\delta\lambda$ over reconstructed complex optical field can be separated into two parts: a constant part over the whole field of view and a location-dependent varying part. In Eq. 2.9, the former part is from the exponential term outside the summation:

$$\exp(-j\frac{2\pi d}{\lambda})$$

and the latter part comes from inside the summation:

$$\exp[j\frac{\pi\lambda dM^2}{N^2\Delta^2}(U^2+V^2)]$$

The magnitude of the first order derivatives of phase over wavelength in the above two parts are,

$$\left|\frac{\partial(-\frac{2\pi d}{\lambda})}{\partial\lambda}\right| = \left|\frac{2\pi d}{\lambda^2}\right| \tag{2.12}$$

and

$$\left|\frac{\partial[\frac{\pi\lambda dM^2}{N^2\Delta^2}(U^2+V^2)]}{\partial\lambda}\right| = \left|\frac{\pi dM^2}{N^2\Delta^2}(U^2+V^2)\right| < \left|\frac{2\pi dM^2}{\Delta^2}\right| \quad \text{(since U,V<N)} \tag{2.13}$$

respectively. Substituting system parameters into Eq. 2.12 and Eq. 2.13, it then comes out that the constant phase shift is significant, while the location-dependent phase shift is trivial towards wavelength variation. Assuming a 10pm wavelength error occurs, due to evident magnitude difference between d and λ, error in the constant phase shift can be as large as $7.5\times10^{6}\pi$; while in the location-dependent phase part, the introduced error is no more than $2.5\times10^{-2}\pi$.

In a single wavelength interference map, constant phase shift over the whole field of view usually will not make a difference. Nevertheless, it should be taken special care of while combining multiple wavelengths together. Since the magnitude by Eq. 2.12 is gigantic, after phase wrapping, an arbitrary phase shift ζ_p, ranging from $-\pi$ to π, will be added to each of the out-of-focus phase term θ_p. This will break the mathematical base of axial distance scanning in Eq. 2.6, which depends on the inter-relationship among θ_ps to deduce the correct distance. After digital refocusing with Eq. 2.9, deduced h may jump evidently from one value to another, rather than within a predictable tolerance range based on the range of wavelength errors. Thus, the constant phase part has to be eliminated from Eq. 2.9 to protect measurement accuracy of the phase/axial distance reconstruction.

This elimination will not affect clarity enhancement by digital refocusing. Physically, $\exp(-j2\pi d/\lambda)$ represents a plane wave propagating along the axial direction. It contains no lateral information and is thereby irrelevant towards clarity

reconstruction. In other words, no difference will be observed if x or y coordinates vary in Fig 2.2. Instead of Eq. 2.9,

$$E_2(\frac{X'\Delta}{M},\frac{Y'\Delta}{M}) = \sum_{X,Y,U,V=0}^{N-1} \frac{1}{N^2} E_1(\frac{X\Delta}{M},\frac{Y\Delta}{M}) \times$$

$$\times \exp[j\frac{\pi\lambda d M^2}{N^2\Delta^2}(U^2+V^2)] \times \exp\{-j\frac{2\pi}{N}[(X-X')U+(Y-Y')V]\} \quad (2.14)$$

will be used as a practical refocusing equation.

The refocusing and reconstruction process to enlarge measurement clarity range beyond the depth-of-field for out-of-focus features in MWHI imaging can be summarized as follows:

- Capture multiple interferograms for each wavelength λ_p
- Calculate the individual out-of-focus holograms, based on Eq. 2.3
- Digital refocus the holograms, using Eq. 2.14
- Axial distance scanning to reconstruct 3D map from the refocused holograms, based on Eq. 2.6

The terminology "interferogram" here means one intensity map captured by the CCD camera with respect to one phase shifter value of a single wavelength. It is in the form of Eq. 2.1. On the other hand, "hologram" here means the calculated complex optical field of the wavelength. It can be expressed in the form of Eq. 2.5. For a certain wavelength λ_p, since PSI need multiple phase shifts to derive θ_p, it will have multiple interferograms, but only one hologram.

2.4.3 Numerical Simulation

To further illustrate the validity of Eq. 2.14, simulated measurements of a 160-pixel by 160-pixel plate have been numerically demonstrated in Fig 2.4 (only the central 100 by 100 pixels are shown). In the original test plate shown in Fig 2.4a, the word "UMICH" is 2.3874 mm above its background. Tilting of 60 arc seconds in the x direction and 30 arc seconds in the y direction is carried out, to imitate a realistic case. System magnification M is set to be 1/20. 14 wavelengths, ranging from 838 to 853nm, are selected for the refocusing and reconstruction process. Wavelength errors are randomly selected within $\pm$10pm. Fig 2.4b shows a single-wavelength "ideal" (in-focus, zero phase noise) phase map of this test plate. Then the test plate is set 150mm out of focus. Fig 2.4c shows one of the out-of-focus phase maps, which has $\pm$2.5º random phase noise. 3D map reconstruction is done by scanning a range from 0 to 3mm, with a step size of 10μm. Without digital refocusing, the synthesized 3D map is shown in Fig 2.4d, in which out-of-focus blur plays an obvious destructive role. After refocusing by either Eq. 2.14 or Eq. 2.9, reconstruction results are shown in Fig 2.4e and Fig 2.4f, respectively. 3D map in Fig 2.4e is generated by Eq. 2.14, which is in good agreement with the original test plate. For comparison, Fig 2.4f is one typical result by using Eq. 2.9 for refocusing. The grey bar near the graph indicates that the axial location of the word is "measured" to be 2.49mm lower than the background. It can then be concluded that, while Eq. 2.14 keeps good tolerance towards wavelength error, applying Eq. 2.9 will make measurement results deviate strongly. In one thousand such tests, 938 results of Eq. 2.9 gave incorrect results,

while all the results generated via Eq. 2.14 are correctly measured to a level of better than 10μm.

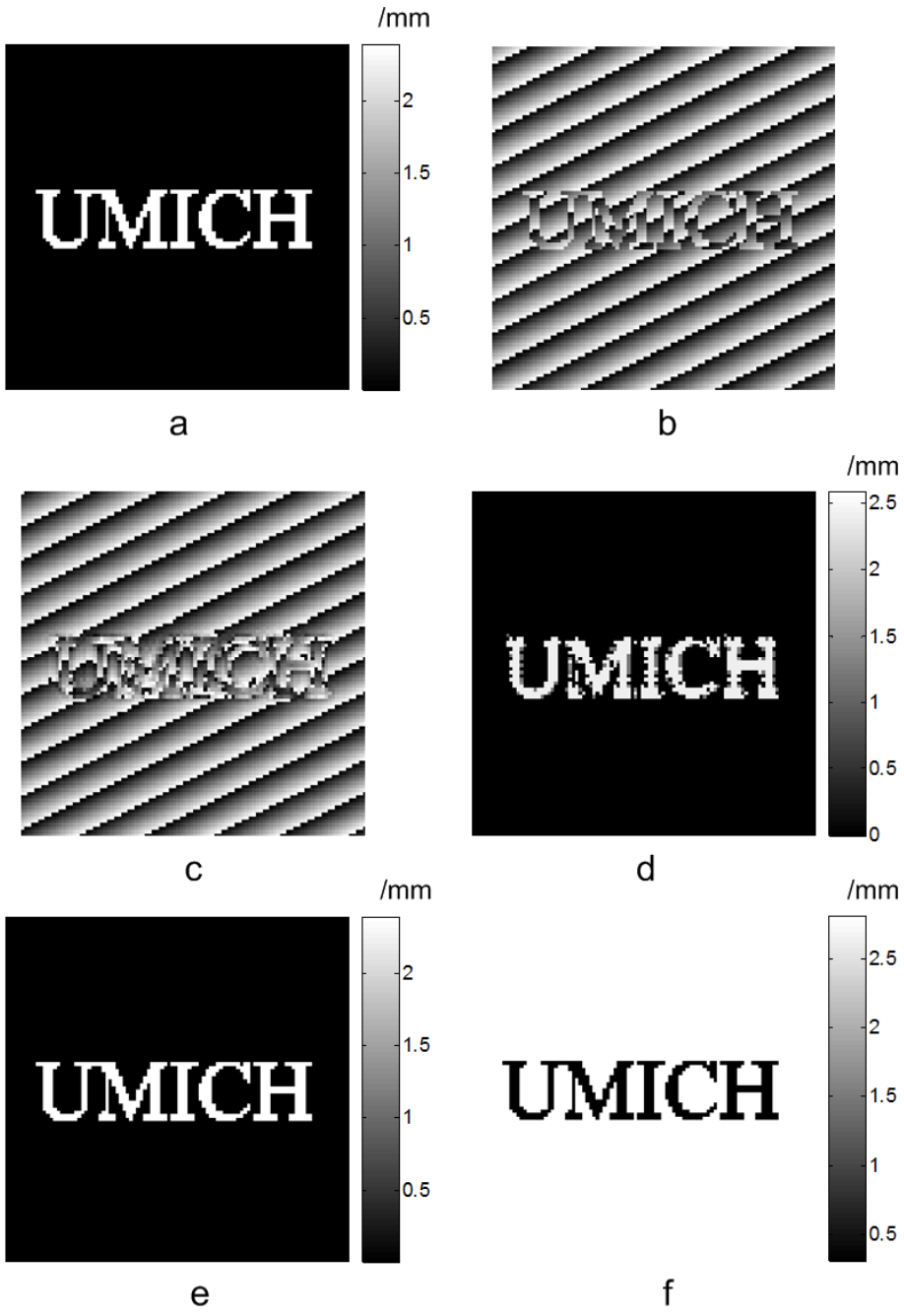

Fig 2.4 Simulation "UMICH"
a) original test plate; b) ideal in-focus phase map; c) out-of-focus noisy phase map; d) blurred out-of-focus 3D map; e) refocused 3D map using Eq. 2.14; f) refocused 3D map using Eq. 2.9

2.5 Experiment & Discussion

Wavelength λ	14 selected wavelengths, ranging from 838 to 853nm		
Number of pixels N×N	400×400 (200×200 is shown)	Pixel interval Δ	7.5 μm
Magnification M	1/20	Refocusing distance d	200mm
h scan range	-1mm ~ 3mm	h scan step size	1 μm

Table 2.1 Experimental parameters

The performance of digital refocusing in MWI imaging is tested by the following experiment. A measurement has been carried out to test a penny over a stainless steel flat plate, as shown in Fig 2.5. Related system parameters are provided in Table 2.1. In order to reduce phase noise, careful steps have been taken. The system is placed on air-cushioned table, isolating units from sudden shocks and high frequency vibrations. The optical path is sealed and the laser source is air-conditioned, to prevent influences from air perturbation and temperature change. Furthermore, the entire hologram-capturing process is programed, which can be completed within 30 seconds. By reducing capturing time, influence of environmental variation is minimized to the best of our capability.

The penny and the plate are first placed in focus and measured. Then they are mechanically set out focus by 200mm and measured again. In the reconstruction step, the axial distance scanning range is set to be -1 to 3mm, with step size of 1μm. At each position, 5 measurement results have been recorded to evaluate measurement accuracy and repeatability. The results are median-filtered to remove salt-and-pepper

noise. Mean and standard deviation σ of 5 measures are calculated based on filtered data for each point. Differences between captured results and median filtered results are recorded. If a difference exceeds ±3σ, the point would be considered as corrupted by salt-and-pepper noise.

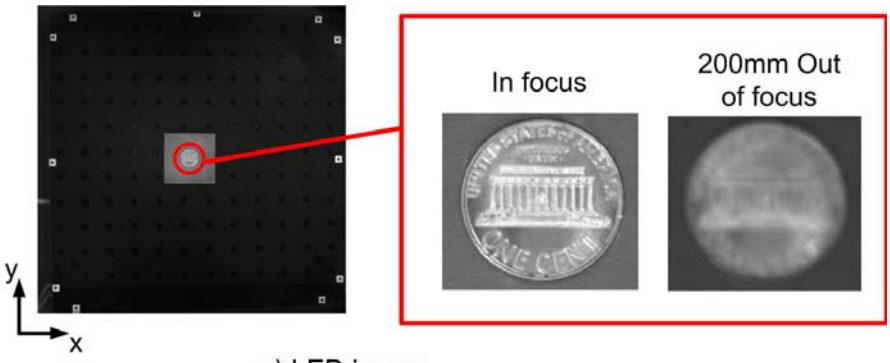

a) LED image

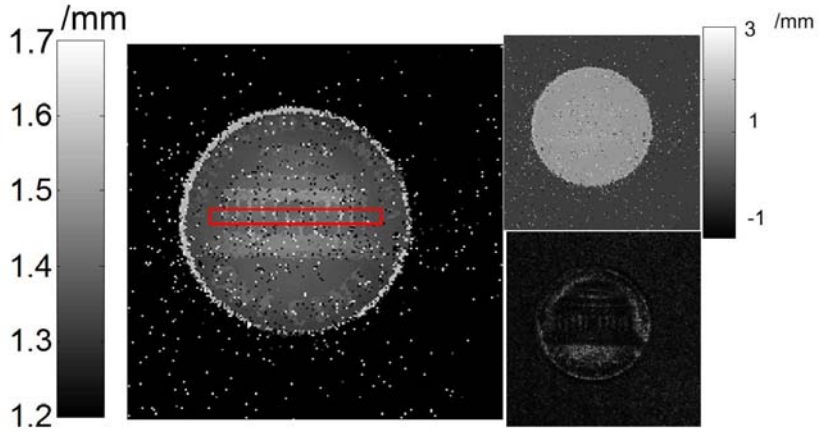

b) In-focus

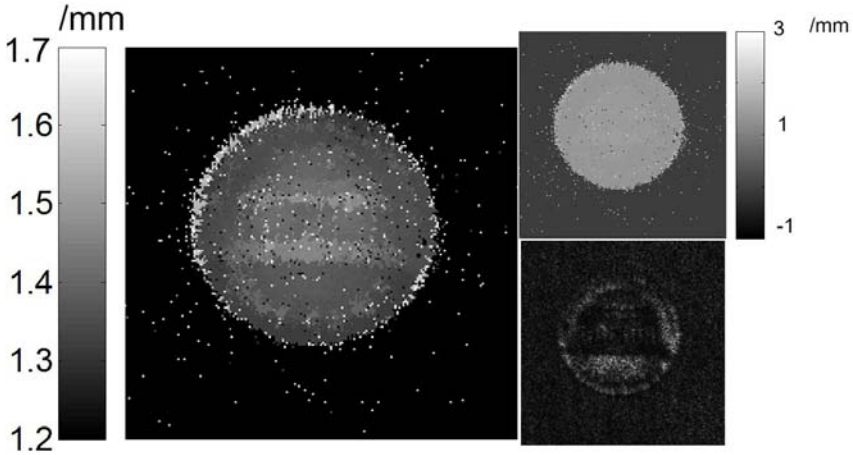

c) Out-of-focus

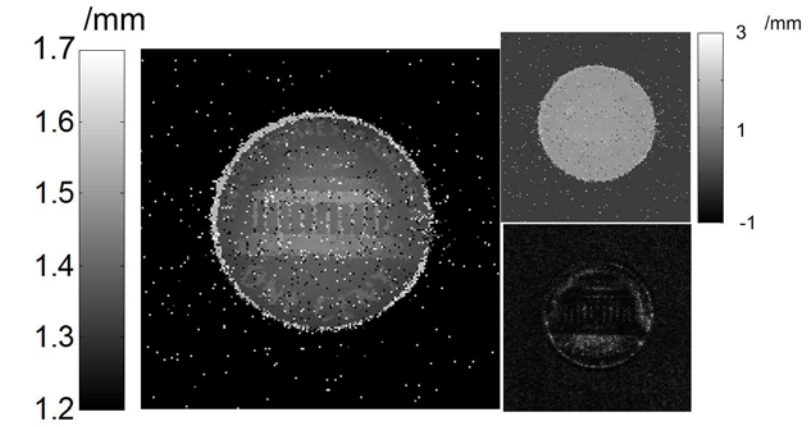

d) Refocused using Eq. 2.14

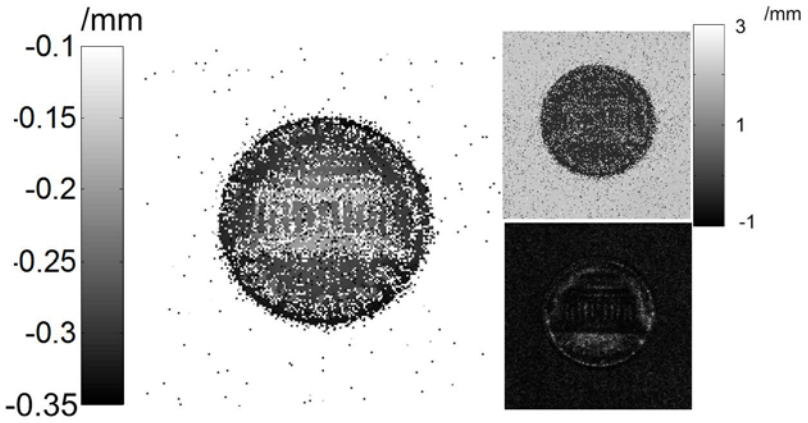

e) Refocused using Eq. 2.9

Fig 2.5 Experimental measurement of a penny: a) LED images of: whole field-of-view, in-focus penny and out-of-focus penny; b) in-focus measurement; c) out-of-focus measurement; d) refocused measurement using Eq. 2.14; e) refocused measurement using Eq. 2.9. In sub-picture b to e: left, re-ranged 3D map to show penny features; upper-right: original 3D map scaled from -1mm to 3mm; lower-right: example hologram (amplitude only)

Fig 2.5a shows LED illuminated images of the penny in the whole field-of-view. It contains no 3D information. Fig 2.5 b to e shows the in-focus (Fig 2.5b), out-of-focus (Fig 2.5c) and refocused 3D maps (Fig 2.5d by Eq. 2.14, Fig 2.5e by Eq. 2.9) in grey scales, respectively. In Fig 2.5 b to d, features within the range from 1.200mm to 1.700mm above the steel plate are emphasized. It can be observed that details of the Lincoln Memorial shown in Fig 2.5b are not observable in Fig 2.5c. By

doing digital refocusing with Eq. 2.14, most of the details can be recovered in Fig 2.5d from out-of-focus blur. In addition, as shown in Fig 2.5e, if Eq. 2.9 is employed, not only does the resultant 3D map show incorrect profile (penny surface lower than the steel plate surface), but it contains much more corrupted points as well.

By using Eq. 2.14, good consistency of 3D measurement results is preserved. This can be observed in Fig 2.6, where the heights of the centers of the pillars are measured within the rectangle-marked area in Fig 2.5b. The dashed green line in Fig 2.6a stands for the result of a mechanical profiler (Form Talysurf 50, Taylor Hobson Precision), whose lateral resolution is 10μm and height measurement accuracy is 0.1μm. In comparison, the black dotted line is for direct out-of-focus measurement (Fig 2.5c), which can show only a general trend of the surface, without any detailed information. In Fig 2.6b, Blue 'x' dots and error-bars are for in-focus results. The result after digital refocusing is represented by red 'o' dots and error-bars in Fig 2.6c. Considering the low sampling rate for features over the penny (the width of one pillar typically covers 1 to 3 pixels), the mean positions of the refocused measurement show good accuracy.

Since the standard deviations of both the in-focus and re-focused measurement results are around 2μm (as shown by 10 times scaled error-bars in both Fig 2.6b and c), a good repeatability of the refocusing process is shown. The refocusing process is not adding uncertainty to the measurement results and thereby indicates robustness from realistic noise.

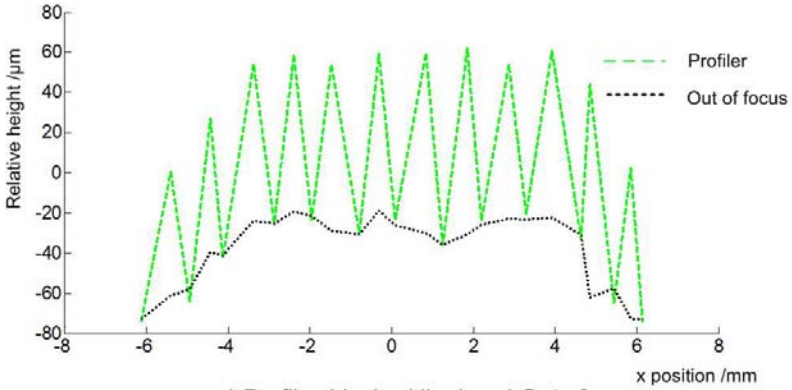

a) Profiler (dashed line) and Out of focus (dotted line)

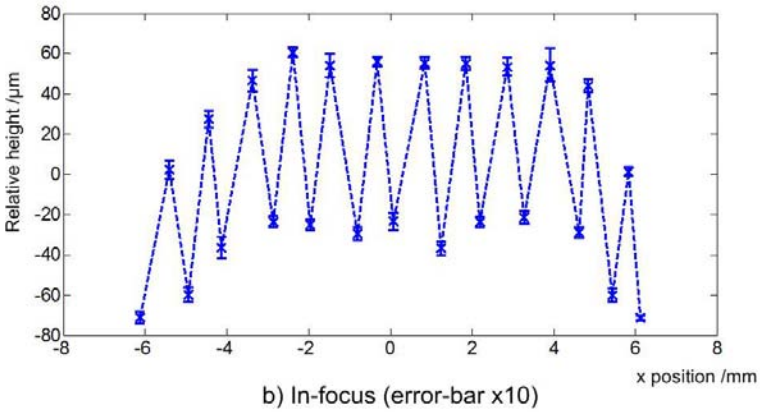

b) In-focus (error-bar x10)

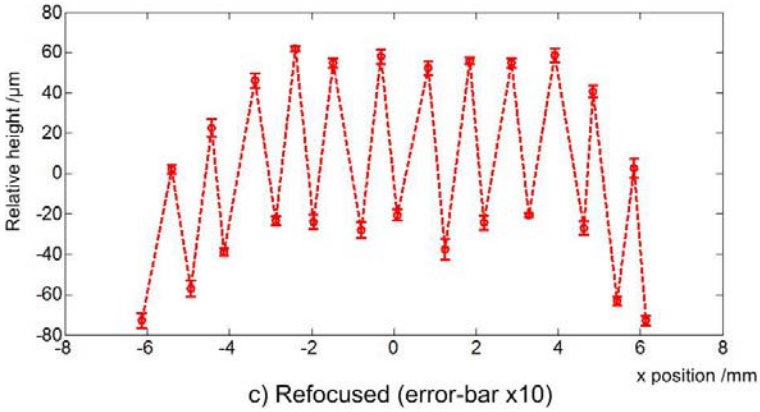

c) Refocused (error-bar x10)

Fig 2.6 Height measurement result

2.6 Conclusion

When features of interest are placed out-of-focus in realistic applications for a MWHI system, the technology of digital refocusing is proposed in this chapter as a solution to improve 3D profiling. The key advantage is that, not only can the

technology enlarge measurement clarity range beyond the depth-of-field, but it can keep a good accuracy and repeatability for the refocused results as well. This solution is especially effective when a large field of view is to be investigated, since small magnification guarantees wider refocusing range and superior robustness towards random wavelength error. Satisfying repeatability is achieved in the 200mm refocusing experiment, indicating that the proposed process is sufficiently robust to noise in practical cases. Future work to further improve the MWHI refocusing technique lies in studies of wavelength combination to enhance robustness towards random wavelengths fluctuation.

Chapter 3

Advanced Focal Plane Detection Criterion for Multi-wavelength Holographic Refocusing

3.1 Introduction

Chapter 2 showed that out-of-focus measurements can be reconstructed and reach an enhanced clarity as if they were in-focus. Refocusing distance d is a critical parameter in the reconstruction process. It was given as a prior knowledge in the previous chapter.

In practical metrology cases, due to the uncertainty of parts to be measured, d can be unknown. On such occasions, a series of reconstructions need to be made at different axial positions. Based on certain sharpness criterion, the best focal plane should be selected among them.

Previous studies in best focal plane detection for digital holography (reviewed in section 3.2.1) were mainly based on amplitude information of the holograms. Phase information is rarely used, as it contains 2π phase wrapping which might be misinterpreted as sharp structures [Langehanenberg, 2008]. Even for those images that can be numerically phase unwrapped, criteria based on phase information are not

recommended because of potential unwrapping errors.

In MWHI, since absolute measurement range is greatly expended, phase wrapping is no longer a critical obstacle. Phase information can be used for sharpness indicators. There are two specific challenges in focal-plane detection of synthetic 3D maps/images:

On the one hand, there are evident "salt-and-pepper" noise points in synthetic 3D images. Since the generation of 3D height from individual phases is a peak-finding process, small phase error can result in significant height bias. The incorrect height value of one pixel is irrelevant from all other pixels, and its value is randomly distributed within the whole measurement range. The noisy pixels can be misunderstood as sharp features observed via refocusing. In this chapter, traditional median filter is implemented to deal with "salt-and-pepper" noise. However, it tends to remove too much detailed information via smoothing (reviewed in section 3.2.2), which corresponds to the sensitivity of sharpness detection, and thereby it is subject to improvement in future works.

On the other hand, in 3D profiling, small lateral (x-y) features (details) to be observed are sometimes not sufficiently evident in the axial (z) dimension, comparing with their background. This is different from those in astronomy, or many other image-deblurring problems, where 2D details can give sharp contrast to their background [Campisi, 2007]. In practical metrology cases, needle like objects are less likely to be imaged from their ends, especially when lateral resolution is insufficient.

The insignificance of detailed features makes refocusing improvement in clarity almost unperceivable. For display purpose, we restrict artificially the observing gray level range to a narrow fraction of the whole measurement range in Chapter 2. The whole range result of an out-of-focus and refocused penny is shown in Fig 3.1. The difference over penny surface is almost unobservable, which indicates that the information useful for focal plane finding is weak.

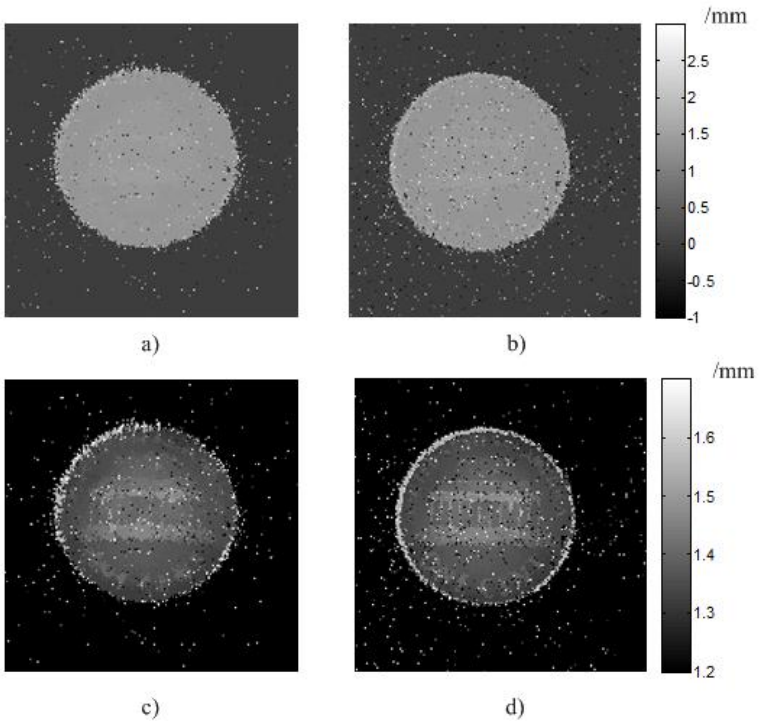

Fig 3.1 Effect of scale range on feature visibility
a) and c) are out of focus 3D maps, b) and d) are in focus 3D maps; a) and b) range from -1mm to 3mm, c) and d) range from 1.2mm to 1.7mm

In this chapter, a new phase contrast based focus detection criterion has been proposed by taking the advantage of MWHI. Instead of detecting a maximum sharpness point as many previous criteria do, the developed criterion aims to find a zero-passing point, which is experimentally effective. A step-by-step derivation of the

criterion is provided. Measurement examples of step-like 3D structures are given, demonstrating possible applications of this criterion. The work presented in this chapter has been summarized in [Xu, 2011].

3.2 Literature review

3.2.1 Existing focus detection criteria

Focus detection criteria to select the best focused image from a series of images are usually based on image sharpness. In the field of image processing, commonly applied sharpness indicators include, for example, gradient computation [Yu, 2001], self-entropy [Gillespie, 1989], variance distribution [Groen, 1985; Ozgen, 2004; Sun, 2004] and Laplace operator [Groen, 1985; Sun, 2004].

In processing single-wavelength holographic images, most criteria are based on amplitude contrast. [Ma, 2004] based their criterion on maximizing the local variance of speckles. A computationally intensive criterion has been proposed by introducing Fresnelet [Liebling, 2003], and basing the sharpness metric on the sparsity of the wavelet coefficients and their energies [Liebling, 2004]. Benefiting from the invariance of energy and amplitude integration, [Dubois, 2006] summarized two amplitude-based criteria for two special cases of holographic focal finding, namely, the object was either pure amplitude or pure phase.

While working on digital holographic microscopy images, Langehanenberg et al. [Langehanenberg, 2008] recently proved that a criterion based on weighted spectral

analysis (SPEC) outperformed many other methods. By applying this criterion, a series of studies have been demonstrated in imaging, tracking life cells [Kemper, 2007; Langehanenberg, 2007; Remmersmann, 2009] and capturing surface topography [Liu, 2009(1) ; Liu, 2009 (2) ; Wang, 2009].

Another type of sharpness indicator has been proposed by Choo et al [Choo, 2006; Yang, 2007; Yang, 2008]. Instead of directly finding sharpness of a single image, the symmetry of images on opposite sides of the best focal plane was emphasized. They employed correlation coefficient to measure the degree to which the images were similar, and determined the best focal plane in the middle of the two most similar images.

3.2.2 "Salt-and-pepper" noise filtering

There are many filters developed to remove salt-and-pepper noise. Traditional median filter [Nodes, 1982] and its modifications [Pitas, 1990; Ko, 1991] are most commonly employed. However, they modify both noisy and noise-free pixels. Such approaches are likely to blur the original image. Advanced filters are developed to first separate noisy and noise-free pixels, and then do the filtering. Impulse detectors are commonly applied in these filters. In [Zhang, 2002], for example, one-dimensional Laplacian operators were used to create four convolutions, and their minimum absolute value was obtained to detect noisy pixels. Many others, such as fuzzy impulse detector [Luo, 2006(1)], differential rank detector [Aizenberg, 2004], decision-based algorithm detector [Srinivasan, 2007], alpha-trimmed mean-based

[Luo, 2006(2)], had also been proposed.

Having identified noisy pixels, a second step is to construct a noise removal strategy to fulfill certain functions. For example, in [Chan, 2005] and [Chen, 2008], the idea of edge-preserving was highlighted. By setting different routines based on directional differences around the corrupted pixel, [Chen, 2008] found an effective way to protect image sharpness from salt-and-pepper noise.

3.3 Focus detection for MWHI imaging

Object axial dimension h derived in Eq. 2.6 originates from the phase term $\cos[(\gamma_{obj} - \gamma_{ref}) - \varphi]$ of the captured interferograms, rather than the amplitude term $2\sqrt{I_{obj} \mathrm{g} I_{ref}}$ in Eq. 2.1. The focus detection criterion derived below for 3D map h(x,y) is thereby based on phase contrast, which is a significant difference of the proposed work in this chapter from its predecessors.

A major difficulty of setting up a practical focus-finding criterion on 3D maps is that the useful height contrast information is relatively weak, comparing with its background noise. Take Fig 3.1 as an example, the reconstructed features over the penny are typically around 100μm in height, 1/40 of the experimental axial dimension scanning range (-1mm to 3mm). Their occupied area is less than 5% of the whole field of view (200 by 200 pixels). Therefore, an effective feature extraction and enhancement process should be the core part of the criterion.

After generating refocused 3D maps $h(x, y; d)$ with a series of refocusing

distance d along z axis, the proposed focus detection criterion can be conducted in the following steps:

- Impulse detector based noise filtering
- Finding the difference between two reconstructed 3D maps of certain interval
- Eliminate measurement uncertainty
- Feature enhancement
- Implement differential indicator $\eta\{d\}$

Step 1: Impulse detector based noise filtering

Fig 3.1 demonstrates obvious salt-and-pepper noise. This is introduced by practical small errors of λ_ps and $\theta(\lambda_p)$s. As we are taking a real-time measurement of wavelengths experimentally, the main contributor of errors in λ_ps is considered to be rounding errors. On the other hand, the causes of errors of $\theta(\lambda_p)$ are manifold, including vibration, temporal air turbulence along optical path and speckle induced degradation, etc. Laser speckles due to the roughness of the target object surface randomly degrade intensity modulation, on which we depend to derive $\theta(\lambda_p)$ in Eq. 2.3. Since the axial distance scanning process (Eq. 2.6) is ill-posed, small differences of λ_p and $\theta(\lambda_p)$ in $(4\pi h/\lambda_p - \theta(\lambda_p))$ cause unpredictable peak position shift, which indicates an unpredictable measurement error. When errors of λ_p and $\theta(\lambda_p)$ are random small values, this kind of measurement error should be point-by-point / pixel-by-pixel: one outlier point will not affect its neighbors. Under such conditions, impulse detector based noise filtering should be effective. The filtered 3D maps are noted as

$\overline{h}(x, y; d)$.

Step 2: Finding the difference between two reconstructed 3D maps of certain interval

Instead of focusing on the information of a single frame, the proposed criterion here uses two reconstructed frames: the subtraction of two 3D maps with a certain interval, named "3D difference map", is employed. Assuming the frame interval of the reconstruction series is δd, then the difference interval between two frames is usually selected to be l times of δd for convenience, and the resulting 3D difference map:

$$\overline{h}\_diff(x, y; d, d - l\delta d) = \overline{h}(x, y; d) - \overline{h}(x, y; d - l\delta d) \tag{3.1}$$

This operation is more or less similar to the correlation coefficient (CC) indicator [Choo, 2006], as it can be viewed as a kind of "robustness enhancement" procedure: the larger the interval is, the more evident the difference between two frames should be. The idea of using difference instead of the frames themselves has a physical meaning in MWHI imaging: An out-of-focus 3D map provides a "blurred version" of a correct 3D profile. Subtraction between reconstructed frames is then just a height difference calculation. The majority points in the two 3D maps should be similar. After subtraction, they should thereby be around zero. Only those points along the edges of features remain obviously different from zero in a 3D difference map.

Step 3: Eliminate measurement uncertainty

In the previous step, although the majority points are of similar heights in the two frames, their difference may not be exactly zero. This is because of measurement uncertainty introduced by either digitalization error or microscopic surface fluctuation. Although they may take up a considerable percentage of the field of view, such non-zero values do not reflect feature sharpness. They must be eliminated in order not to be mistakenly amplified by the following feature enhancement step. Threshold filtering provides a possible solution: any value between measurement uncertainty threshold ±ε should be set to zero in the resultant 3D difference map $\overline{\overline{h}\_diff}(x, y; d, d - l\delta d)$.

Step 4: Feature enhancement

After step 3, the remaining non-zero values in 3D difference maps stand for feature sharpness variation. However, from an image processing point of view, their distribution in gray level (the axial scanning range) needs to be further adjusted by a histogram regularization step. The purposes of this step are: 1) enhance weak features / small height differences and 2) reshape the histogram, to make it suitable for a selected sharpness calculation.

In this work, feature enhancement of a 3D difference map after step 3 is accomplished via a revised histogram equalization process: First, pick out all non-zero values; next, do histogram equalization for these values; then calculate the mean of the equalized values; finally, set all zero points in the original 3D difference map to be this mean value. The feature-enhanced 3D difference maps are noted as

$\overline{\overline{h}\_diff}_{eq}(x,y;d,d-l\delta d)$

The above described process is developed especially for variance calculation: on one hand, the majority zero valued points contain no feature information, thus should be designed to have no contribution to the variance; on the other hand, variance based indicator would be most efficient when the histogram is reshaped closer to a Gaussian distribution. If another sharpness calculation is to be adopted in step 5, the process of feature enhancement may be adjusted accordingly.

Step 5: Implement differential indicator $\eta\{d\}$

The differential indicator described below is based on variance calculation. The major difference is, instead of the maximum of variance, the symmetry around the focus is emphasized: at each position d, two 3D difference maps, namely, $\overline{\overline{h}\_diff}_{eq}(x,y;d,d-l\delta d)$ and $\overline{\overline{h}\_diff}_{eq}(x,y;d+l\delta d,d)$ are considered. If their variances, $Var\_diff_{eq}\{d,d-l\delta d\}$ and $Var\_diff_{eq}\{d+l\delta d,d\}$, are equal, d will be recognized as the location of the best focus plane. The regularized indicator to estimate how close a selected plane is to the best focus is thereby:

$$\eta\{d\}=\frac{Var\_diff_{eq}\{d+l\delta d,d\}-Var\_diff_{eq}\{d,d-l\delta d\}}{Var\_diff_{eq}\{d,d-l\delta d\}+Var\_diff_{eq}\{d+l\delta d,d\}} \tag{3.2}$$

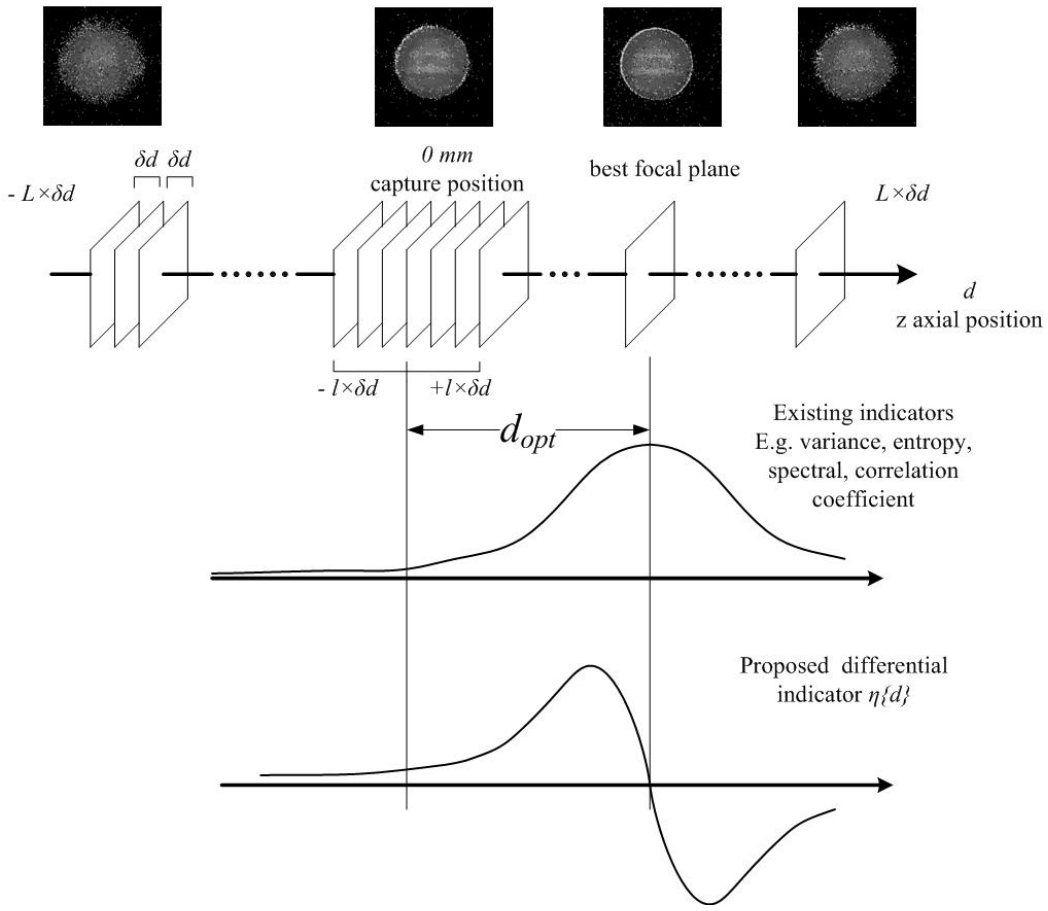

Fig 3.2 Sequential 3D maps and focus detection curves

Fig 3.2 illustrates the idea of $\eta\{d\}$. Symmetry detection implements a further subtraction upon 3D difference maps, which can be viewed as a kind of differential operation to a maximum finding curve. By combining information from three frames: $h(x,y;d-l\delta d)$, $h(x,y;d)$ and $h(x,y;d+l\delta d)$, each point on $\eta\{d\}$ curve contains more information than the existing indicators, and should therefore be more robust: a sharper indication of the best focus with less "false alarms" would be expected. As an extra benefit, $\eta\{d\}$ directly tells the relative location of the best focus by its sign. This would be especially helpful when either the best focus position or the capture position is unknown.

The proposed focus detection criterion is summarized in flow chart in Fig 3.3.

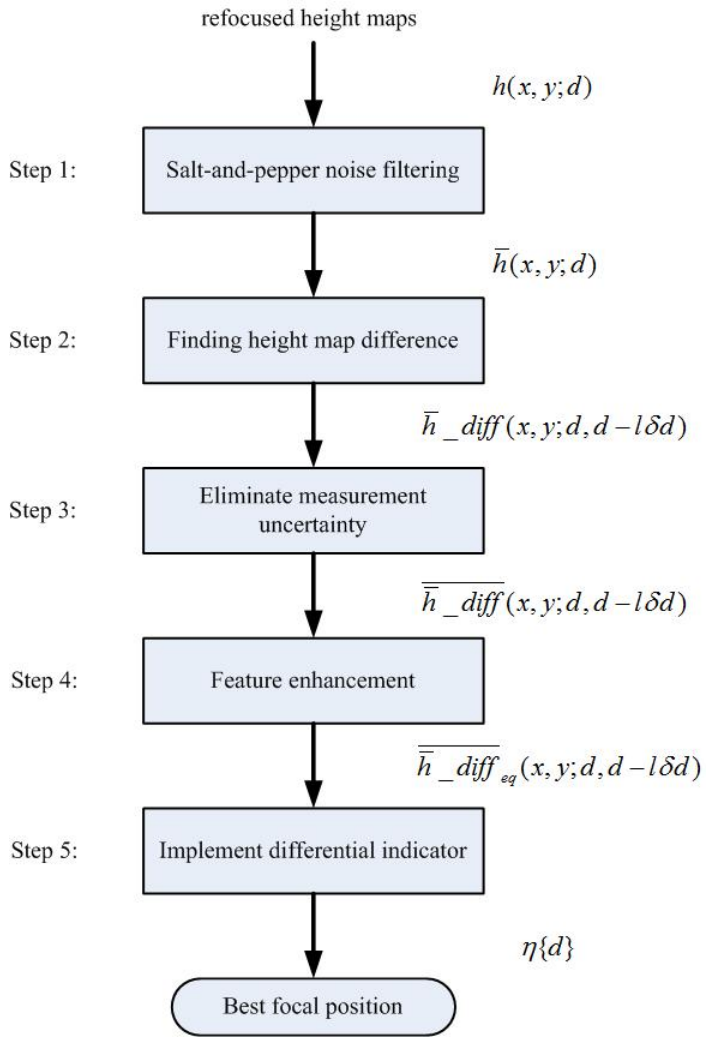

Fig 3.3 Flow chart of the differential focus detection criterion

3.4. Experimental results

3.4.1 Parameter selection

Based on experimental environment, the following parameters in the proposed criterion should be decided in advance:

- δd reconstruction sequence interval

Depend on the nominal depth-of-field of the imaging system. The depth-of-field for our system is approximately ±25mm. Thus δd is selected to be 25mm.

- ±Lδd sequence range

Depend on the maximum possible measurement range. Selected to be ±750mm in our experiment.

- Type of impulse filter in step 1

Depend on the density of salt-and-pepper noise. In our experiment, the simplest 3-by-3 median filtering is proved sufficient.

- lδd the difference interval between two frames in step 2

Depend on how sensitive the features are towards refocusing. Selected to be 6×25mm in our experiment.

- ±ε measurement uncertainty threshold in step 3

Should be related to measurement repeatability. Since the difference operation in step 2 amplifies uncertainty by a factor of $\sqrt{2}$, empirical value of 2ε is usually around 3 ~ 6 times of repeatability standard deviation. In our experiment shown in chapter 2, the repeatability of the majority points is around 2μm. Hence the measurement uncertainty threshold is selected to be ±5μm.

For comparison purpose, performances of a few other indicators are also

displayed:

Ent: entropy indicator [Gillespie, 1989]

$$Ent = -\sum_{x}\sum_{y}\{p(x,y)\times\log[p(x,y)]\} \tag{3.3}$$

Var: variance indicator [Ma, 2004]

$$Var = -\sum_{x}\sum_{y}[p(x,y)-p_{mean}]^2 \tag{3.4}$$

Spec: spectral indicator [Langehanenberg, 2008]

$$Spec = \sum_{u}\sum_{v}\log\{1+\left|\mathcal{F}_{u,v}^{+1}p(x,y)\right|\} \tag{3.5}$$

$\mathcal{F}_{x,y}^{+1}$: 2D Fourier transform (see Eq. 2.8)

CC: correlation coefficient indicator [Choo, 2006]

$$CC = \frac{\sum_{x}\sum_{y}[p_1(x,y)-p_{1mean}][p_2(x,y)-p_{2mean}]}{\sqrt{\{\sum_{x}\sum_{y}[p_1(x,y)-p_{1mean}]^2\}\{\sum_{x}\sum_{y}[p_2(x,y)-p_{2mean}]^2\}}} \tag{3.6}$$

$p(x,y)$ stands for the 3D map to be processed, and p_{mean} represents its mean value. For variance, spectral and correlation coefficient indicators, $p(x,y)$ are median filtered 3D maps, i.e., $\bar{h}(x,y;d)$; For entropy, since available feature differences are too weak, $\bar{h}(x,y;d)$ is pre-processed by a direct histogram equalization operation.

In correlation coefficient indicator, the special interval between $p_1(x,y)$ and $p_2(x,y)$ is selected to be 6×25mm, in accordance with lδd for the developed

indicator.

3.4.2 Results

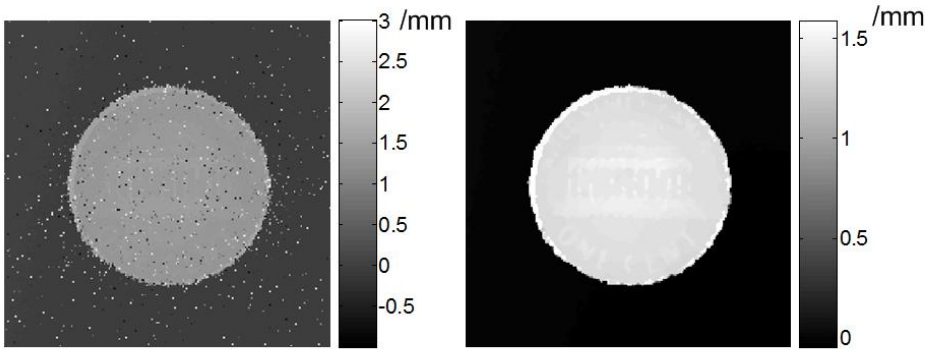

a) original height map $h(x,y;d)$

b) median filtered height map $\bar{h}(x,y;d)$

Fig 3.4 3D height map before and after median filtering

Experimental result of the 200mm out-of-focused penny in Fig 3.1 is shown. Its axial distance scanning range is from -1mm to 3mm, with a 1μm step size. Features over the penny (typically around 100μm in height) are almost invisible in the original 3D map $h(x,y;d)$ in Fig 3.4 a); on the contrary, salt-and-pepper noises are much more evident. After median filtering, noises are removed in Fig 3.4b). Difference 3D map $\bar{h}\_diff(x,y;0mm,-150mm)$ is shown in Fig 3.5a), and its corresponding histogram is demonstrated in Fig 3.5b). It can be observed that over 91% of the points are within ±5μm. In spite of their large percentage, these points are irrelevant towards feature sharpness. Histogram equalization is directly implemented on $\bar{h}\_diff(x,y;0mm,-150mm)$, and the resultant gray image and corresponding histogram are shown in Fig 3.5c) and Fig 3.5d). The tiny difference within measurement uncertainty is amplified because of their percentage superiority, while the true feature sharpness information is still crowded in two narrow bands. Fig 3.5e)

and Fig 3.5f) display feature enhanced image $\overline{\overline{h}\_diff}_{eq}(x,y;0mm,-150mm)$ and its corresponding histogram resulting from step 3 and step 4. It is clear that histogram information other than zeros is widely spread in the whole range, indicating a more effective feature sharpness enhancement operation.

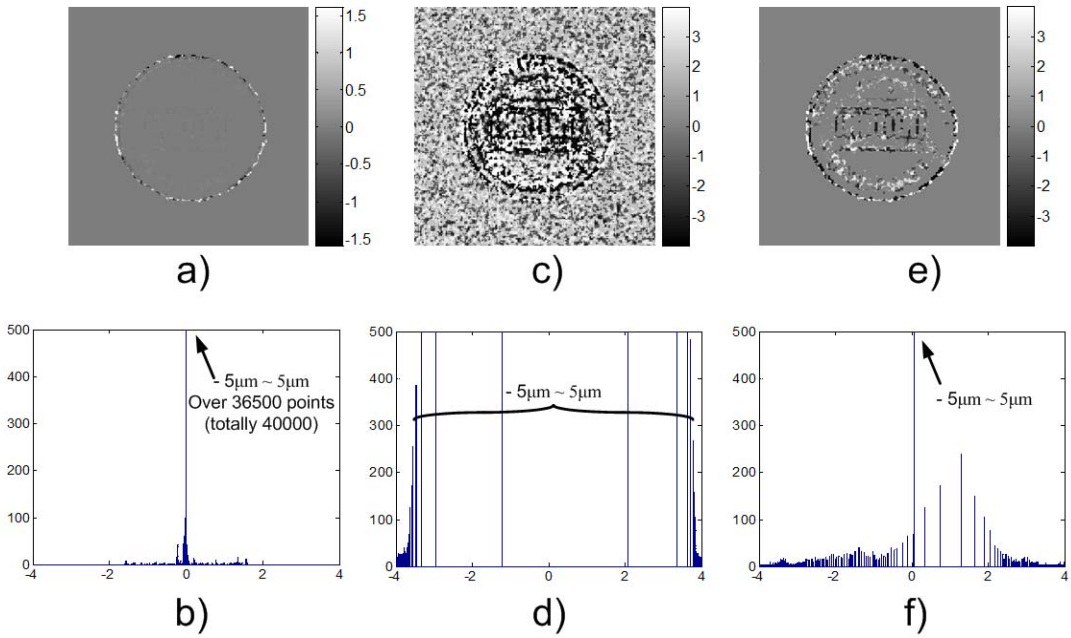

Fig 3.5 Feature enhancement: a) $\overline{h}\_diff(x,y;0mm,-150mm)$; b) histogram of a); c) histogram equalization without uncertainty elimination; d) histogram of c); e) $\overline{\overline{h}\_diff}_{eq}(x,y;0mm,-150mm)$ feature enhancement after uncertainty elimination; f) histogram of e).

The differential curve $\eta\{d\}$ is shown in Fig 3.6. Its zero-passing is at 210.3 mm. Comparing with system's depth-of-field, ±25mm, this result is of satisfactory accuracy.

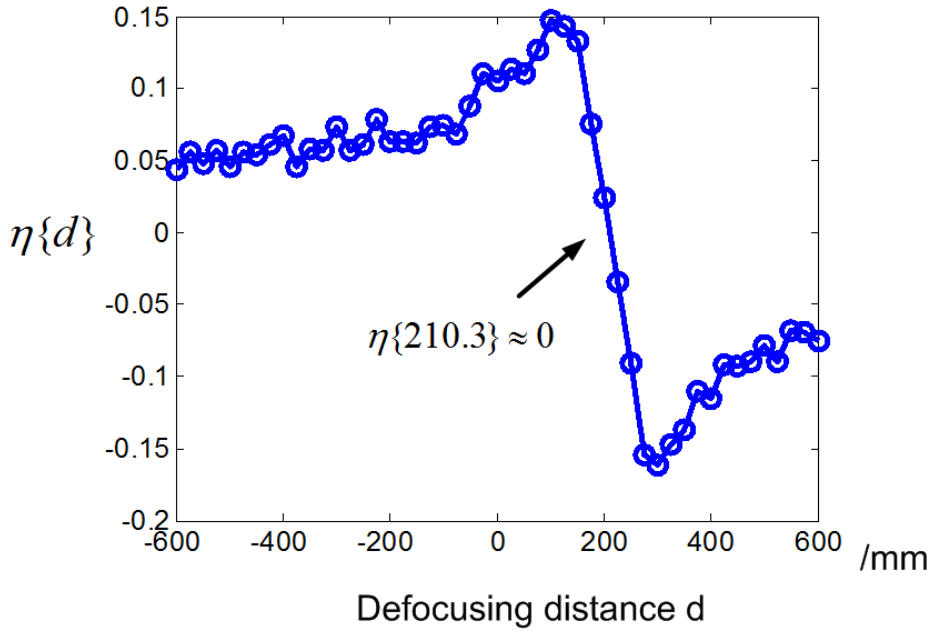

Fig 3.6 Focus detection curve $\eta\{d\}$ for the out-of-focus penny in Fig 3.1

Fig 3.7 a) to d) demonstrate results by entropy (Ent) indicator, variance (Var) indicator, spectral (Spec) indicator and correlation coefficient (CC) indicator. In Fig 3.7 a), entropy curve does not tell the correct best focus position; Although with limited accuracy, variance curve and spectral curve do show some kind of local maxima in Fig 3.7b) and c). Nevertheless, local maxima are insufficient for automatic focus detection purpose. The CC indicator successfully overcomes the problem of local maxima and finds the correct best focus position. However, it displays a wide top range from approximately 125mm to 300mm in Fig 3.7d). Such flat top phenomenon indicates that the result is likely to be corrupted by residual noise, or filtered out by commonly adopted curve fitting method in follow-up signal processing steps. Thus the method is in general less reliable.

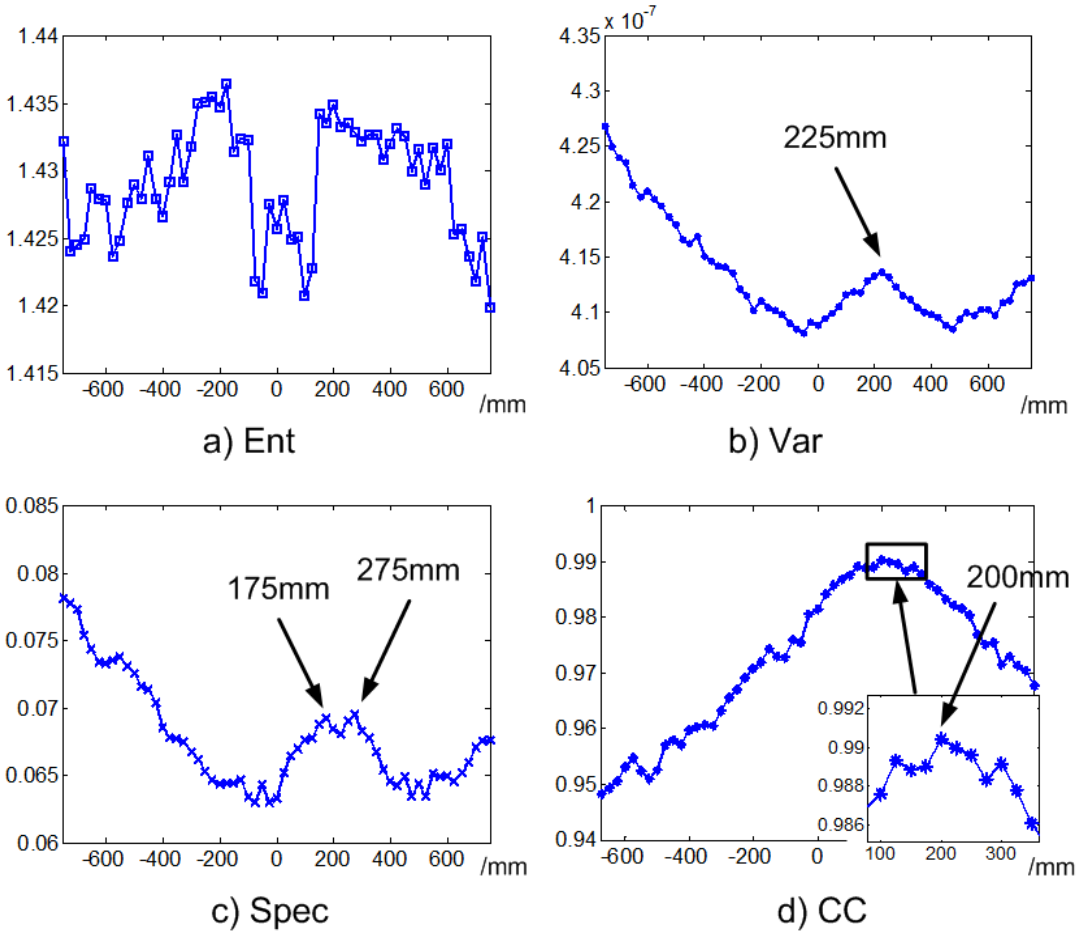

Fig 3.7 Result of other indicators: a) entropy indicator; b) variance indicator; c) spectral indicator; d) correlation coefficient indicator

Two more examples are provided in Fig 3.8 and Fig 3.9, both of which are measured with system's depth-of-field of ±25mm. Fig 3.8 demonstrates a result of "concave" features by measuring a key 200mm out of focus. Different from the penny example, main features over the key (the characters) are below their background. Surface quality of the key is also worse, as more salt-and-pepper noise points can be observed. The detected best focus position is 210.1mm from its capturing origin.

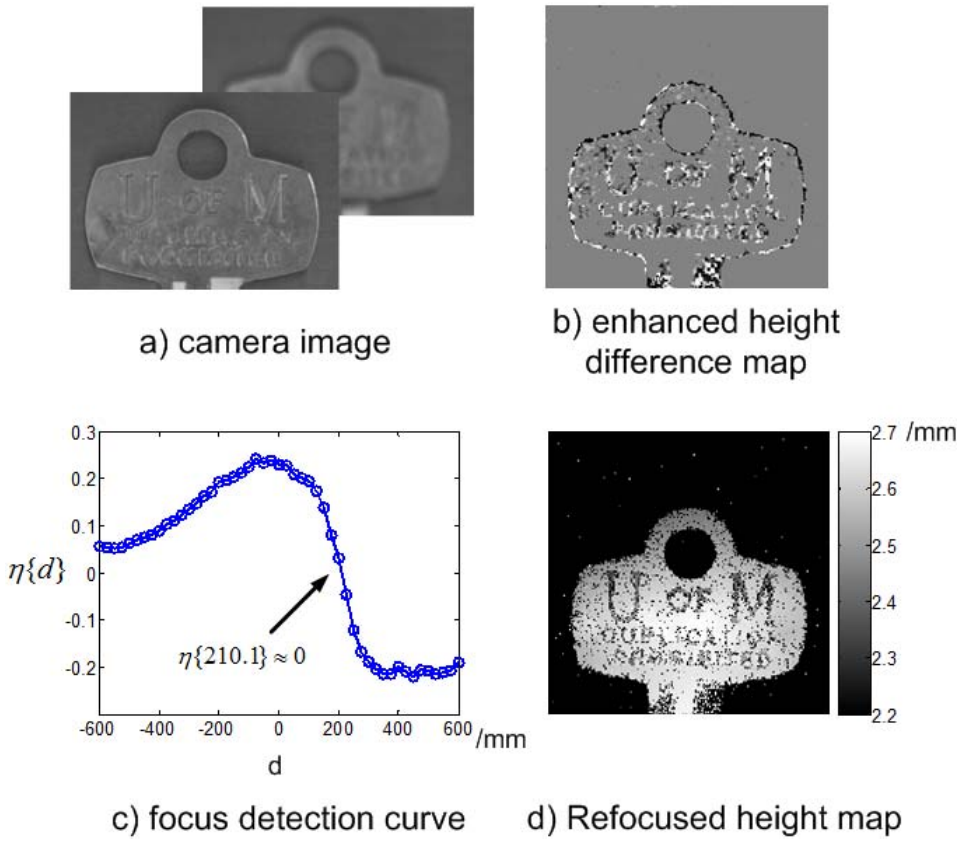

Fig 3.8 Result of imaging a key 200mm out of focus

Fig 3.9 shows a possible solution of "weak feature" recognition. An artificial part with characters "coherix" has been captured 300mm out of focus. The characters are approximately 1mm above their background. The detected refocusing distance is 311.5mm. Over the machined background, there are tooling marks typically of 10μm to 30μm in height. These tooling marks are barely above the uncertainty filtering threshold and containing very limited refocusing information. The exact patterns of tooling marks are of observation interest in machining process analysis. Due to measurement time or structure limitations, some of the machined surfaces have to be observed out-of-focus. Details of tooling marks can therefore be covered by blurring. Since they contribute little in focus detection, a direct focus detection based on tooling

marks can be severely deviated. The refocusing result shown in Fig 3.9d) demonstrates a solution that relates weak features (tooling marks) to strong features (characters) to achieve satisfactory observation quality for the former.

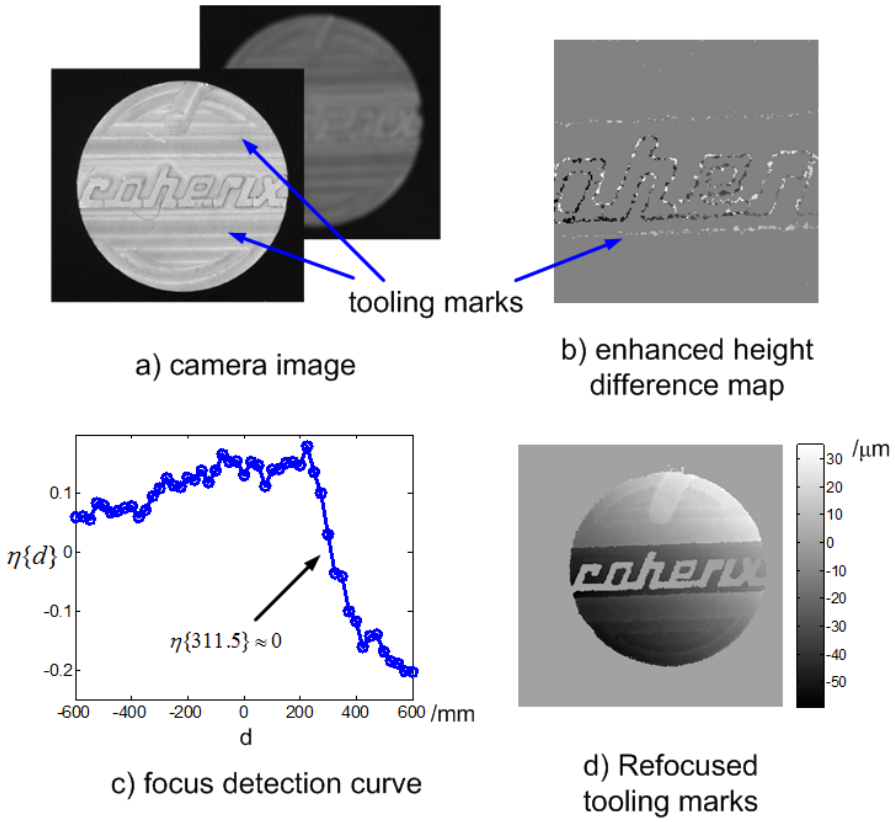

Fig 3.9 Result of "coherix" image. For clearance, in d) the refocused 3D map is displayed within -60µm to +35µm range after 3-by-3 median filtering

3.5 Conclusion and potential future work

This chapter demonstrated that, by implementing multi-wavelength holographic interferometry, holographic focus detection criterion can be based on phase contrast distribution. A specific criterion has been developed with experimental results on step-like 3D structures proving its feasibility. The developed technology can be especially helpful in practical applications, because it provides a possibility of

recognizing micron level tooling marks over surfaces far out of focus.

Nevertheless, further improvement of the criterion is necessary. For example, to preserve more details from "salt-and-pepper" noise, advanced data filtering algorithm shall be developed instead of traditional median filter. Another question of interest is how much the selected parameters in section 3.4 depend on a specific system and the certain object to be investigated. Future studies should also involve questions such as how the criterion can be improved for a "boundary" condition, with object features between gentle and step like. Integrating focus calibration process into the criterion to remove detection inaccuracy induced by depth-of-field variation, such as described in [Tachiki, 2008], would be of practical value. Furthermore, studies on how to further reduce phase error in a practical system would also be of remarkable value.

A final remark related to the combination between amplitude contrast and phase contrast is that, although theoretically there is no dependency between them, in many experimental cases they are more or less related, either proportional or inversely proportional. This is most likely due to the similarity of either materials or surface quality conditions. Such a relation can be viewed as valuable information, even though it may be corrupted severely by noise. With modern signal processing technology, such as Principal components analysis (PCA) [Jolliffe, 2002] or independent components analysis (ICA) [Hyvarinen, 2000; Hyvarinen, 2007], or wavelet based methods, this information would be proved useful in practice.

Chapter 4

3D Shape Reconstruction via Multi-wavelength Holographic Refocusing

4.1 Introduction

Based on the results developed in Chapters 2 and 3, this chapter aims to form a merged, in-focus 3D profile of high quality.

Some papers [Ferraro, 2005; Paturzo, 2009] in the microscopic field refer to merged image from differently focused sub-areas as extended focus image (EFI). Traditional EFI (as shown in Fig 4.1) is generated by scanning the depth-of-field, mechanically, selecting the in-focus area from each picture, and stitching them together [Hausler, 1972; Pieper, 1983]. With digital holography, mechanical scanning for focal plane is no longer essential, as multiple scans can be numerically generated of a single-position capture. This provides significant convenience to intensity based imaging analysis.

A drawback of current digital holographic EFI technology is that it has difficulty in automatically identifying multiple, unknown shaped targets and transferring them into their respective best focal position. A commonly adopted concept is to segregate

the image into different blocks or cells, then apply focus detection criteria demonstrated in Chapter 3 block by block, and do digital refocusing accordingly [Mc Elhinney, 2005; Tachiki, 2008]. However, this brings another problem, as demonstrated in [Tachiki, 2008], that blocks with insufficient features (either having no object or being occupied by a whole object yet with no significant change during digital refocusing) are generally hard to find their exact focal plane via focus detection algorithms. A brief literature review on methods of identifying and separating objects and generating EFI holographic images is provided in section 4.2.

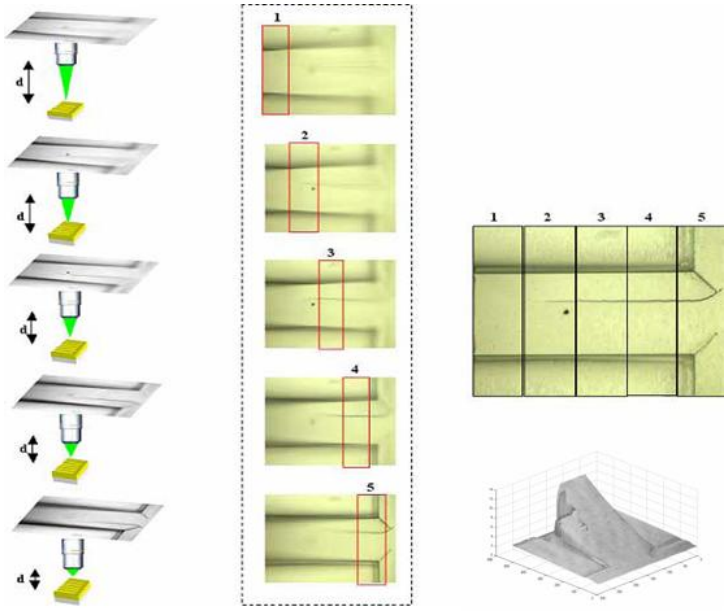

Fig 4.1 Qualitative drawing of the working principle of the EFI method (reprinted from [Ferraro, 2005] Fig 1 and Fig 7)
Stack of in-focus images (sequentially numbered) corresponding to different portions of the imaged object are stuck together to get an overall in-focus image (on the right)

With MWHI, similar benefit is expected as in EFI. What is unique here originates from MWHI's extended absolute distance measurement range. Axial locations of the target objects can be obtained in a distance measurement way: If one

of the objects (an object used as a datum) can be located in the axial direction, all other objects within the absolute measurement range around it can be located accordingly. So long as the relative distances can be measured via interferometry correctly, the locations of objects are irrelevant to whether they have significant surface features or not. Weak feature objects of metrology interest can be located with sufficient accuracy in this way.

An example of the necessity of this technology is monitoring tooling marks over out-of-focus surfaces. As mentioned in chapter 3, tooling marks usually have micron level fluctuation over machined metal surfaces. They are very difficult to be clearly observed if the surface itself is placed out of focus in practice. In the meantime, they can be too weak to be used as significant targets for focus detection. In such cases, putting a significant target (such as a penny) within its absolute height range is suggested to help locating the best focal plane.

4.2 Literature review

Many articles have been addressed to generate EFI in digital holographic images. Although their methods are based on a variety of different physical characteristics of the imaging process, learning from these methods provides a beneficial broad view for our research objective.

In [Almoro, 2007], the objects were recognized based on their colors. Under the illumination of different wavelengths (colors), the object having the corresponding

color would be evident, while other objects with different colors would be dim. The sensitivity of this method towards wavelength change is low. Thus it is less likely to be applied in MWHI.

In [Kim, 2006; Zhang, 2008; Zhang, 2009], a novel separation method based on height difference was provided, by using optical scanning holography. However, its optical heterodyne physics makes it capable of only recovering amplitude: Its distribution at a certain depth to be separated should have no contribution to the imaginary part of the respective holographic expression. That is why it can be segmented via mathematically separating the real and imaginary parts of the expression. The idea is not viable in multi-wavelength holography, where phase information / imaginary parts are critical for height measurement and must be preserved in the segmentation.

In the field of image processing, people have tested algorithms to fuse the series of reconstructed holograms, rather than separate the in-focus areas from the out-of-focus areas, to form an EFI image. [Cuong, 2005; Javidi, 2006; Cuong, 2007] demonstrated algorithms employing ICA (independent component analysis) and DWT (discrete wavelet transform), respectively. They achieved visual success. Nevertheless, by changing parameters their results can show the impact of blurring, since fusion is basically putting weights to each hologram. In addition, blurring can be interpreted as inaccurate or erroneous measurement in synthetic height map, which is exactly what refocusing want to prevent. Thereby, the way of image fusion may not be a good

choice for metrology purpose.

In [Paturzo, 2009], a parameterized model was employed to the distribution of targets (for example, they stayed in a plate tilting from the perpendicular imaging plane), and a corresponding algorithm was developed to cure the out-of-focus blurring effect. The method had demonstrated interesting possibility of fulfilling EFI on a tilted USAF target board. However, in more general cases, the distribution of targets is hard to predict.

The idea of generating digital holographic EFI by separating the image into small blocks was described in [Mc Elhinney, 2005] and [Tachiki, 2008]. Focal measurement algorithms were applied to each of the individual blocks, the best focal positions were calculated, and then blocks from their best focal positions could be used to stitch an EFI. The major drawback of this idea, as reported in [Tachiki, 2008], is that it has difficulties in getting correct best focal distances for featureless blocks (which is referred to as “voids”, consist of “flats”, featureless object surface occupies the entire block, and “blanks”, blocks with no objects).

The usage of interferometric information to form an EFI had been proposed by [Ferraro, 2005] and [Colomb, 2010], in which a single wavelength holographic microscopy was employed. The best focal positions of different blocks were determined by phase maps on a gentle and continuous slope of the target to be imaged. Since the absolute height range of a single wavelength is limited, this method will have difficulties while imaging multiple discontinuous targets or target with a sharp

slope.

4.3 3D profiling of multiple target objects at different axial locations

The study proposed in this chapter further develops the idea in [Mc Elhinney, 2005; Tachiki, 2008] and [Ferraro, 2005]. Focus detection criteria depend heavily on surface features, such as edges, which can show difference between in-focus and out-of-focus captures. Distance measurement via MWHI outperforms focus detection as it is feature independent. MWHI distance measurement alone cannot tell where the best focal position is, since it cannot discriminate between the status of "in-focus" and "out-of-focus" based on blurring effect. In other words, it is an effective tool of measuring "relative location", but not qualified in determining "absolute location". Thereby, there stands a chance to combine focus detection criteria and MWHI measurement to fulfill accurate 3D shape profiling as follows: First determine an in-focus "datum" by applying focus detection criterion to one of the objects or blocks with evident features, then relate the rest objects or blocks to this datum and calculate their individual best focused profiles.

This key idea can be further illustrated as follows: Assuming multiple objects distributed in a wide image depth range are to be observed simultaneously, as shown in Fig 4.2a). Some of them (object A, for example) carries features of sharp edges (referred to as "strong feature"); others (objects B and C) do not have feature sharp enough for a focus detection purpose ("weak feature"). To have all of the objects clearly displayed within one frame, the following steps are to be carried:

1. Find the out-of-focus distance of object A (Fig 4.2b));

2. Relate the location of other objects with respect to object A (Fig 4.2c));

3. Calculate the respective refocusing distances of each object (Fig 4.2d));

4. Perform digital refocusing to achieve accurate 3D profiling of the objects (Fig 4.2e)).

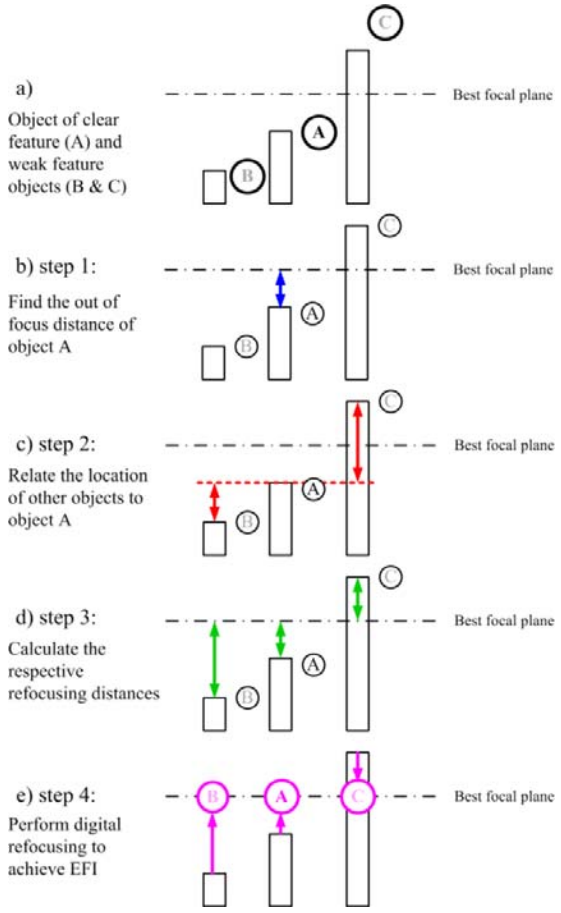

Fig 4.2 Working principle of generating accurate 3D profiles via MWHI refocusing approach

Step 1 is a typical phase contrast based focus detection operation, which intends to set up a datum for all the objects to be refocused. The accuracy of this step is

related to how strong the feature over the selected object is. In practical cases, the target with strong feature can either be an existing part of the object or a designed one located deliberately. In Step 2, MWHI is used to estimate refocusing distance. Although details over an object placed out of focus may not be recognizable, a generally correct axial location of the object can still be obtained: So long as the axial scale of blurred details does not exceed the depth-of-field, the distance estimation should be considered valid. Step 3 combines the results of Step 1 and Step 2, which leads to absolute distances of each object to their individual best focus plane. Step 4 refocuses the objects accordingly and reconstructs the expected 3D profile.

It is worth noticing that, although MWHI is applied repeatedly in Steps 1, 2 and 4, the objectives are different: in Steps 1 and 4, MWHI is used as an image construction tool; while in Step 2, it is employed to estimate refocusing distance. Such difference would result in different parameter choice while doing height scanning (Eq. 2.6): for image construction purpose, Eq. 2.6 should be applied to each individual pixel, and the minimum scan step should be set small enough to avoid round-off error. For refocusing distance estimation purpose, since the total scanning range can be much larger than that for imaging, while accuracy requirement is relatively lower, to reduce processing time, it is reasonable either to set scanning step larger, or to carry out the operation only on selected pixels.

4.4 Experimental results

An artificial part demonstrated in Fig 4.3 has been imaged by a “Shapix” system

(Coherix Inc.), whose experimental parameters are listed in Table 4.1. The part has eight plateaus, numbered from A to H. Surfaces of the plateaus are machined and polished, leaving superficial tooling marks as weak features to be observed. Three pennies are placed over Plateaus B, D and G, representing objects with strong features. The interval between every two adjacent plateaus is approximately 25mm, in accordance with the depth-of-field of the imaging system. In the experiment, the part is loaded so that Plateau D is placed 150mm out of focus.

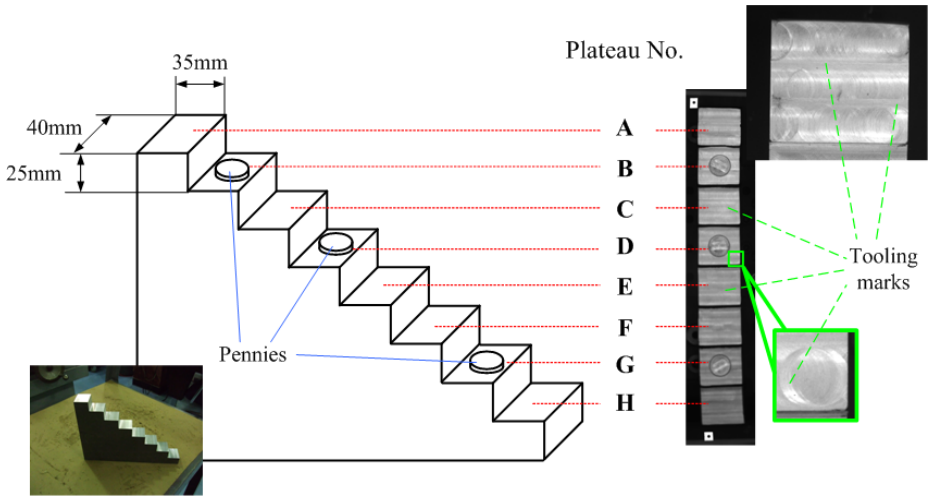

Fig 4.3 Artificial part with tooling marks to be imaged

Wavelength λ_p	14 selected wavelengths, ranging from 838nm to 853nm		
Number of pixels	2048 ×2048	Pixel interval Δ	7.5 μm
Magnification M	1/20	Depth-of-view in the object field	Approx. ±25mm around best focus

Table 4.1 Parameters of the Experimental MWHI system

In Step 1, Plateau D is selected as the datum. Data processing parameters are selected as follows: For MWHI imaging, the height scanning range is -1mm to +3mm,

with a minimum step of 1μm. For focus detection, a series of frames are reconstructed along focal depth, with an interval δd of 25mm. 3-by-3 median filtering is implemented to eliminate noise; interval $l \times \delta d$ in Eq. 3.1 is 150mm; Uncertainty threshold ε is 6μm. The focus detection curve of Plateau D is shown in Fig 4.4, indicating that the estimated out-of-focus distance is approximately 156.6mm.

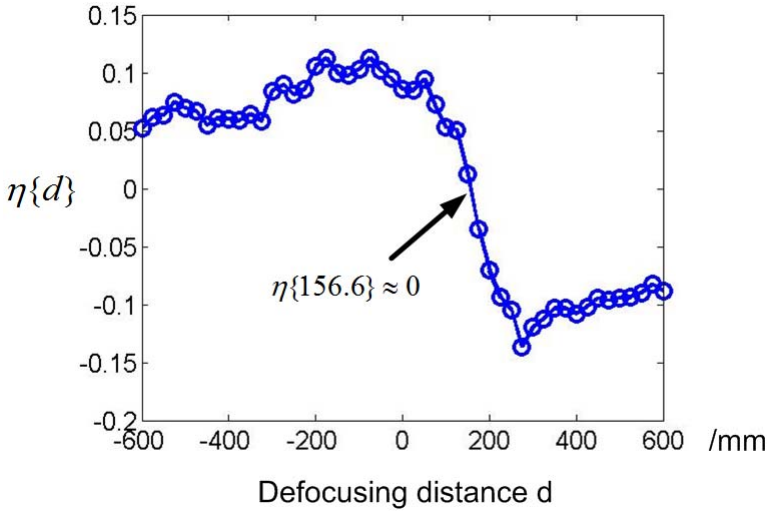

Fig 4.4 Focus detection curve ($\eta\{d\}$) for Plateau D

In Step 2, MWHI is implemented for distance estimation. The height scanning range is set to be -150mm to 150mm, with a minimum step of 10μm. Relative distances of each plateau towards Plateau D are listed in Table 4.2.

Plateau No.	A	B	C	D	E	F	G	H
/mm	74.8	49.9	25.0	0.0	-24.9	-49.9	-74.8	-100.2

Table 4.2 Distance of each plateau towards Plateau D by MWHI

Fig 4.5 displays distance measurement results of Plateau A by setting different step intervals. Fig 4.5a) has a minimum step of 1μm, while the step of Fig 4.5b) is

10μm. Both figures are 3-by-3 median filtered. In Fig 4.5a), the two major tooling marks are clearly observable; while in Fig 4.5b), although the tooling marks are smeared by round-off error, the general location of Plateau A is well preserved to 0.1mm. The largest step interval is limited by Nyquist Law, which requires that there should be at least two sampling points within $\lambda_{syn} = \frac{\lambda_1 \lambda_2}{\lambda_1 - \lambda_2}$. In the experiment, the shortest λ_{syn} is longer than 36.1μm (0.84μm × 0.86μm / 0.02μm). Thereby the selected 10μm interval is valid.

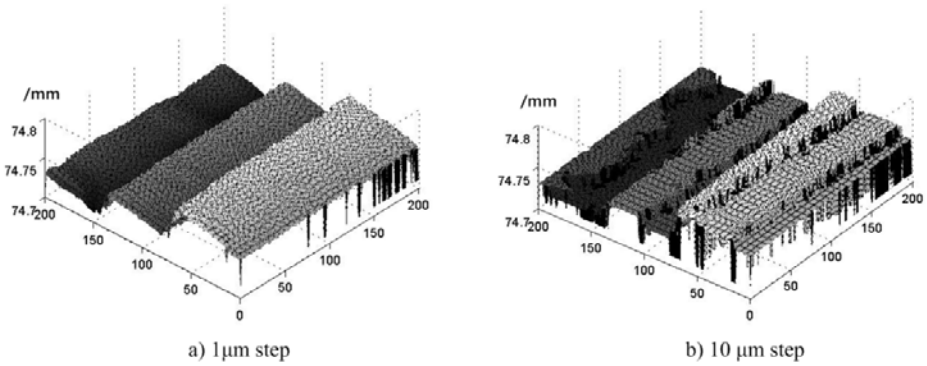

a) 1μm step b) 10 μm step

Fig 4.5 MWHI reconstructed Plateau A with minimum step interval of: a) 1μm (for imaging purpose) and b) 10μm (for distance measurement purpose)

Calculated refocusing distances by Step 3 are listed in Table 4.3. Also listed are refocusing distances reported by Plateau-by-Plateau focus detection, as well as the nominal out of focus distances of the plateaus.

Fig 4.6a) shows the reconstructed EFI by the proposed MWHI approach. Since distance measurement in Step 2 is independent of features, axial distance relation among plateaus is well preserved. For comparison, the result of Plateau-by-Plateau focus detection and refocusing approach is shown in Fig 7b), which shows that

Plateaus C and D are estimated to be of very similar height. Since focus detection is highly dependent on the strength of features observed, the relative axial location is not correctly reflected.

Plateau No.	A	B	C	D	E	F	G	H
MWHI	-81.8	-106.7	-131.6	-156.6	-181.5	-206.5	-231.4	-256.8
Focus detection	-55.5	-88.0	-153.5	-156.6	-197.4	-233.0	-272.5	-313.0
Nominal	-75	-100	-125	-150	-175	-200	-225	-250

Table 4.3 Refocusing distances of plateaus (/mm)

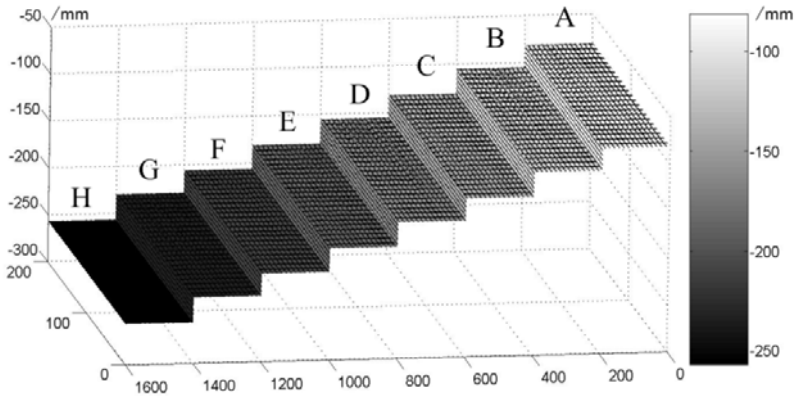

a) MWI approach

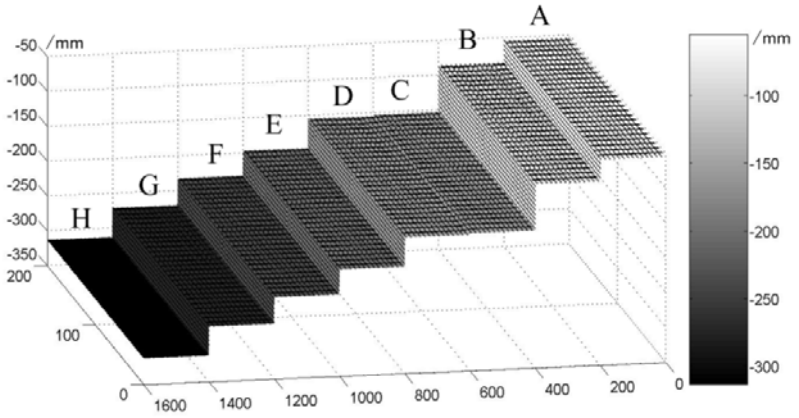

b) Plateau-by-plateau focus detection approach

Fig 4.6 EFI reconstructed via: a) MWHI approach;

b) Plateau-by-Plateau focus detection and refocusing approach

Fig 4.7 displays views of pennies on Plateaus B, D and G by both approaches. Comparing with the original captured views, both approaches display clarity enhancement for strong features. It can be inferred that the reason why Plateau-by-Plateau focus detection can give deviated distance measure is also partially due to the nonlinearity of the imaging system, especially the variation of focus depth along axial direction as suggested in [Tachiki, 2008]. A properly designed calibration step would be expected to further improve the proposed process.

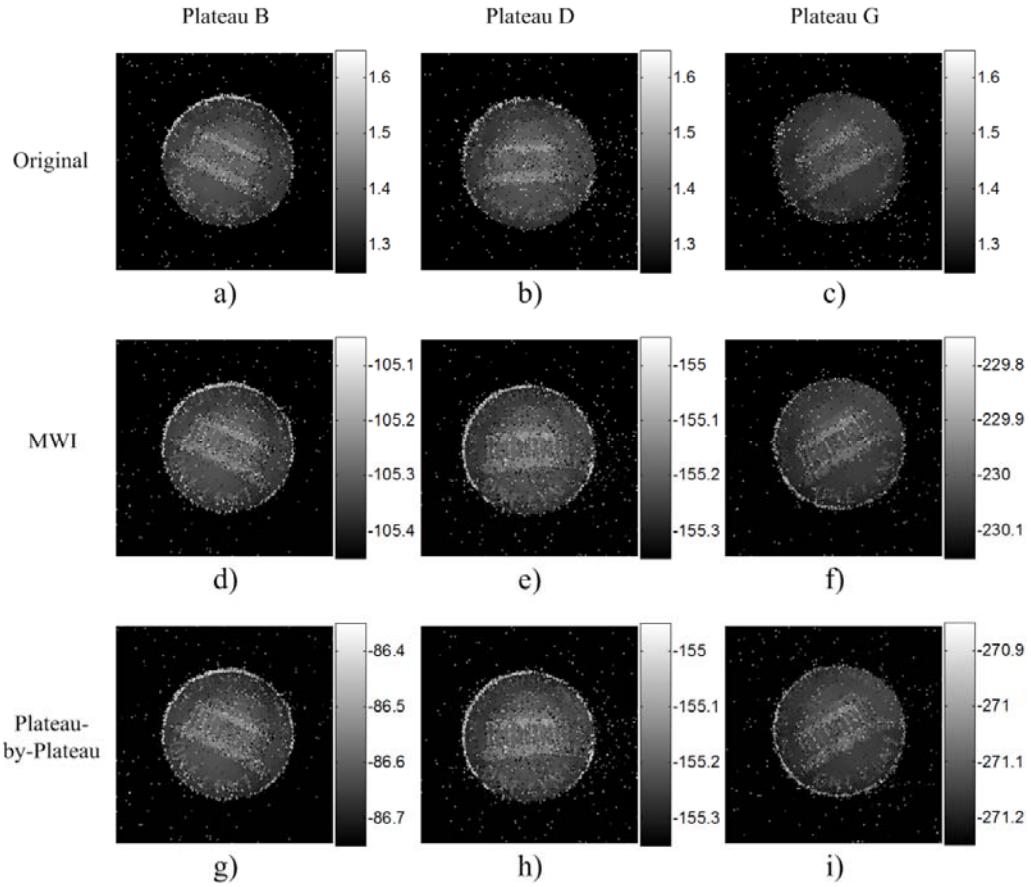

Fig 4.7 Views of pennies on Plateau B, D and G: a)~c) original captured views; d) ~ f) EFI by MWHI approach; g) ~ i) EFI by Plateau-by-Plateau approach (Scale bar: /mm)

To demonstrate weak features of the generated EFI by the MWHI approach, Fig

4.8 illustrates the circular tooling mark on Plateau D displayed in Fig 4.3. The tooling mark has a depth of less than 30μm. Fig 4.8a) displays the amplitude map and phase map of one of the holograms refocused 156.6mm to the best focus position. It can be concluded that this tooling mark is neither 'pure amplitude' nor 'pure phase' in its holograms, since at the best focus plane its profile can be read out from both amplitude map and 3D map. Therefore, the amplitude indicator proposed in [Dubois, 2006] will not be valid in this case. As shown in Fig 4.8b), neither the minimum nor the maximum of the amplitude sum indicator correctly reflects the true out of focus distance. The original captured height map and the 156.6mm refocused height map are shown in Fig 4.8c), indicating clarity enhancement of the tooling mark.

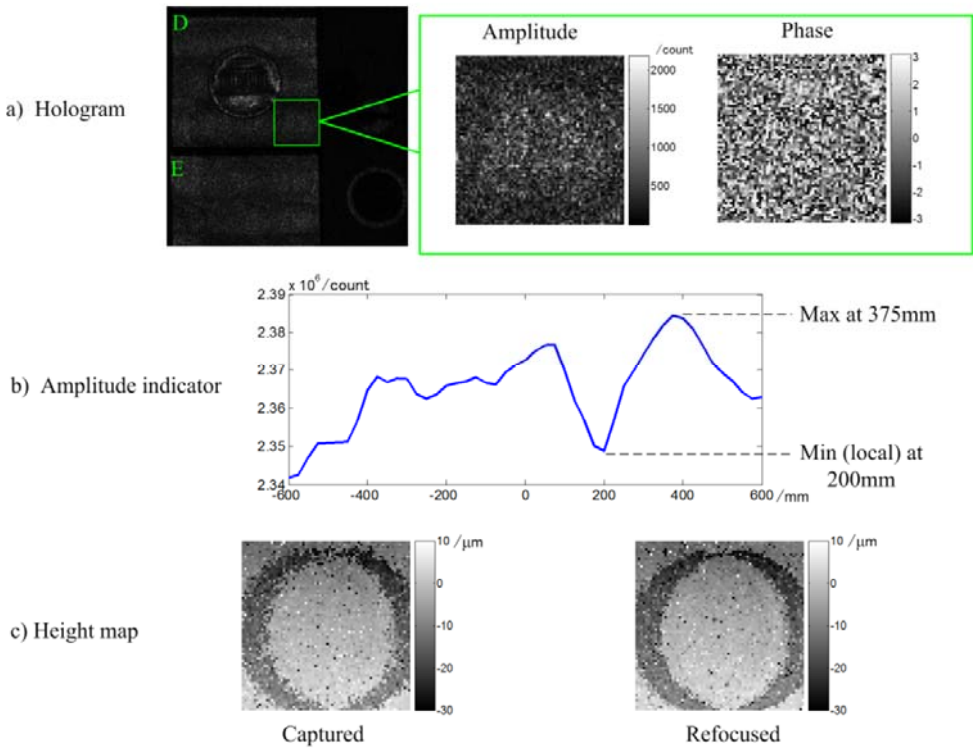

Fig 4.8 Tooling mark observation: a) amplitude and phase of one of the refocused holograms; b) amplitude indicator proposed in [Dubois, 2006]; c) captured view of the height map (left) and the refocused height map (right)

4.5 Conclusion and future work

Digital refocusing is performed with MWHI holographic imaging as a solution of 3D shape reconstruction. The key advantage is that, interferometric distance measurement of over ±100mm introduced by MWHI is implemented as a high accuracy focus detection tool for digital refocusing, which is not available in traditional EFI solutions. The proposed method not only expands axial clarity measurement range, but protects accuracy for axial measurements as well. Reconstruction example of an artificial test part provides a first-step prove of the feasibility of MWHI digital refocusing as a high quality 3D shape reconstruction tool. Future work to further improve the approach to increase measurement capability with more complicated objects involves efforts to make system more robust towards wavelengths fluctuation and stray light, as well as to work out a practical calibration process of matching realistic distance to the best refocusing distance due to system non-linearity.

Chapter 5

Stray Light Suppression by Pupil Apodization in MWHI

5.1 Introduction

In previous chapters, we have demonstrated that digital refocusing technology is helpful in multi-wavelength holographic interferometry (MWHI). It makes simultaneous high clarity measurement possible for multiple Z-directional isolated targets.

A further practical challenge in 3D profile measurement via MWHI derives from the difference in finishing properties of two laterally adjacent surfaces. In practice, the measurement of a dull rough surface often appears to be affected by its shiny smooth neighbor. As shown in Fig 5.1, gauge blocks of mirror-like surface quality are placed in the vicinity of a ground surface (Ra in the range of 8~16μm). From the MWHI measurement result, it can be observed that a large area of the ground surface is "measured" to be of the same height of its mirror-like neighbors. We infer from this result that there is stray light from the shiny surfaces to their neighboring area, which carries phase information leading to smeared measurement.

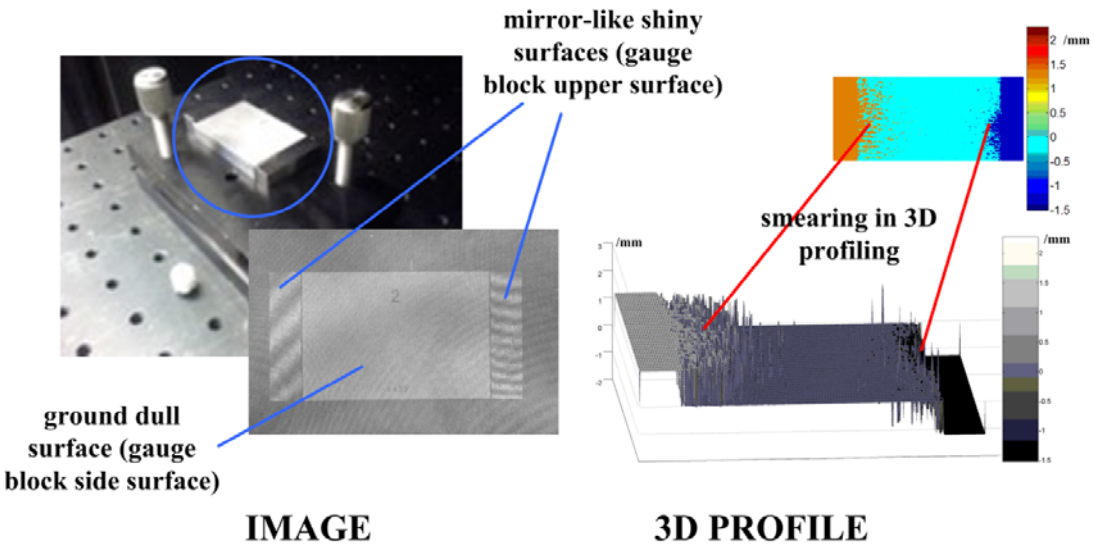

Fig 5.1 Observed measurement smearing from mirror-like (shiny smooth) surfaces to ground (dull rough) surface

A persuasive explanation of the phenomena indicates that the truncation of the system pupil edge leads to the observed smearing effect. The explanation starts from a model of surface facets (see section 5.2.1 for a brief literature review of models of rough surface scattering). As shown in 5.2, rough surfaces can be modeled as a series of small planar "facets". The facets are assumed to be absolutely flat, and they are tangential to the actual surface slope. Surface reflection patterns are determined by the orientation and reflectivity of these facets. In this chapter, we assume uniform reflectivity of each facet over machined surfaces, since they are, after all, of the same material. The orientation of a facet is represented by orientation angle α, which is the angle from the global normal of the surface profile to the local normal of the facet.

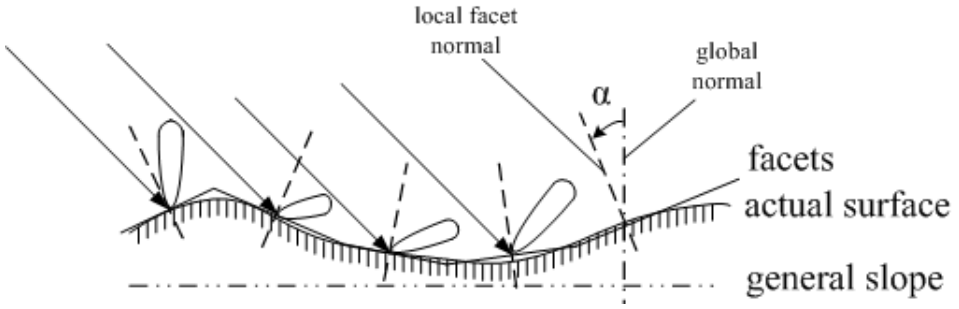

Fig 5.2 Facet approximation of a rough surface

Fig 5.3 shows two adjacent facets. They are differently orientated. Under collimated illumination, their focal points at the pupil plane are determined by their orientation angle. According to Fourier optics [Goodman, 1996], field distribution at the pupil plane can be viewed as a Fourier transform of the facet at the object plane. In the same way, the captured image of this facet at the image plane can also be understood as a Fourier transform of the field at the pupil plane. The role of the pupil can be viewed as a truncation function, which chops the Fourier transforms of the facets and leads to stray light in their images. It is then clear that, how severe the stray light of a facet is, largely depends on the orientation of that specific facet. If it makes the Fourier transform field centered close to the edge of the pupil, the resultant evident truncation effect will give severe side-lobes / stray light towards neighboring facets in the image plane. Otherwise, if the field is far away from the edge, the truncation effect will be faint, and side-lobes / stray light of the image will not be problematic towards the neighbors.

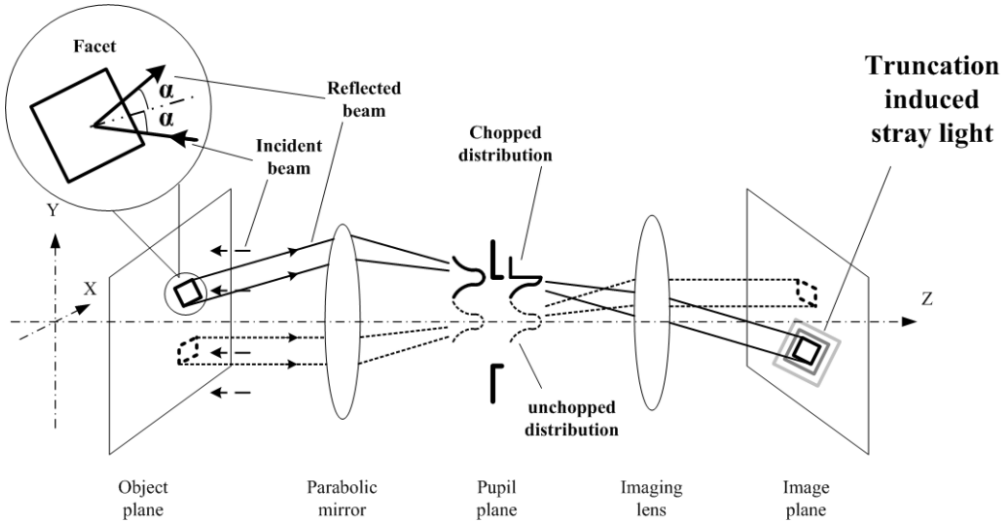

Fig 5.3 Origin of stray light

From a statistic point of view, orientation angle α can be viewed as random variable, whose distribution characterizes the properties of the surface under observation. For illustration convenience in a 2D model of facets, from here on we denote α according to the two axes, namely, into α_x and α_y, and assign joint or respective random distribution functions to them. A practical advantage of doing such a directional separation is that, as pointed out by some earlier literatures [Kierkegaard, 1996], machined surfaces can have very different distribution functions in directions perpendicular and parallel towards tooling traces. For most theoretical and computational studies within the scope of this chapter, we assume identical, Gaussian random distributions of the two directions, in order to protect the generality of the study, as well as to keep our derivation concise. Nevertheless, it is still worth noticing that, for future detailed and specific studies, separated consideration of surface properties is beneficial while doing a mathematical modeling work for rough surface scattering problems.

In this chapter, we propose a pupil apodization solution to alleviate the stray light problem. Instead of using a hard-edged aperture, a pupil with gradually attenuating transmission function is implemented to avoid the wave truncation effect. As far as we know, this is the first time that pupil apodization has been implemented in a MWHI imaging system.

The idea of apodization has been proposed for decades. However, manufacturing difficulty and cost prohibit the wide application of apodization for a long period. In recent years, due to the advancement of manufacturing, apodized filters with customized transmissivity curve have been commercially available. Quite a few articles have been published, reporting various applications, among which a major branch is astronomical observation, such as to discriminate dim extrasolar planet (exoplanet) from its relatively strong star background [Nisenson, 2001] (See section 5.2.2 for literature review of recent achievements and commonly applied metrics of pupil apodization in optics).

Comparing with works in the field of astronomy, a first difference in MWHI imaging is that the observation objects of interest are much more and much denser. In astronomical observation, the two objects, the exoplanet and the star, are isolated in dark background. The goal is usually to get them separated, while not much attention is given to the more detailed characteristics of the objectives. In other words, it is more a “detection” task rather than an “identification” task. Many one dimensional, asymmetric or shaped pupils are thereby applicable, which introduce quite a lot

peculiar point spread functions (PSF) [Kasdin, 2003], just for their sharp contrast in a certain direction or within a certain region. In MWHI imaging, objects are facets. They are so densely distributed that tens or hundreds of them can be crowded within a single pixel. Instead of getting them recognized one after another, it is more important to get the information carried by each facet restricted within their own realms, rather than to have them crosstalk with any neighbor in any direction. Therefore, an edge-free, azimuthally symmetric pupil is highly desired, aiming to generate a diffraction-limited PSF.

Another key difference in MWHI surface inspection is that the signal of interest is no longer amplitude or irradiance, as it is in many other applications. For MWHI imaging system, it is now phase of the captured holograms that carries useful information (object height). For this reason, metrics created to optimize apodization transmissivity curve need to be modified accordingly. In astronomical observation case, for example, two most frequently implemented metrics are contrast and integration time. As shown later in this chapter, the concept of contrast is still applicable in our study, yet with much lower requirement; integration time, on the other hand, will be replaced in our metrics, because the reflection from metal surfaces is strong enough to make a single capture completed within a second (while in astronomical observation, captures could take hours). Furthermore, a few other metrics should be included, for the consideration of accuracy and reliability of the phase signals.

In this chapter, we will first state the mathematical modeling of the problem. Then we will discuss and create necessary optimization metrics for selecting apodized transmissivity curves. Based on them, several known curves are compared via numerical simulation. The most promising curve is then selected and implemented in a real Shapix system. An experimental result is shown, demonstrating the effectiveness of the proposed solution. The work presented in this chapter has been summarized in [Xu, 2012(2)].

5.2 Literature review

5.2.1 Modeling of rough surface scattering

Scattering from rough surface is a topic of great importance and has been studied over decades. Many methods have been developed that model the problem with high precision by complicated techniques. Good summaries can be found in well-written books, such as [Beckmann, 1987; Ogilvy, 1991; Fung, 1994]. Following [Guo, 2010], here listed are just 1) modeling parameters of rough surfaces and 2) a few well-known approximation methods. Only modeling methods of static surfaces are discussed, since time-variant dynamic surfaces such as sea surface are out of our research scope.

Rough surfaces are most commonly modeled as groups of random points, or a 1D/2D random process. The properties of a random rough surface are characterized by statistical coefficients, such as mean, standard deviation (or variance) and autocorrelation coefficient. The mean value of a random rough surface is usually set to be zero for simplicity, while standard deviation provides a direct understanding of

surface roughness. Autocorrelation is yet another important coefficient that helps to describe the surface completely, since it tells whether the “hills and valleys” over the surface are closed together or far apart [Beckmann, 1987]. As shown in Fig 5.4, large correlation distance (distance where autocorrelation of the surface drop to a factor of e^{-1}, assuming a normal distribution of the surface) characterizes gentle slope change, while small correlation distance indicates rapid slope variation. Usually, correlation distance, together with standard deviation, is used to characterize the scale of the surface, with respect to the wavelength of incident electrical magnetic wave. Most approximations aiming to reduce the complexity of modeling must always specify their conditions of validation first, the most important of which is the scale of the surface under study [Beckmann, 1987].

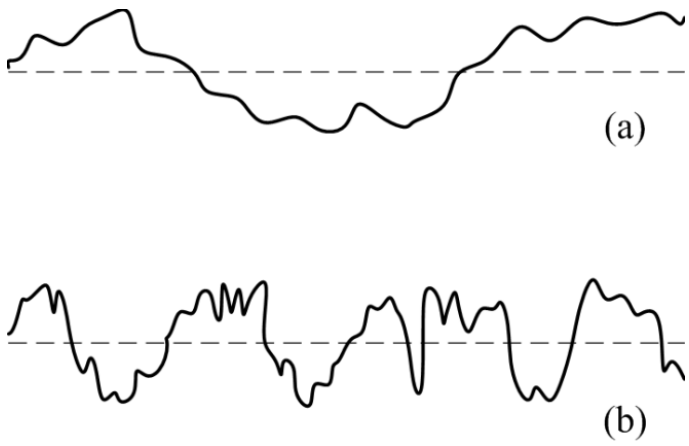

Fig 5.4 Correlation distance of a rough surface (same standard deviation): a) large autocorrelation distance; b) small autocorrelation distance

A fairly high accuracy solution of the scattered field can be derived via the integral equation method (IEM), which starts from solving electric magnetic equations with boundary conditions. The so called “Krichhoff approximation” (KA)

[Beckmann, 1987], which is probably the most well-known and most commonly used model of rough surface scattering, is a tangential approximation to IEM. KA can be used for only large scale surfaces, and with small incident angle, since it only considers singular reflection. Second order KA has been proposed to take multiple reflections and shadowing effect into consideration and thereby increase accuracy. For small scale surfaces, whose surface fluctuation is much smaller than incident wavelength, the small perturbation method (SPM) [Rice, 1951] is applicable. Two methods fill in the gap between large scale and small scale, namely, small slope approximation (SSA) [Voronovich, 1985] and two-scale approximation (TSA) [Wu, 1972]. The former is based on surface slope, and achieves high accuracy by expansion to higher orders. There is no real limitation on surface height difference scale. The latter decomposes a real surface into large-scale and small-scale components, and applies KA and SPM respectively. The small-scale result is then averaged over the large-scale result, leading to the final answer by TSA. Other approximation methods include, for example, Extinction theorem (ET), full wave algorithm (FWA) and phase perturbation technique (PPT), etc. [Guo, 2010]

These listed methods are more or less limited to singular scattering problems, turning a blind eye to many more complicated physical phenomena, such as multiple scattering, shadow effect, phase interference, and edge diffraction, to name a few. With the rapid development of computer science, numerical methods are more and more favored by researchers all over the world. Based on the type of equations to be solved, numerical methods can be discriminated as differential equation or integral

equation. Based on in which domain the problem is solved, they can also be recognized as frequency domain methods or time domain methods.

What we implement in this chapter, the so called "facet modeling" [Ulaby, 1982; Rees, 1990; Nouvel, 2004], is actually a Krichhoff approximation based numerical modeling method. A chief advantage of this method is its simplicity, allowing much swifter estimations for various kinds of apodized pupils. Furthermore, the method is considered accurate enough in our case:

1. Our incident angle is very close to 0, and our acceptance angle is relative narrow. This helps greatly to avoid components due to phenomena such as multi-scattering or shadow effect.
2. Common machined surfaces are of micron level roughness. Since measurement uncertainty of Shapix is also around 2μm, the scale of rough surface scattering here can be considered as "large scale" with respect to wavelength (around 0.85 μm).
3. In practice we set a 5μm facet scale in simulation, 1/30 of pixel coverage distance (150 μm). It can be inferred that the vertical / height uncertainty within a single facet is less than $2\mu m/\sqrt{30} \approx 0.37\mu m$, which is less than half of wavelength.

Points 2 and 3 above are listed in literatures as necessary requirements for "facet modeling" method.

Finally, a minor yet practical reason why "facet modeling" is favored in our study is that the majority of documented rough surface scattering methods use scattering coefficient for evaluation purpose, which often appears as a ratio of irradiance / power but has no phase information involved. Again, as we note that our signal of interest is phase rather than irradiance, "facet modeling" provides a relatively simple and easy-understanding tool for studying the problem.

5.2.2 Recent achievements and commonly applied metrics of pupil apodization in optics

From a more general point of view, apodization is a category of pupil modification. For the purpose of contrast enhancement, pupils can be modified in different ways. There are amplitude modified pupils [Kasdin, 2003], phase modified pupils [Yang, 2004; Kostinski, 2005; Codona, 2006] (kinds of phase plate) and even pupils modified for both amplitude and phase. There are aperture shape modified pupils (or named "shaped pupils") [Kasdin, 2003; Debes, 2002; Debes, 2004; Chakraborty, 2005; Cady, 2009], or aperture transmissivity modified pupils (apodized pupils). There are also symmetrically designed pupils [Vanderbei, 2003(1); 2003(2)] or asymmetrically designed pupils [Kasdin, 2005]. Since our study is looking for a low cost, relatively easy making, azimuthally symmetric solution, we have been restricting our scope within symmetrically apodized pupils. Although there are general concerns about the drawbacks of apodization [Guyon 2003], such as irradiance degradation (due to absorption) and reduced angular resolution (due to the

expansion of PSF main-lobe), to our task neither of them should be problematic. We have sufficient flux reflected from metallic surfaces, and resolution requirement of surface inspection is much lower than that in astronomical observations. However, we will still include as many interesting recent articles under the broad topic of pupil modification as we can in this literature review section.

A comprehensive review of the subject can be found as early as in 1964 [Jacquinot, 1964]. Due to the progress in manufacturing technology, since 2001, there has been a blooming in pupil modification related literatures, most of which are in the field of astronomical observation.

Nisenson and Papaliolios [Nisenson, 2001] first pointed out the interest of using apodized pupils to discriminate an extrasolar planet (exoplanet) from its star. They suggested in optical telescope the introduction of an aperture modifying both its shape (circular to triangular) and its transmission (crossed sonine), to achieve significant diffraction side-lobe suppression. The major difficulty is, of course, how transmission modification (apodization) can be physically achieved precisely.

Pupils with various shape and apodization curves are compared in [Kasdin, 2003]. It also provides a set of comprehensive metrics for evaluating pupils' performance in astronomy observation. Comparatively, asymmetric shaped pupils are easier to fabricate [Kasdin, 2005], if directional or regional high contrast is the target. However, if azimuthally symmetric PSF is the goal, the pupil is likely to be serrated, having rings or radiate bars wavelength-level thin. This is also a challenging and

expensive manufacturing task. Although theoretical tolerance analysis in [Kasdin, 2005] favors shaped pupils to apodized pupils, their suggested accuracy of shaped pupil bars is typically 25nm level for a 50mm aperture, since their goal is 10^{-10} contrast, which is a much higher requirement than our need. On the other hand, experimental results in [MacDonald, 2002] provided good proofs of the efficiency of apodized pupils, even with obvious transmission curve distortion. There are also articles reporting that from a signal-to-noise ratio (SNR) point of view, apodized apertures are favored comparing with shaped apertures [Aime, 2005]. The throughput of shaped apertures was reported more likely to contribute towards background, rather than the main-lobe of the PSF [Guyon, 2006].

Guyon first proposed an idea of beam apodization without loss of flux [Guyon, 2003]. The idea was developed further in several following publications [Guyon, 2005; Belikov, 2006]. By implementing a pair of aspheric mirrors at the entrance aperture, it is numerically proved that flux redistribution can be achieved. The two drawbacks of this proposed solution are: 1) strong off-axis imaging aberration and 2) difficulty in making the aspheric mirrors.

More recent articles emphasize mainly on experimental results as well as realistic engineering oriented analysis. Following the proposal of Aime in [Aime, 2002], Carlotti et al. [Carlotti, 2008] presented laboratory results, using a Mach-Zehnder interferometer to fulfill apodization. Abe et al. [Abe, 2008] demonstrated first experimental results on their fabricated multi-plateau pupil.

Sivaramakrishnan et al. [Sivaramakrishnan, 2008] provided an analysis of how phase aberrations in Lyot coronagraphs could be measured and corrected. Martinez and his colleagues published a series of articles [Martinez, 2007; 2008; 2009(1); 2009(2); 2010], recording systematically from principle, design, manufacturing, to test and experimental results of pupil apodized Lyot coronagraph (PALC). Although there are still many aspects that need to be improved in first-step experimental results, these efforts provide a real potential towards high contrast imaging in the field of astronomical observation.

Important applications of pupil apodization have been found in many other fields as well. Traditional applications such as laser beam reshaping had been reported 20 years ago [Aleksoff, 1991]. In 2002, MacDonald et al. [MacDonald 2002] proposed implementations of super Gaussian shaped pupil on environmental satellite for remote sensing purpose. Martinez-Corral et al. [Martinez-Corral, 2003] reported side-lobe suppression in confocal scanning microscopy by phase only pupil modification. The concept of apodization has also been used in imaging interferometric lithography [Tridhavee, 2004], to achieve high quality patterns for high volume manufacturing. In 2009, an application of super-resolution pupil mask, modifying both phase and amplitude had been proposed [Canales, 2009], to increase the data density of optical storage systems.

It is also beneficial to summarize some most commonly adopted metrics in existing literatures, as a reference during our work of establishing a different set of

metrics for phase signal in MWHI observation. [Kasdin, 2003] and many other literatures provide excellent materials for the following summary.

1. Contrast. The first and the most commonly adopted metric is contrast. Brown and Burrows [Brown, 1990] introduced the concept of "contrast quotient" Q, which is a ratio of the mean central irradiance of observation target (the planet, as in the exoplanet-star discrimination case) image to the mean irradiance of the local background, to evaluate the effectiveness of an exoplanet-detection system. It includes two terms: Q_{ss} from the star background and Q_{sc} from inner instrument scattering:

$$Q = (\frac{1}{Q_{ss}} + \frac{1}{Q_{sc}})^{-1} \qquad (5.1)$$

According to [Kasdin, 2003], Q should be a value not too small (with respect to 1), in order to achieve valid observation in practice. Assuming Q_{sc} is sufficiently large, it is then expected that Q_{ss} is a value larger than 1. Q_{ss} can be expressed as:

$$Q_{ss} = \frac{I_p}{I_s} \bullet \frac{P(0,0)}{P(\xi_p, \zeta_p)} \qquad (5.2)$$

in which I_p / I_s represents the ratio between peak irradiance of the planet and that of the star. Considering the PSF centered at the star, $P(0,0)$ stands for the center value of this PSF, while $P(\xi_p, \zeta_p)$ is the PSF value at the location of the center of the planet image. Since I_p / I_s can be as large as 10^{-6} to 10^{-10},

it is then often desirable in exoplanet detection that a PSF inherent contrast (or PSF contrast) C can be better than 10^{-10}, i.e.:

$$C = \frac{P(\xi_p, \zeta_p)}{P(0,0)} \leq 10^{-10} \tag{5.3}$$

2. Discovery space. A second metric is discovery space, represented by inner working distance (IWD) and outer working distance (OWD). According to [Kasdin, 2003], IWD is defined as the smallest angular separation (usually in a scale of several λ/d, wavelength/pupil aperture size) from the star for which the PSF contrast C reaches the required value (say, 10^{-10}). Together with the counterpart OWD, an azimuthal region where dark contrast is maintained is defined, which represents a space where the existence of an exoplanet can be convinced. Of course, different pupil modifications can have their own measure of discovery space. But in general, the concept of IWD is of more popularity since it marks a kind of upper limit of special detection capability. It has been commented that trade off can be possible, between IWD and discovery space (for example, small IWD at the cost of narrow discovery space) and some other metrics.
3. Integration time. This metric marks the necessary observing time to guarantee detection with a certain "confidence level", which is usually represented by signal-to-noise ratio. In [Kasdin, 2003], two types of formulas are derived to characterize integration time, both of which are based on statistical modeling of photon accumulation process. Their difference is that, by assuming a known background level, formula t_1 is much simpler than formula t_2, which is

assuming unknown background level and estimates both the objective planet and the background simultaneously.

Although integration time is considered as the most important metric in astronomical observation, it is not our priority to reduce time cost in our case. In general, signal reflected from metallic surfaces is strong enough to guarantee sufficient detection confidence. Our concern is more on the accuracy side, or can be understood as a "characterization" problem rather than a "detection" one, as defined at the beginning of section 3 in [Kasdin, 2003].

It is worth noticing that, to the best of our knowledge, there are relatively few analyse related to phase shift induced by apodization. According to [Kasdin, 2005], this is mainly because 1) it is practically difficult to measure the phase shift as well as to get it fitted to a model of reasonable accuracy and 2) the phase shift is varying according to the material used. [Kasdin, 2005] assumed a log shaped phase shift with respect to amplitude of field apodization function, while some others simply viewed apodization induced phase shift as "uncompensated phase aberration" [Abe, 2008] inherent to material. It seems reasonable to assume apodization induced phase shift as a kind of error, since analysis shows that their effect is not very significant [Kasdin, 2005; Abe, 2008], such as minor modifications of PSF curve that can be partially compensated when extremely high requirement on contrast is targeted.

5.3 Mathematical modeling of rough surface inspection in MWHI imaging system

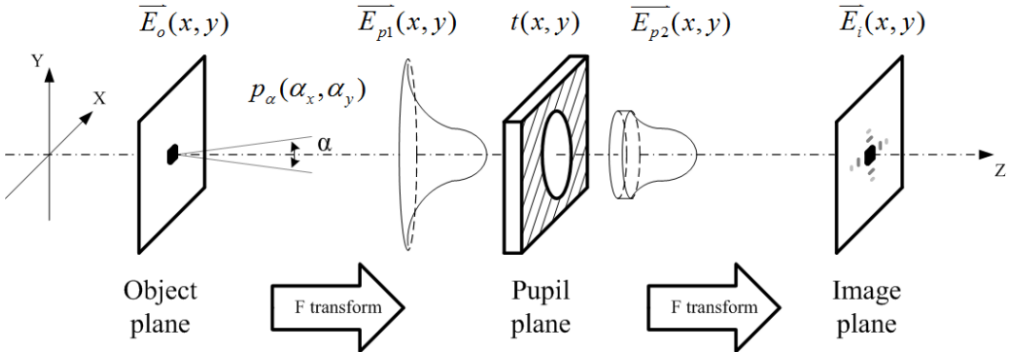

Fig 5.5 Process of surface inspection via MWHI imaging system

Fig 5.5 demonstrates the imaging process of rough surface inspection in MWHI system (comparing with the model used in previous chapters, the modeling work here gets pupil involved, yet assumes in-focus imaging). Suppose field distribution at the object plane is $\overline{E_o}(x,y)$, whose phase contains surface height information. The field right in front of the pupil plane, $\overline{E_{p1}}(x,y)$, can be viewed as a convolution of two parts: one is the Fourier transform of $\overline{E_o}(x,y)$, $\mathsf{F}\{\overline{E_o}\}(x,y)$, just the same as suggested by classical Fourier optics theory [Goodman, 1996]; the other part is a distribution function due to the randomness of facets. As suggested in the introduction section in this chapter, if the probability density function of facet orientation angle α is denoted as $p_\alpha(\alpha_x,\alpha_y)$, then the distribution function:

$$p_{pupil}(x,y) = p_\alpha(x/f, y/f) \tag{5.4}$$

where f is the total focal distance of the 1st lens group in Fig 5.3 (i.e., the parabolic mirror in current Shapix). $p_{pupil}(x,y)$ can be understood as the possibility of field $\mathsf{F}\{\overline{E_o}\}(\xi,\zeta)$ centering at position (x,y). By superposing all such chances together,

the convolutional relationship correctly describes the portrait of the optical field right before the pupil.

The pupil modulates the transmitted field in amplitude and phase simultaneously. According to [Kasdin, 2005], it is reasonable to assume a log relationship between amplitude and phase for $t(x,y)$, the field transmissivity function of the pupil:

$$t(x,y) = |t(x,y)| \exp[j \times \varsigma \log(|t(x,y)|)] \tag{5.5}$$

Where $|t(x,y)|$ is a ratio between 0 and 100%. The square of $|t(x,y)|$ results in irradiance transmissivity function $T(x,y)$, which is also between 0 and 100%. ς depends on the material coated to achieve apodization. According to data provided by our pupil manufacturer, as shown in Fig 5.6, curve fitting demonstrates good match at $\varsigma = -0.1993$.

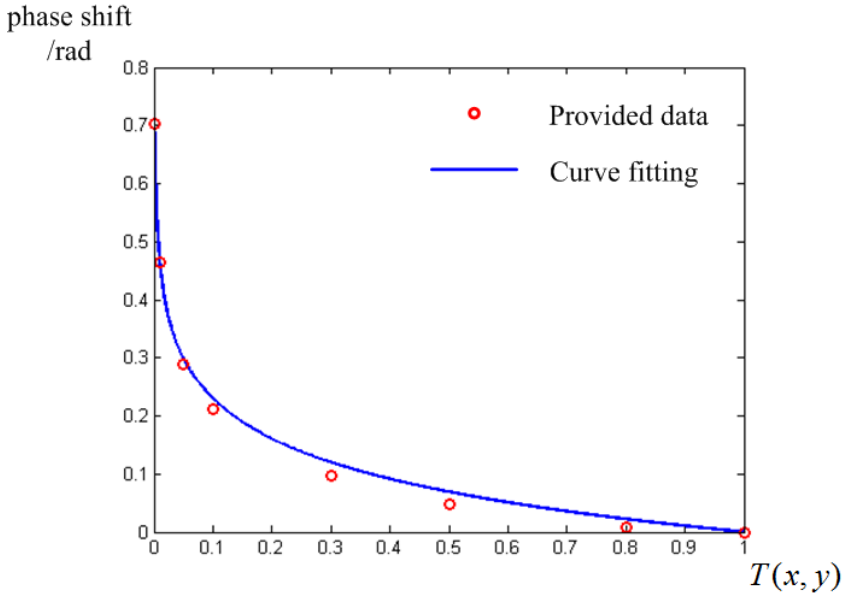

Fig 5.6 Curve fitting of phase shift vs. irradiance transmissivity $T(x,y)$

The field right after the pupil, $\overrightarrow{E_{p2}}(x,y)$, is thus:

$$\overrightarrow{E_{p2}}(x,y) = \overrightarrow{E_{p1}}(x,y) \times t(x,y) \tag{5.6}$$

and the field at the image plane, $\overrightarrow{E_i}(x,y)$, is just another Fourier transform of $\overrightarrow{E_{p2}}(x,y)$. In summary, we can conclude that:

$$\overrightarrow{E_i}(x,y) = \mathsf{F}\{\overrightarrow{E_{p2}}\}(x,y) = \mathsf{F}\{\overrightarrow{E_{p1}} \times t\}(x,y)$$

$$= \mathsf{F}\{\overrightarrow{E_{p1}}\} \otimes \mathsf{F}\{t\}(x,y) = \mathsf{F}\{\overrightarrow{E_{p1}}\} \otimes psf(x,y)$$

$$= \mathsf{F}\{\mathsf{F}\{\overrightarrow{E_o}\} \otimes p_{pupil}\} \otimes psf(x,y) = (\overrightarrow{E_o} \times \mathsf{F}[p_{pupil}]) \otimes psf(x,y) \tag{5.7}$$

where we denote $\mathsf{F}\{t\}(x,y)$, the Fourier transform of $t(x,y)$, as $psf(x,y)$. Indeed, square of the amplitude of $\mathsf{F}\{t\}(x,y)$ results in the traditionally defined point spread function (PSF, which describes intensity distribution at the image plane of a point source), a concept of critical importance in all kinds of imaging system.

$$PSF(x,y) = \left|\mathsf{F}\{t\}(x,y)\right|^2 = \left|psf(x,y)\right|^2 \tag{5.8}$$

5.4 Metrics of pupil optimization in MWHI

In this section, we are going to define a set of metrics, to pick out a preferable transmissivity function from a bunch of candidates. As described in the introduction section, the metrics we need should be different from what have been used in many previous applications, since the signal of interest in our case is phase, rather than amplitude or irradiance in other cases.

The evidence of stray light reduction in MWHI is straightforward: less affected area while sufficient accuracy of height or phase at the origin pixel. From the previous mathematical derivation (Eq. 5.7) we see that the concept of PSF still comes into play since it acts as an individual convolutional part in MWHI imaging. Metrics related to PSF are thereby still valid in describing how energy of an ideal point source affects neighboring area. Here we inherit the usage of ***contrast / stretching distance*** as a metric to describe how far one point source will affect. Instead of integration time, we employ ***absolute/percentage encircled energy*** to describe the concept of "valid" throughput, which helps the system to achieve sufficient irradiance. To create a measure of signal strength, which here means phase modulation amplitude, we introduce ***modulation depth*** as a new metric. To simulate phase accuracy, we go through Monte Carlo trials and characterize ***standard deviation of phase shift*** as our last metric.

5.4.1 Contrast / stretching distance

As described in Eq. 5.3 in section 5.2.2, traditionally, PSF contrast is defined as a ratio between the strength at a neighboring point to that at the center of the PSF. In astronomical observation it is desired to be a ratio as low as 10^{-10}, which makes the design and manufacturing of the pupil really a challenging engineering task. In MWHI surface inspection, the threshold does not need to be that low: assuming roughness induced field strength difference between smooth / rough surfaces is η_1, to make stray-light induced phase shift less than η_2, a further degradation of η_2 is

necessary between the field of stray light and the local optic field by the rough surface (Fig 5.7). Therefore, the total required field contrast is $\eta_1 \times \eta_2$, and the requirement on PSF contrast is $(\eta_1 \times \eta_2)^2$. Experimental results of aluminum deck face and its neighboring cast areas suggest that η_1 is typically around 10%. Supposing $\eta_2 \approx 0.01$, which is a common level of Shapix's phase noise, then the necessary PSF contrast is around 10^{-6} to 10^{-7}.

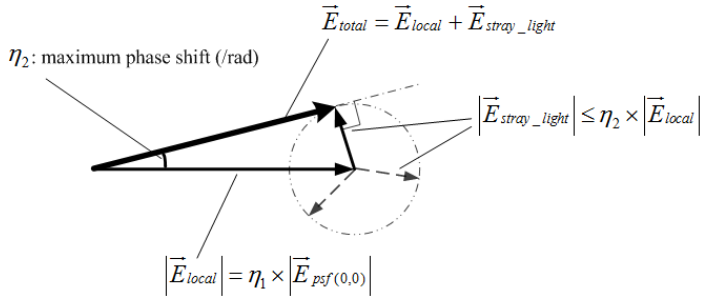

Fig 5.7 Stray field induced phase shift

In practice, we combine PSF contrast with the concept of inner working distance (IWD, [Kasdin, 2003]) to form stretching distance, a metric of distance in the image plane, estimating how far away would the PSF of a certain apodization curve stretch, before it goes below a given contrast threshold. The shorter this distance is, the better the apodization curve is considered.

5.4.2 Encircled energy

Fundamentally, the strong concern of integration time in astronomical observation is for the purpose of accumulating sufficient irradiance throughput, as pointed out in [Kasdin, 2005]. Since the actual integration time is not a bottleneck in

our MWHI imaging system, we turn to its surrogate to take into consideration of power accumulation in our metric. Encircled energy is defined as the amount of energy / irradiance falls into a certain area. It can be given in an absolute value, by integrating the PSF function over the selected area; or be given as a percentage, with respect to the total energy conveyed to the imaging plane from the point source (i.e., an infinity to infinity integration of the PSF). As a common practice, many imaging systems select their pupil so that the size between the first nulls of its PSF is of a certain proportion to detector's array pixel size [MacDonald, 2002]. It is then reasonable to make the pixel centered at the PSF as the selected integrating area. In this case, the absolute value of encircled energy marks the amount of "valid" throughput of the pupil. We here highlight the concept of "valid", because reports have pointed out that not all increase in throughput is helpful [Aime, 2005; Guyon, 2006]: some may just result in brighter background and thereby make detection even harder. Percentage encircled energy emphases just this point: the higher this percentage is, the lower amount of stray-light it would produce.

We will employ equal absolute encircled energy within one centered square pixel area (150μm by 150μm, covers the full width half maximum, FWHM, of the Airy disc by the current 4mm circular pupil) as a rule to regularize dimensions of different apodization curves. Percentage encircled energy is introduced as a secondary metric of characterizing stray light stretching properties of pupils.

5.4.3 Modulation depth

Modulation depth reveals how much the modulated variable of the carrier signal varies around its unmodulated level. Generally speaking, this concept is applicable to all kinds of situations where variation (phase) is recognized as signal, including the case of MWHI imaging. By denoting the ratio between the largest magnitude and the carrier amplitude, it gives a good measure of relative signal strength. Recall the fundamental interferometric equation Eq. 2.1:

$$I(\varphi) = I_{obj} + I_{ref} + 2\sqrt{I_{obj} I_{ref}} \cos[(\gamma_{obj} - \gamma_{ref}) - \varphi]$$

The first two intensity terms give an offset, while the magnitude of cosine interference term marks signal strength. Theoretical modulation depth can then be given as:

$$\frac{2\sqrt{I_{obj} I_{ref}}}{I_{obj} + I_{ref}} \times 100\% \tag{5.9}$$

while in reality, taking integration effect of pixel size as well as noise factors into consideration, a commonly conducted practice (as we here follows the concept of "visibility " in [Born and Wolf, 1999]) is a sinusoid curve fitting followed by:

$$\frac{I_{\max} - I_{\min}}{I_{\max} + I_{\min}} \times 100\% \tag{5.10}$$

where $I_{\max}$ and $I_{\min}$ represent the maximum and the minimum in the curve. In our case, we regularize the strength of the reference field to be the same as that of the

original object field. By testing a sequence of different surface roughness (characterized by the standard deviation of facet orientation angle, whose distribution is assumed to be Gaussian in both x and y directions for generality and simplicity), each pupil can give out a modulation depth curve according to surface roughness. Values at certain roughness along the curves are of interest, but we would like to emphasize more on the slope tendency side: a more gentle modulation depth curve indicates a smaller difference between rough and smooth surfaces, leading to better endurance towards surface quality variation.

Although articles ([Tanner, 1976; Kierkegaard, 1996]) reveal that the standard deviation of facet orientation angle of machined metallic surfaces can be as large as tens of degrees, we have decided to restrict our angular standard deviation from mirror like (632.8nm / inch, approximately 0.001 degree) to 2μm/150mm, approximately 0.8 degree. 2μm is Shapix's system height measurement uncertainty over a single pixel, while 150mm is pixel size in the object plane. As the half acceptance angle of the current imaging system is 2mm(radius of circular aperture)/744mm(focal length of the parabolic mirror), which is approximately 0.15 degree, most reflected flux over the selected angle range will simply be blocked by the aperture and imposing almost zero influence over the image plane field.

5.4.4 Standard deviation of phase shift

A very direct way to simulate pupils' performance is to generate the image plane field in Monte Carlo trials and detect phase via virtual phase shift interferometric (PSI)

processes. That is, 1) Starting with assumed facets orientation and simulating the imaging process, field distribution in the imaging plane can be depicted in facets; 2) Following similar PSI steps to those in the detection of modulation depth, an integrated / weighted phase over a single pixel can be generated; and 3) Repeating the above process would result in a trial of such phases. The mean shift of these phases towards the original object plane phase is of minor importance, since a common mean shift among different wavelengths is most likely to be compensated for; however, the standard deviation of these phases marks the uncertainty of the phase acquiring process, which can be used as a measure of the risk of getting outliers.

In the Monte Carlo test, the size of facets is selected to be 5μm by 5μm, 1/30th of the dimension of a single pixel area in the object plane. This size is picked because:

1. It is large enough to satisfy the requirement of "facet modeling", comparing with wavelength 850nm.
2. It is close to the level of roughness (micron level lateral spacing), which is the common scale level for most machined surfaces.
3. 30 by 30 would be large enough to represent a random process.

5.5 Comparison of different pupils via numerical simulation

We have simulated the performance of 5 types of pupils, all of which are azimuthally symmetric. Their power transmissivity functions $T(r)$ are:

1. Circular (regular): $T(r) = 1 \quad 0 \le r \le a_0$

2. Triangular: $T(r) = (a_1 - r)/a_1 \qquad 0 \le r \le a_1$

3. Gaussian: $T(r) = \exp[-(r/a_2)^2] \qquad 0 \le r \le 2.0a_0$

4. Super-Gaussian [MacDonald, 2002]: $T(r) = \exp[-2(r/0.9a_3)^4] \qquad 0 \le r \le a_3$

5. 5th order Sonine [Nisenson, 2001]: $T(r) = [1-(r/a_4)^2]^{\nu-1} \qquad 0 \le r \le a_4, \ \nu = 5$

a_1 to a_4 are characteristic dimensions that need to be regularized according to a_0 before comparison. In practice, a structure induced upper limit on radius r of all pupils is $2.0a_0$. From an experiment design point of view, there can be more than one ways of regularization and comparison based on the metrics described in the previous section. However, some of the ways of regularization, such as minimizing contrast, would simply drive dimension optimization to extreme values. Here we choose to regularize pupils by equal absolute encircled energy, and compare them in contrast, percentage encircled energy, modulation depth and standard deviation of phase shift. The dimensions after regularization are: $a_1 = 1.45a_0$, $a_2 = 0.80a_0$, $a_3 = 1.23a_0$ and $a_4 = 1.85a_0$.

Fig 5.8 to Fig 5.12 demonstrate the transmissivity curves and PSFs of the pupils. Upper left are 2D pupils $T(x,y)$; upper right are 1D azimuthal slopes, whose X scales are regularized in unit of a_0. Lower left are PSFs of $T(x,y)$; lower right are 1D azimuthal slopes of the PSFs, whose X scales are regularized in unit of pixels (this is different from common deed of using angular units λ/d, yet more convenient in an engineering system). Threshold of contrast is selected to be 10^{-6}, and marked as dash-dotted lines in the 1D PSF pictures. The dashed lines are PSF curves if no phase

delay is introduced by pupil apodization, i.e., pure amplitude modulation. Performance metrics of percentage encircled energy and contrast are summarized in Table 5.1.

	Stretching distance (/pixel) PSF Contrast threshold: 10^{-6}	encircled energy (percentage)
Circular	>15	53.18%
Triangular	11.1	76.41%
Gaussian	5.1	83.61%
Super Gaussian	3.3	70.36%
5th order Sonine	3.6	78.16%

Table 5.1. Stretching distance and percentage encircled energy comparison

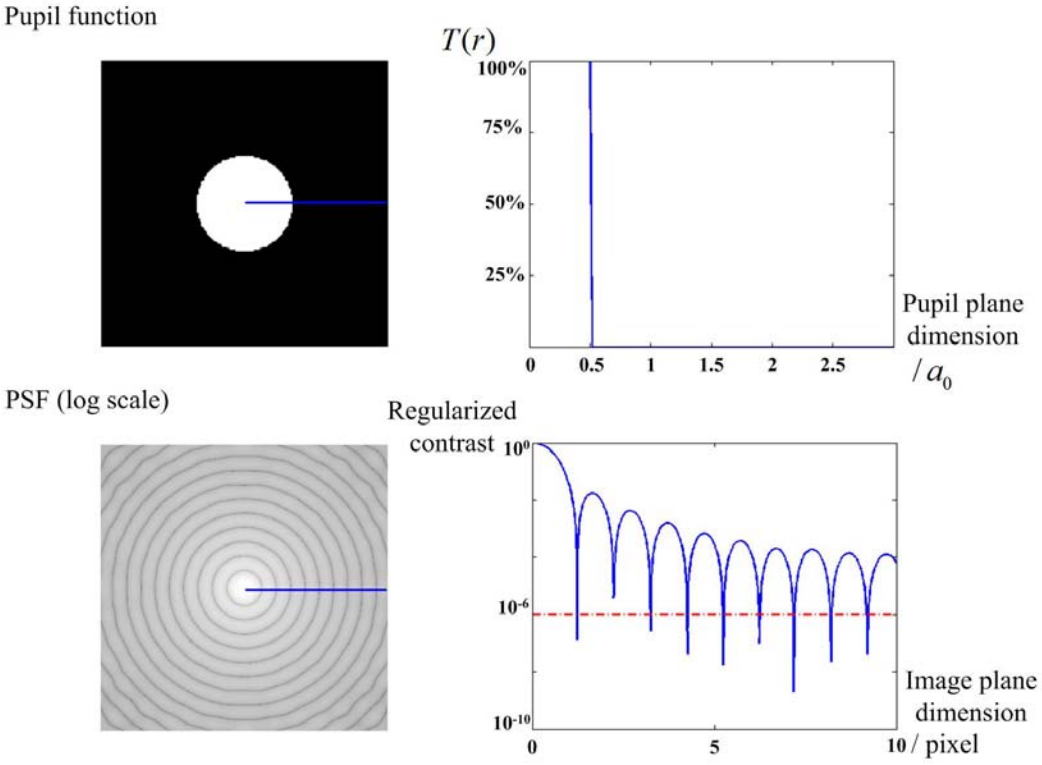

Fig 5.8 Circular pupil and its PSF (in log scale)

It can be observed that regular pupil introduces very strong side-lobes, which are significantly damped in apodized pupils. Super Gaussian and Sonine pupils produce most significant contrast, making stretched lights limited within 4 pixels. Gaussian pupil produces slightly longer “tails”, while triangular pupil produces much longer ones. It is also observed that taking phase delay into consideration modifies PSF curves slightly, most evident at nulls of the PSFs. The influence of such modifications is limited in our study.

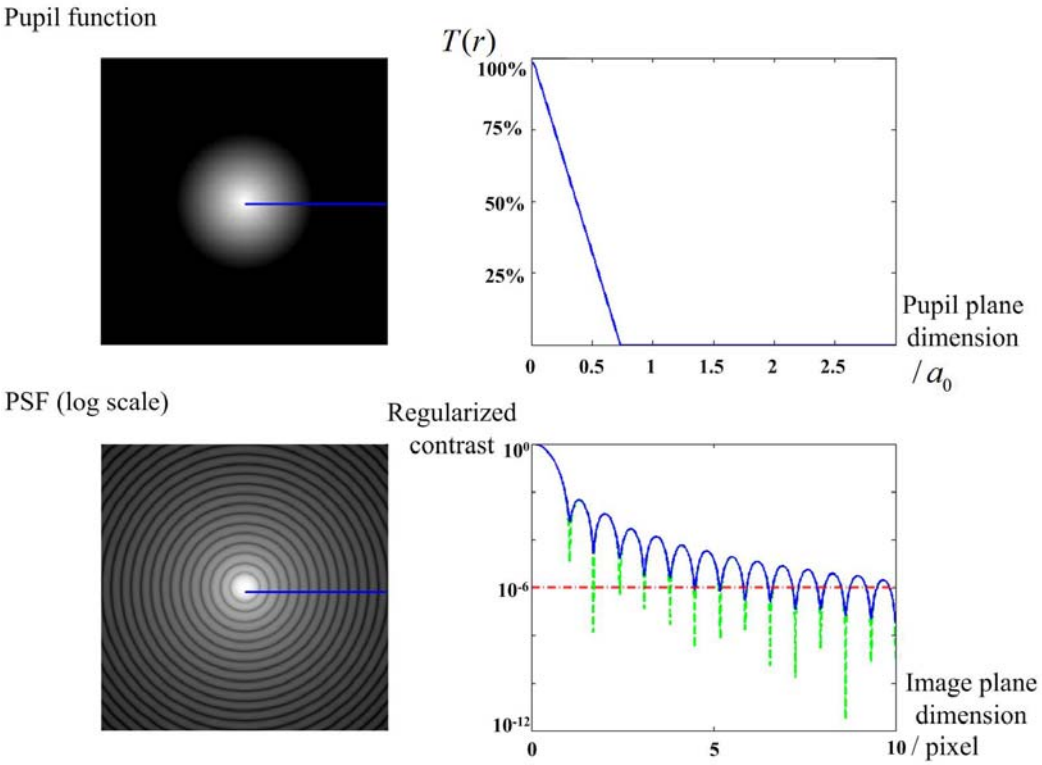

Fig 5.9 Triangular pupil and its PSF (in log scale)

From percentage encircled energy data shown in Table 5.1, it is clear that the center pixel of circular aperture only collects a little more than half of the total

irradiance. Over 45% of the energy goes to neighboring pixels and becomes stray light. All apodized pupils do much better than that, about 15% to 30% leakage. The current Shapix system is arranged to cover FWHM of the circular PSF in a signal pixel, rather than in a more common null-null way (which means to double the pupil size. This is prohibited by mechanical interference and geometric aberration in practice). In a null-null case, circular pupil collects 83.4% of the total energy, while apodized pupils collect over 95% to 99% in general, offering a more evident improvement to the circular pupil.

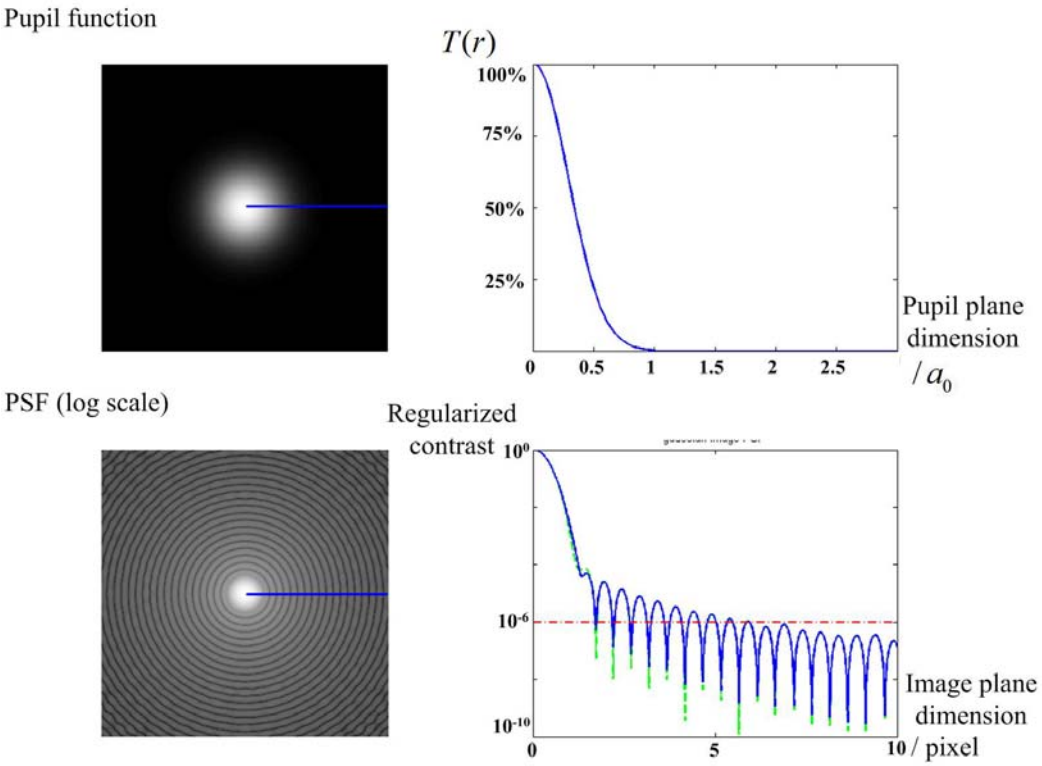

Fig 5.10 Gaussian pupil and its PSF (in log scale)

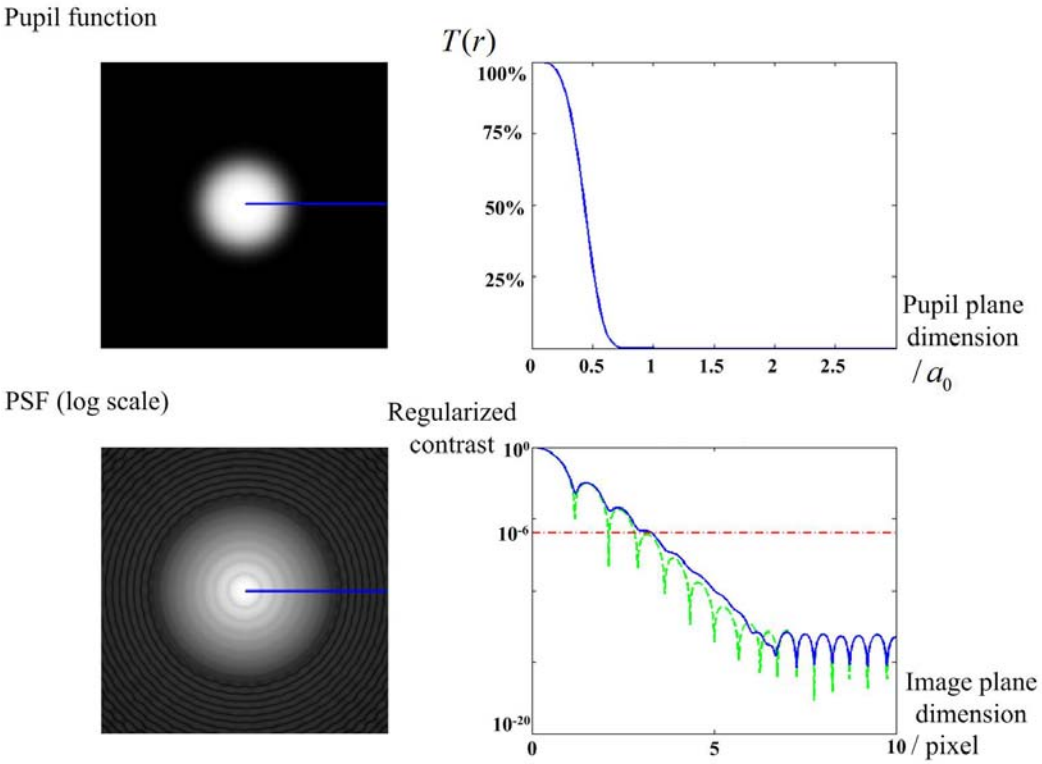

Fig 5.11 Super-Gaussian pupil and its PSF (in log scale)

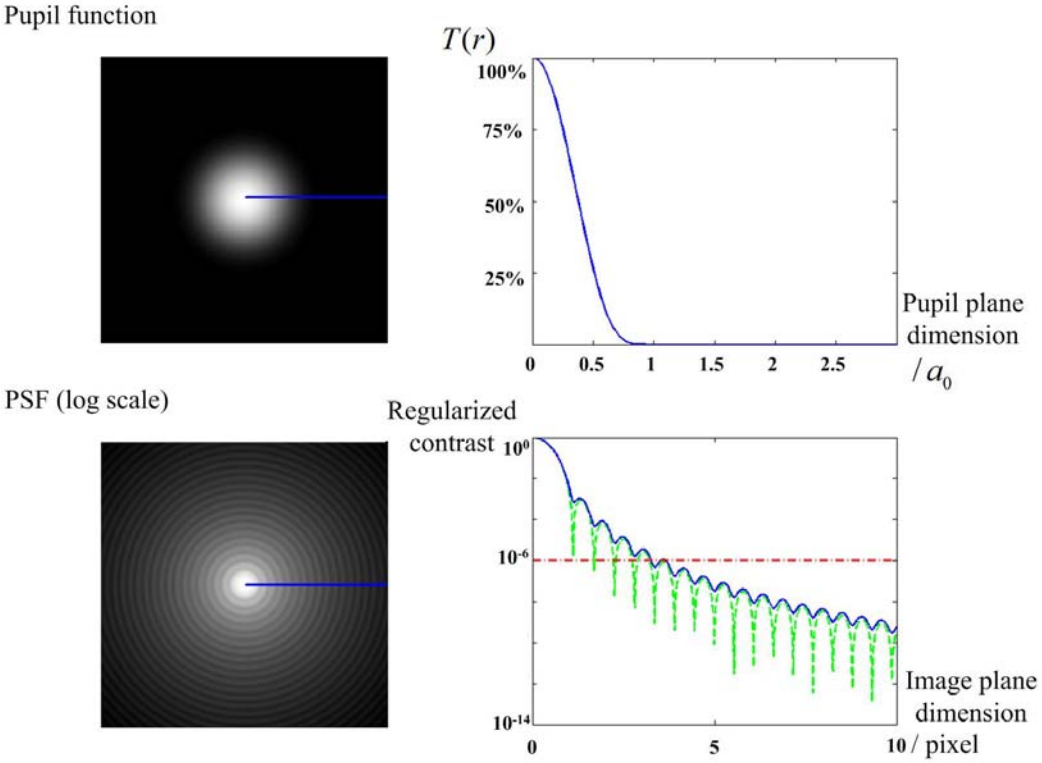

Fig 5.12 Sonine pupil and its PSF (in log scale)

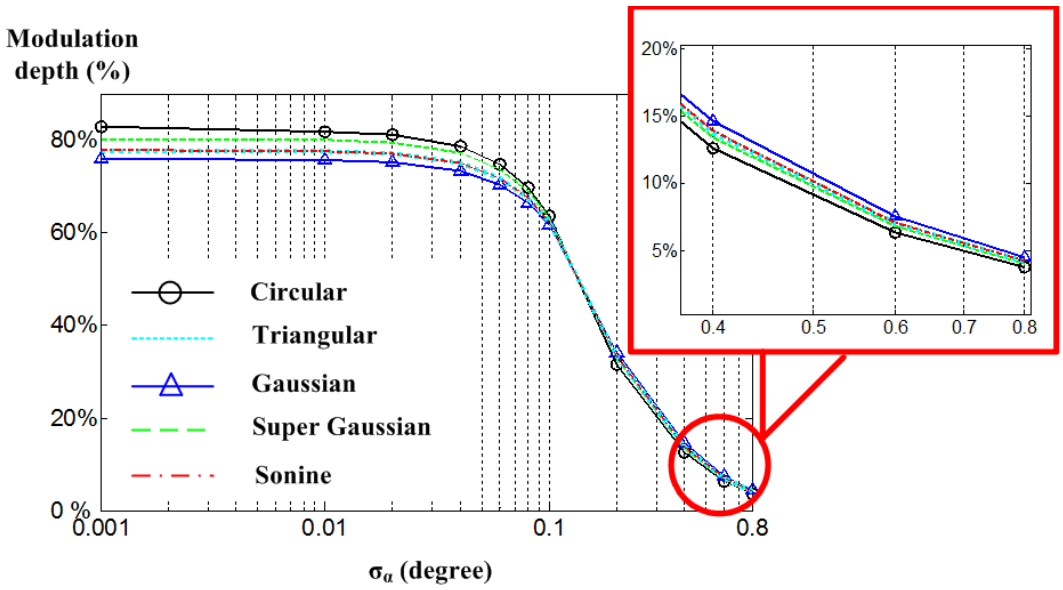

Fig 5.13 Modulation depth variation according to surface roughness

Fig 5.13 gives modulation depth curves of roughness range σ_α (standard deviation range of facet orientation angle) from 0.001 degree to 0.8 degree. In general, for all the pupils, modulation depth is decreasing with the increase of surface roughness. More specifically, as can be seen in the figure, circular pupil provides the highest modulation depth at mirror like surfaces, yet comes to the lowest at rougher surface finish. This indicates a sharper variation between smooth and rough surfaces, which is not favored by the need of measuring them next to each other. The gentlest slope is provided by Gaussian pupil, which can be considered as the most favorable by the modulation depth metric.

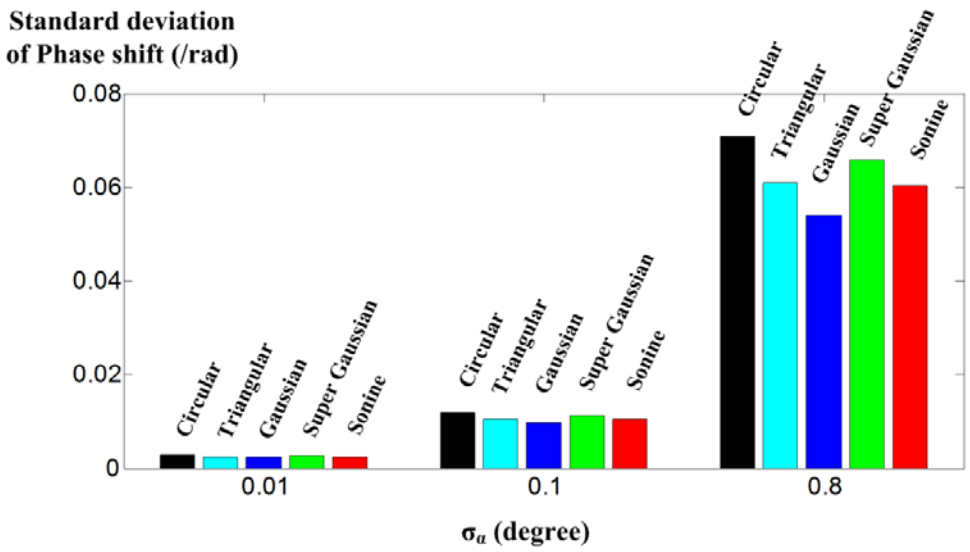

Fig 5.14 Standard deviation of phase shift at selected roughness level

Fig 5.14 shows phase shift standard deviation of all pupils at σ_α of 0.01 degree, 0.1 degree and 0.8 degree, respectively. As smaller standard deviation indicates better stability for the given surface finish, Gaussian pupil is again considered superior compared with other pupils, especially when the surface quality is rough.

In summary, we consider Gaussian pupil apodization to be the best, under regularization criterion of absolute encircled energy.

5.6 Experimental results

A Gaussian apodized pupil is manufactured by Raynard Corp. The apodization layer is coated over one side of a piece of flat glass. Test results of its $T(r)$ is shown in Fig 5.15 ($a_0 = 2mm$).

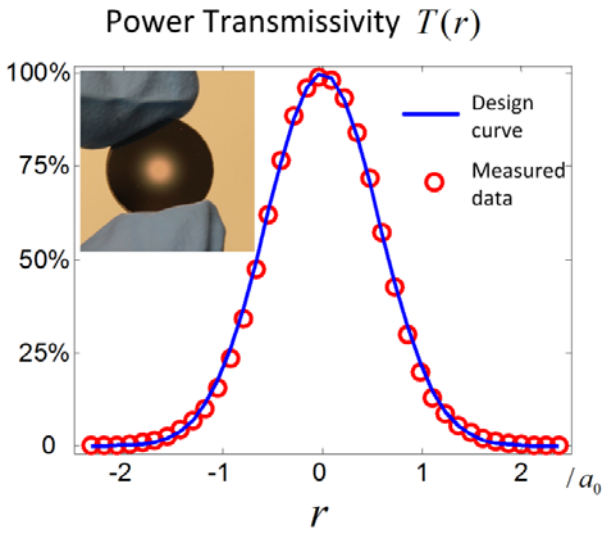

Fig 5.15 measured $T(r)$ of the Gaussian pupil

A S-22 micro-finish comparator has been measured, as shown in Fig 5.16. Log of PSI intensity difference, holographic phase and 3D measurement proflie by the Gaussian pupil are listed in Fig 5.17. For comparison, corresponding maps by a circular pupil are also listed. Evident irradiative stray light can be observed on the circular-pupil side around the mirror-like 2 micron-inch lapped surface. This stray light leads to spreading phase fringes towards neighboring dull rougher areas. The consequential smearing effect, i.e., area over the dull surface which is "measured" to have the same height as the neighboring shiny surface, is obvious. On the Gaussian pupil side, stray light is restrained from spreading, and surface areas are measured of their corresponding heights.

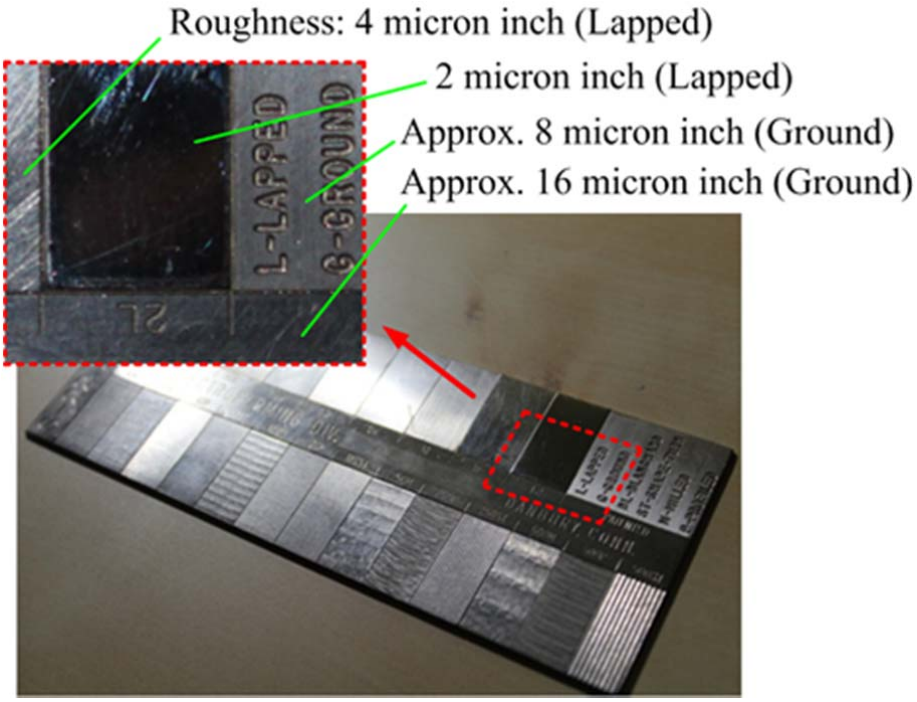

Fig 5.16 S-22 micro-finish comparator to be measured

5.7 Conclusion and future work

In summary, pupil apodization has been proven effective in MWHI imaging system to prevent smearing between surfaces of different quality. Differences in signal of interest lead to coherent modeling of MWHI surface inspection process, which consequentially innovates new evaluation metrics for pupil apodization functions. Nevertheless, there are some drawbacks in the current pupil apodization arrangement that needs to be overcome in the future. For example, the apodized pupil introduces two additional reflective surfaces in the system (the upper and lower surfaces of the glass base), which would deteriorate measurement result by multi-reflection. Small dirt or defects over the apodization coat would be another important cause of measurement quality degradation.

Future development of the research can be conducted to overcome the drawbacks, such as to quantify the influence of coating quality over measurement result, as well as to try directly coating apodization layer over the beam cube to avoid the usage of glass base. Theoretical development may lie in optimizing pupil transmissivity for sharper contrast as well as for more gentle modulation depth curves.

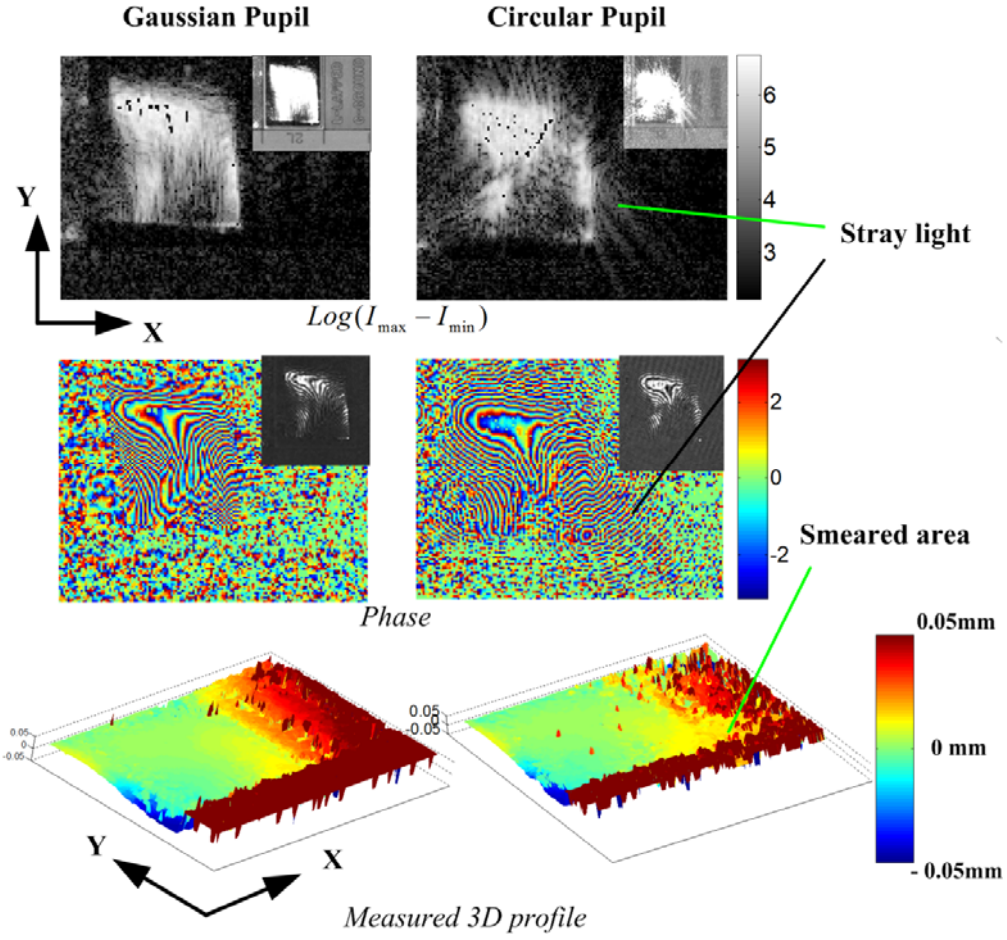

Fig 5.17 Log of PSI intensity difference, holographic phase and 3D measurement profile by Gaussian pupil (right hand side) and regular pupil (left hand side)

Chapter 6

Conclusions and Future Work

6.1 Summary

The research conducted in this doctoral study focused on further developing the multi-wavelength holographic interferometry (MWHI) technique, aiming to a practically viable solution for high quality 3D shape reconstruction tasks.

Digital refocusing has been proposed as a solution of depth-of-field limitation. Three correlated subtasks are studied, motivated by the goal of profiling clearly large-scaled object or multiple objects isolated in the axial direction. The first subtask focused on the accuracy and repeatability of reconstructed multi-wavelength 3D map. The traditional single wavelength refocusing formula has been revised to keep wavelength error induced phase perturbation low, so that phase mismatch can be avoided. An experimental proof has been provided that the repeatability of refocused height map can be as high as 2 microns, and the reconstructed shape profile is in satisfactory consistence with in-focus measurement. The next subtask aims to work out a phase contrast based focus detection criterion, which helps to determine refocusing distance whenever it is not given as prior knowledge. Weak feature detection capability has been highlighted in this subtask. Experiment has shown that

the new criterion developed especially for 3D maps possesses a good potential to outperform many now existing criteria. The last subtask combines the results of the first two subtasks, and deals with detecting multiple target objects with high accuracy simultaneously. The idea is based on the concept of extended focus imaging (EFI) in microscopy field. Relative refocusing distances are derived via interferometric distance measurement, while sharpness focus detection needs only to be performed once. This is especially beneficial for weak feature or featureless targets, as demonstrated in an illustrative experiment of plateaus with tooling marks.

Pupil apodization has been introduced to overcome smearing effect between neighboring surfaces of different reflection property. Based on reflection modeling of facets and mathematical derivation, the origin of smearing phenomena is properly explained. Differences between the goal in MWHI surface inspection and that in astronomical observation tasks have been emphasized. Specific metrics have been chosen to evaluate different pupil types and parameters. By installing a Gaussian apodized transmissive filter as a new system pupil, evident reduction of smearing effect has been experimentally demonstrated.

6.2 Future work

Future study of this dissertation may include the following aspects:

In further developing the MWHI refocusing technique, wavelength combination to enhance measurement robustness against random wavelengths fluctuation is a topic

of high interest. The fact that height scanning equation 2.6 is ill-posed is considered as a major limitation of measurable range of MWHI. Although [Yu, 2011] has proposed calibration techniques to overcome wavelength uncertainty, a mathematically more in-depth understanding of wavelength combination selection is still to be discovered, aiming towards an optimized practical solution of measuring large-scaled objects with sufficient accuracy.

Another topic of interest derives from further developing the phase contrast based focus detection criterion. Performance exploration for "marginal" conditions, with object features between gentle and step-like, would be of high practical value. What also important is to study the root cause of error (i.e., aberration, diffraction, and other imperfection of the optical system) between detected focus position and physical focus position, and to make it properly compensated by calibration programming. Further improvement of detection accuracy may involve development of new algorithms, such as sub-pixel shifted, non-blind / blind deconvolution for complex field, as briefly surveyed in the appendix section.

Implementation of Gaussian apodized pupil in this dissertation is a first step of the study to improve inspection quality over objects of different surface conditions. There are still many engineering works needed before what has been proposed here can be successfully implemented for industry applications. Further academic works, such as more detailed mathematical modeling of rough surface scattering, and impact of inner pixel area integration over acquired phase information via PSI, will help

greatly to the understanding of fundamental questions about interferometric measurement. Optimized design of phase apodized filter would also be of theoretical and experimental interest.

6.3 Academic contributions

Major academic contributions of this doctoral research can be summarized as follows:

First, the modification of traditional refocusing formula to exclude the axial propagation phase term in MWHI is novel. Traditional refocusing formula, in general, consider this term as dispensable, simply because that in most single wavelength cases, a common phase shift error is of little influence towards observation targets. In MWHI, however, phase matching among different wavelengths are of critical importance. Thus the elimination of $\exp(-j2\pi d/\lambda)$ is mandatory.

Second, phase contrast based focus detection criterion for MWHI is newly proposed. With the great expansion of unambiguous measurement range by MWHI, the problem of phase wrapping in previously proposed phase contrast based focus detection criteria has been overcome. Focus detection of phase objects no longer has to be correlated with their amplitude distribution.

A combination of the above two innovations evokes a systematic strategy of generating high accuracy, high clarity 3D profile of large-scaled object or multiple objects distributed in a wide image depth range. Distance measurement via MWHI is

much more accurate than block-by-block focus detection, and thus capable of preserving the 3D profile from distorting. Furthermore, since such distance measurement does not have to be point-by-point, the proposed strategy is expected to have promising time efficiency.

To the best of the author's knowledge, the smearing phenomenon among different surface conditions is addressed for the first time in MWHI. The introduction of pupil apodization into MWHI is thus considered as another innovation of this dissertation. Mathematical model has been created to address the origin of the smearing effect in practice. The influence of apodization towards randomly oriented facets has been simulated. And parameter optimization metrics have been deliberately selected to address the difference in signal of interest.

Appendix

Thoughts of Further Improving Lateral Resolution of Synthetic Height Map via Sub-pixel Method

A.1 Introduction

In this appendix, an idea of further improving lateral resolution of the synthetic height map will be discussed, as a possible future work of the proposed study in this report.

In incoherent imaging, aiming to achieve even better lateral resolution than already in-focused, small aberration cases, people employed sub-pixel shift to gather multiple captures, so that an improved sampling rate over the physical limit by the array device (such as CCD) can be achieved. The idea of "sub-pixel shifting" makes use of the periodicity of the imaging array, by moving a fraction of one pixel and taking a capture at a time. A typical "Sub-pixel shifting" strategy may include the following steps [Xu, 2007] (As shown in Fig A1):

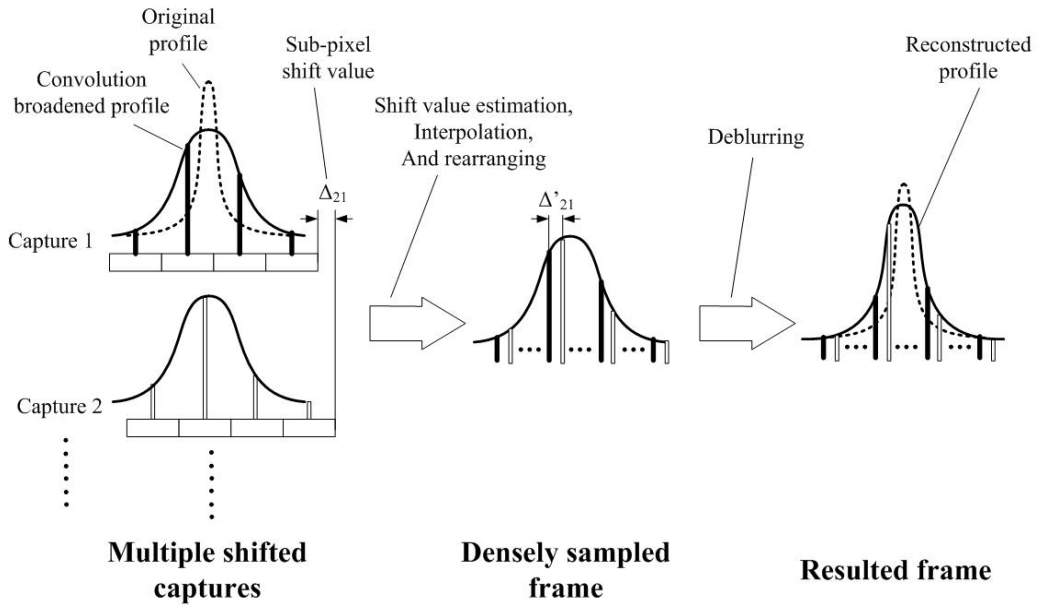

Fig A1 "Sub-pixel shifting" strategy

1. Physical shifting and take captures. Shifting factional to a pixel size can be done by changing the optical imaging system either mechanically or non-mechanically.

2. Estimate the shift value and do necessary compensation. In practical cases, the shifting can be inaccurate and the corresponding capture of the object is not ready to put into the up-sampled imaging grid. Thereby it would be notice worthy how a certain capture is shifted / deformed from the others. Compensation should be carried accordingly if necessary. For example, if the shifting is too far away from the supposed fraction, an interpolation may be carried out, although doing so will more or less sacrifice authenticity.

3. Arrange the captures into an up-sampling grid and form a densely sampled frame

4. Post processing. Based on the up-sampled frame, further deblurring work can be

done. The influence of detector array over the object image can be understood as two folded: on the one hand, it provides a special sampling interval limit, which limits details finer than the sampling interval via aliasing error; on the other hand, the integration effect over each single pixel area provides a convolution blurring effect, which further degrades image quality. While sub-pixel up-sampling aims to cure the former, the latter can be alleviated by deblurring. Besides pixel integration induced blurring, there are also other causes of blurring, such as aberration, diffraction object dithering etc., which may also be observed in the up-sampled frame, and can be alleviated by deblurring. Deconvolution is a most commonly employed deblurring process in dealing with incoherent imaging.

An example of how "Sub-pixel shifting" strategy works can be seen from Fig A2, where a dent over a transmission valve body is being observed.

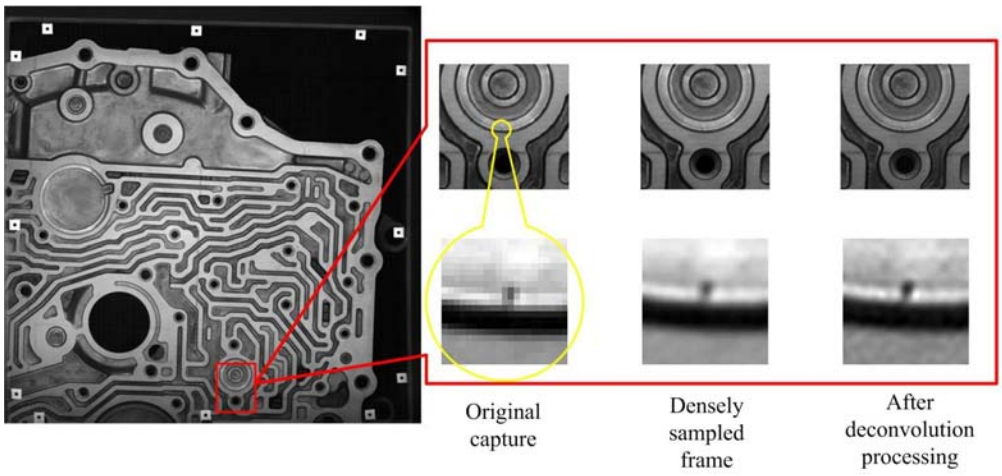

Fig A2 Effect of sub-pixel shifting under incoherent illumination (dent observed on a transmission valve body)

It would be worth trying to see if sup-pixel shifting helps in generating a finer

multi-wavelength synthetic 3D map. There will be major changes to the above described process which works for incoherent imaging (where lights add up as non-negative scalars, which are always constructive), since synthetic height map generated via interferometry is basically coherent imaging (where lights add up as vectors, resulting in either constructive or destructive effects). Several challenges need to be addressed:

Firstly, in coherence imaging, surface quality directly affects the amplitude / phase information captured by forming speckles [Goodman, 2006]. Additional to the often concerned artificial intensity contrast, it may also generate phase problem for sub-pixel shifting. An extreme example shown in Fig A3 can explain the situation: Suppose areas A, B and C are to be imaged via the sub-pixel shifting process under coherent illumination. Area A and C are rough. Lights reflected by these two areas add destructively and they look dim. As a result, two very weak (almost zero) vectors stand for area A and C. On the other hand, area B is smooth, appears to be shiny due to the constructive adding of lights from it. A strong vector is thereby applied to represent area B. In the sub-pixel shifting process, area A and B are first captured. Then, after shifting the camera a fraction of pixel, area B and C are captured. In such cases, phase information from area B dominates both before and after. No additional information will be acquired via sub-pixel processing.

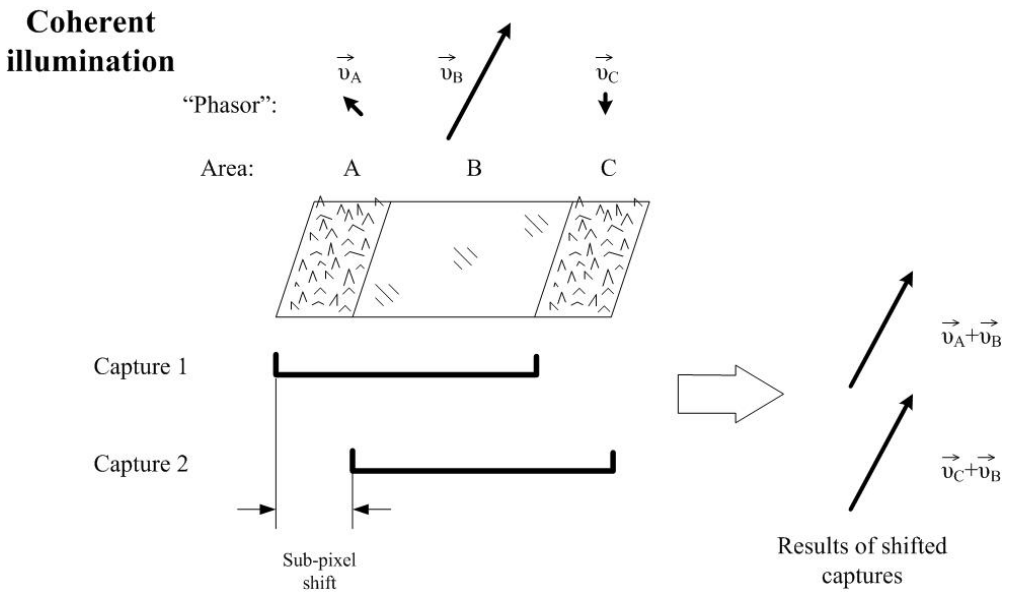

Fig A3 Effect of sub-pixel shifting under coherent illumination depends heavily on surface quality

Secondly, in coherent imaging, estimating the shift to sub-pixel level accuracy may be difficult. Most shift estimation algorithms developed for incoherent imaging (Briefly reviewed in section A.2.2) depends on the edge information. In synthetic 3D map, edges stand for where profile changes suddenly. Unfortunately, these areas are most likely to be where outliers appear, and where surface quality changes. Such uncertainties along edges in coherent height map may deteriorate the efficiency of now existing shift estimation algorithms significantly. As a matter of fact, the uncertainty on edges is also a major cause of why lateral resolution of coherent images usually does not look as good as that of incoherent ones.

Thirdly, commonly adopted deblurring process may not be suitable for coherent images. Deconvolution, typically, as briefly reviewed in section A.2.1, is faced with at least the following constraints:

- Deconvolution requires a constant / semi-constant convolution kernel. This is achievable in incoherent imaging as the dependence of blur characteristics over features is not evident. However in coherent imaging, the kernel may vary evidently from point to point, depending on local surface quality, edge features, and so on.
- Deconvolution generates artifacts around edges. Although people developed all kinds of attenuating algorithms to make artifacts "invisible", it will definitely be an unacceptable drawback for metrology purpose.

A. 2 Literature review:

Many literatures in coherent illumination related fields, such as radar, medical, ultrasonic imaging, and in phase information processing fields, such as phase retrieval [Fienup, 1982], phase diversity, shine intelligence over the further development of this research topic. It is just impossible to list from all aspects. For comparison purpose, two previously mentioned topics in incoherent illumination, namely deconvolution and shift estimation, are briefly described in this section. As a matter of fact, deconvolution is a well-developed research area, which cannot be covered within a few lines.

A.2.1 Deconvolution:

Typical statement of 2D deconvolution problem [Hanisch, 1997; Molina, 2001] is based on Eq. A1:

	$O(x,y) = h(x,y) \otimes S(x,y) + n(x,y)$	(A1)

where $\otimes$ represents convolution operation; $O(x,y)$ stands for the blurred image; $S(x,y)$ stands for the original image; $h(x,y)$ stands for the blur kernel / convolution kernel and $n(x,y)$ stands for noise. The goal of deconvolution is to resolve $S(x,y)$ from $O(x,y)$, by assuming certain distribution of $n(x,y)$. $h(x,y)$ can be either known, partially known or even unknown (in such cases, the problem is named blind deconvolution [Campisi, 2007]).

The difficulty of solving deconvolution problems is mainly due to the mathematical fact that the solution is usually ill-posed: small variations in original conditions may cause evident differences in solutions. Generally speaking, the less pre-knowledge given, the more difficult this problem would be.

Traditional non-iterative solution, for example, can be fulfilled via inverse Winner filtering. Typical drawback for this method is that it will introduce artificial side lobes along sharp edges, which can be alleviated by adding regulation terms (which attenuate the sharpness in the same time) but cannot be eliminated in general. In incoherent imaging applications, such fluctuation may results in negative values, which is physically impossible.

Non-negative solutions can be fulfilled by iterative deconvolution algorithms, which impose non-negative constraints in certain iterative steps. Some famous algorithms, for example, Jansson method [Jansson, 1984] in one dimensional case (for spectrum analysis purpose), is developed in the mid-20th century. In early 1990s, the launch of Hubble space telescope (HST) stimulated an explosive increase in the

application of 2D deconvolution methods, since its imaging optics suffered severe aberration from a manufacturing failure, and was not physically compensated until 3 years later. Many algorithms have been proved successful, including the famous Lucy-Richardson method [Hanisch, 1997].

A large amount of literatures in deconvolution based their method under the Bayesian frame, making different statistical noise assumptions (Gaussian / Poisson, etc.), and turn the problem into maximization searching [Molina, 2001]. However, stability / convergence and artifacts suppression are always key topics in developing deconvolution algorithms. As far as my knowledge goes, deconvolution algorithms are not yet ready for metrology applications, where quantitative accuracy and repeatability are indispensable.

A.2.2 Shift estimation algorithm of sub-pixel level accuracy

Quite a bunch of shift estimation algorithms in incoherent imaging are based on cross power spectrum [Tian, 1986]. Suppose there are two shifted images: $g_1(x,y)$ and $g_2(x,y) = g_1(x-x_0, y-y_0)$, where x_0 and y_0 stands for the shift value of the second image with respect to the first one, then their cross power spectrum:

	$$CC(u,v) = \frac{G_1 G_2^*}{\left|G_1 G_2^*\right|} = \exp[i(x_0 u + y_0 v)]$$	(A2)

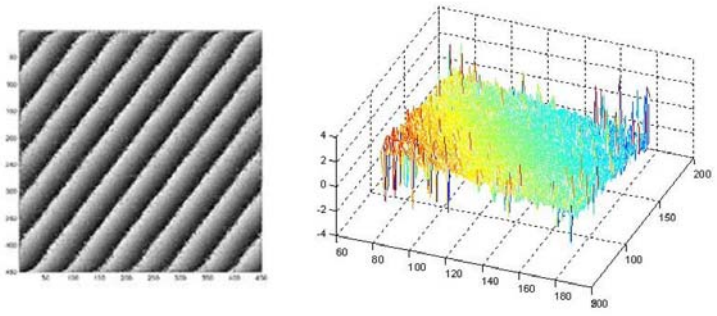

Fig A4 Cross power spectrum of $g_1(x,y)$ and $g_1(x-x_0,y-y_0)$

a) ideal case, integral part of shift x_0 and y_0 can be counted out from the number of cycles along u and v directions, respectively; b) a realistic example, with x_0 and y_0 both smaller than one pixel; outliers due to noise and aliasing error can be observed near the margins.

where G_1 and G_2 are the Fourier transforms of g_1 and g_2, respectively. Ideally, in frequency domain, $CC(u,v)$ should be a wrapped plane whose tilting direction can be derived from x_0 and y_0 (as shown in Fig A4); If inverse transformed back into space domain, $cc(x,y)$ should generate a sharp peak at (x_0,y_0). Earlier algorithms were based on finding the exact peak position of $cc(x,y)$ [Foroosh, 2002]. However, due to image noise and aliasing errors, it is generally difficult to improve the accuracy to sub-pixel level. More sophisticated algorithms focused on finding a plane trend of $CC(u,v)$, and developed a couple of effective solutions, employing mathematics such as singular value decomposition (SVD) [Hoge, 2003], estimation maximization (EM) [Balci, 2006], etc. Frequency domain based algorithms generally can have accuracy as far as sub-pixel level, which satisfies the need of shift estimation for incoherent images.

A.3 Proposed research for sub-pixel resolution enhancement in synthetic 3D map generation

Experiments should be conducted to see whether sub-pixel shifting method can show any potential help to synthetic 3Dt map or not. To begin with, 2 by 2 sub-pixel shifted height maps of some significant target (say, a penny) should be captured and merged directly, without any shift estimation or deblurring post processing. Once any indication of previously unobservable features is now "likely" to be resolved, further development of the method would be worth trying.

For the next step, several topics may worth devoted interest:

- The relationship between surface quality and the efficiency of sub-pixel shift. Besides an indicator to describe surface roughness, the quality of a random shaped surface needs another indicator to tell how far away two successive peaks or valleys locate. In commonly adopted random surface shape scattering model [Beckmann, 1987; Ogilvy, 1987], variation indicator and autocorrelation coefficient are employed for this two purpose, respectively. The effectiveness evaluation of sub-pixel shifting should also be based on random surface scattering modeling. As a start point of this study, complicated secondary or multiple reflection problems can be omitted, as the work should mainly focused on the large scale efficiency rather than detailed accuracy aspect.
- A sophisticated shift estimation algorithm based on synthetic height map / coherent illumination. The purpose of this study is similar to the work proposed

in Chapter 3. However it may be much more challenging, since accuracy to one tenth of a pixel is indispensable, based on noisy and edge destroyed original images. Feasibility of this part should be first verified via simulation and repeatability tests. And then, if viable, the developed algorithm should be tested by real data; if not, shift estimation step should be deducted based on incoherent images purposely captured.

- A deblurring algorithm developed for synthetic 3D map, satisfying metrology purpose. Traditional deconvolution algorithms adopted in 2D imaging may not be the suitable solution in 3D height map for metrology purpose. However, it is interesting to notice that digital holographic refocusing / reconstruction itself is a typical process to remove "blurring effect" of spherical wave-front from the captured hologram. Furthermore, the idea of Fresnelets proposed in [Liebling, 2003] and [Liebling, 2004], although computationally intensive, provides a possibility to decompose complex wave fields into forms that are closely related to digital refocusing. If somehow a mathematical derivation can be proved functional from a metrology point of view, it would be a breakthrough in holographic information processing

A.4 Summary

Possibility of further enhancing lateral resolution of multi-wavelength holographic interferometry via sub-pixel shifting has been discussed. From a metrology point of view, potential academic contributions should be based on both

experimental evidence and theoretical guarantee of accuracy and repeatability.

Reference

[Abe, 2008] Abe, L.; Venet, M.; Enya, K.; Kataza, H.; Nakagawa, T.; Tamura, M. "Multi-stage apodized pupil Lyot coronagraph experimental results" Proceedings of the SPIE - The International Society for Optical Engineering, v 7014, p 701467 (11 pp.), 2008

[Adams, 1998] Adams, M.; Kreis, T.M.; Juptner, W.P.O. "Particle size and position measurement with digital holography" Proceedings of the SPIE - The International Society for Optical Engineering, v 3098, p 234-40, 1997

[Aime, 2002] Aime, C.; Soummer, R.; Ferrari, A. "Total coronagraphic extinction of rectangular apertures using linear prolate apodizations" Astronomy & Astrophysics, v 389, n 1, p 334-44, July 2002

[Aime, 2005] Aime, C. "Radon approach to shaped and apodized apertures for imaging exoplanets" Astronomy & Astrophysics, v 434, n 2, p 785-94, May 2005

[Aizenberg, 2004] Aizenberg, Igor; Butakoff, Constantine "Effective Impulse Detector Based on Rank-Order Criteria" IEEE Signal Processing Letters, v 11, n 3, p 363-366, March 2004

[Aleksoff, 1991] Aleksoff, Carl C.; Ellis, K.K.; Neagle, B.D. "Holographic conversion of a Gaussian beam to a near-field uniform beam" Optical Engineering, v 30, n 5, p 537-43, May 1991

[Aleksoff, 2006] Aleksoff, Carl C. "Multi-wavelength digital holographic metrology" Proceedings of the SPIE - The International Society for Optical Engineering, v 6311, p 63111D-1-7, Aug. 2006

[Almoro, 2007] Almoro, Percival; Garcia, Wilson; Saloma, Caesar "Colored object recognition by digital holography and a hydrogen Raman shifter" Optics Express, v 15, n 12, p 7176-7181, June 11, 2007

[Balci, 2006] Balci, M.; Foroosh, H. "Subpixel estimation of shifts directly in the Fourier domain" IEEE Transactions on Image Processing, v 15, n 7, p 1965-72, July 2006

[Beckmann, 1987] Beckmann, Petr; Spizzichino, Andre "The scattering of

electromagnetic waves from rough surfaces" Artech House, Inc., Norwood, MA, 1987

[Belikov, 2006] Belikov, R.; Kasdin, N.J.; Vanderbei, R.J. "Diffraction-based sensitivity analysis of apodized pupil-mapping systems" Astrophysical Journal, v 652, n 1, pt.1, p 833-44, 20 Nov. 2006

[Born and Wolf, 1999] Born, Max; Wolf, Emil "Principles of Optics" 7th edition, Cambridge University Press, 1999

[Bothe, 1997] Bothe, T.; Burke, J.; Helmers, H.; "Spatial phase shifting in electronic speckle pattern interferometry: minimization of phase reconstruction errors"; Applied Optics, 36, 5310-16, 1997

[Brown, 1990] Brown, R.A.; Burrows, C.J. "On the feasibility of detecting extrasolar planets by reflected starlight using the Hubble Space Telescope" Icarus, v 87, n 2, p 484-97, Oct. 1990

[Bruning, 1974] Bruning, J.H.; Herriott, D.R.; Gallagher, J.E.; Rosenfeld, D.P.; White, A.D.; Brangaccio, D.J. "Digital wavefront measuring interferometer for testing optical surfaces and lenses" Applied Optics, 13, 2693-703, 1974

[Bruning, 1978] Bruning, J. H. "Fringe Scanning Interferometers" in Optical Shop Testing, D. Malacara, Ed. (Wiley, New York, 1978).

[Cady, 2009] Cady, E.; Macintosh, B.; Kasdin, N.J.; Soummer, R. "Shaped pupil design for the Gemini planet imager" Astrophysical Journal, v 698, n 1, p 938-43, 10 June 2009

[Campisi, 2007] Campisi, Patrizio; Egiazarian, Karen "Blind image deconvolution: Theroy and applications" Taylor & Francis Group, LLC, CRC Press, 2007

[Canales, 2009] Canales, Vidal F.; Valle, Pedro J.; Oti, Jose E.; Cagigal, Manuel P. "Pupil apodization for increasing data storage density" Chinese Optics Letters, v 7, n 8, p 720-723, August 2009

[Carl, 2009] D. Carl; M. Fratz; M. Pfeifer; D.M. Giel; H. Höfler. "Multiwavelength digital holography with autocalibration of phase shifts and artificial wavelengths" Appl. Opt., 48, H1-H8(2009)

[Carlotti, 2008] Carlotti, A.; Ricort, G.; Aime, C.; El Azhari, Y.; Soummer, R. "Interferometric apodization of telescope apertures I. First laboratory results obtained using a Mach-Zehnder interferometer" Astronomy and Astrophysics, v 477, n 1, p 329-335, January 2008

[Carre, 1966] P. Carre; "Installation and utilization of photoelectric and interferential comparator of International Bureau of Weights and Measures at Se"

Metrologia, 2, 13-23, 1966 (in French)

[Chakraborty, 2005] Chakraborty, Abhijit; Thompson, Laird A.; Rogosky, Michael "10^{-7} contrast ratio at 4.5/D: New results obtained in laboratory experiments using nanofabricated coronagraph and multi-Gaussian shaped pupil masks" Optics Express, v 13, n 7, p 2394-2402, April 2005

[Chan, 2005] Chan, R.H.; Chung-Wa Ho; Nikolova, M. "Salt-and-pepper noise removal by median-type noise detectors and detail-preserving regularization" IEEE Transactions on Image Processing, v 14, n 10, p 1479-85, Oct. 2005

[Chen, 2008] Chen, Pei-Yin; Lien, Chih-Yuan "An efficient edge-preserving algorithm for removal of salt-and-pepper noise" IEEE Signal Processing Letters, v 15, p 833-836, 2008

[Cheng, 1984] Cheng, Yeou-Yen; Wyant, J.C. "Two-wavelength phase shifting interferometry" Applied Optics, v 23, n 24, p 4539-43, 15 Dec. 1984

[Cheng, 1985] Cheng, Yeou-Yen "Multiple-wavelength phase-shifting interferometry" Applied Optics, v 24, n 6, p 804-7, 15 March 1985

[Choo, 2006] Choo, Y.J.; Kang, B.S. "The characteristics of the particle position along an optical axis in particle holography" Measurement Science & Technology, v 17, n 4, p 761-70, April 2006

[Codona, 2006] Codona, J.L. ; Kenworthy, M.A.; Hinz, P.M.; Angel, J.R.P.; Woolf, N.J. "A high-contrast coronagraph for the MMT using phase apodization: design and observations at 5 microns and 2 λ/D radius" Proceedings of the SPIE - The International Society for Optical Engineering, v 6269, p 62691N-1-10, 2006

[Colomb, 2010] Tristan Colomb; Nicolas Pavillon; Jonas Kühn; Etienne Cuche; Christian Depeursinge; Yves Emery. "Extended depth-of-focus by digital holographic microscopy" Opt. Lett., 35, 1840-1842(2010)

[Cuche, 1999] Cuche, Etienne; Bevilacqua, Frederic; Depeursinge, Christian "Digital holography for quantitative phase-contrast imaging" Optics Letters, v 24, n 5, p 291-293, Mar 1 1999

[Cuong, 2005] Cuong Manh Do; Hong Seung-Hyun; Nomura, T.; Javidi, B. "Multi-wavelength holographic image fusions using discrete wavelet transform" Proceedings of the SPIE - The International Society for Optical Engineering, v 6016, n 1, p 1-6, 9 Nov. 2005

[Cuong, 2007] Cuong Manh Do; Javidi, B. "Multifocus holographic 3-D image fusion using independent component analysis" Journal of Display Technology, v 3, n

3, p 326-32, Sept. 2007

[Daendliker, 1995] Daendliker, Rene; Hug, Kurt; Politch, Jacob; Zimmermann, Eric "High-accuracy distance measurements with multiple-wavelength interferometry" Optical Engineering, v 34, n 8, p 2407-2412, 8 1995

[Debes, 2002] Debes, J.H.; Jian Ge; Chakraborty, A. "First high-contrast imaging using a Gaussian aperture pupil mask" Astrophysical Journal, Letters, v 572, n 2, pt.2, p L165-8, 10 June 2002

[Debes, 2004] Debes, J.H.; Jian Ge "High-contrast imaging with Gaussian aperture pupil masks" Publications of the Astronomical Society of the Pacific, v 116, n 821, p 674-81, July 2004

[Demetrakopoulos, 1974] Demetrakopoulos, T.H.; Mittra, R. "Digital and optical reconstruction of images from suboptical diffraction patterns" Applied Optics, v 13, n 3, p 665-670, Mar 1974

[Dubois, 1999] Dubois, Frank; Joannes, Luc; Legros, Jean-Claude "Improved three-dimensional imaging with a digital holography microscope with a source of partial spatial coherence", Applied Optics, v 38, n 34, p 7085-94, 1 Dec. 1999

[Dubois, 2006] Dubois, Frank; Schockaert, Cédric; Callens, Natacha; Yourassowsky, Catherine "Focus plane detection criteria in digital holography microscopy by amplitude analysis" Optics Express, v 14, n 13, p 61-74, June 26, 2006

[Falaggis, 2009] Falaggis, Konstantinos; Towers, David P.; Towers Catherine E. "Multiwavelength interferometry: extended range metrology", Optics Letters, v 34, n 7, p 950-2, Apr. 2009

[Ferraro, 2005] Ferraro, P.; Grilli, S.; Alfieri, D.; De Nicola, S.; Finizio, A.; Pierattini, G.; Javidi, B.; Coppola, G.; Striano, V. "Extended focused image in microscopy by digital holography" Optics Express, v 13, n 17, Aug. 2005

[Fienup, 1982] Fienup, J.R. "Phase retrieval algorithms: a comparison" Applied Optics, v 21, n 15, p 2758-69, 1 Aug. 1982

[Foroosh, 2002] Foroosh, H.; Zerubia, J.B.; Berthod, M. "Extension of phase correlation to subpixel registration" IEEE Transactions on Image Processing, v 11, n 3, p 188-200, March 2002

[Fung, 1994] Fung, A. K. "Microwave scattering and emission models and their applications" Boston: Artech House, 1994

[Gabor, 1948] Gabor, D. "A new microscopic principle" Nature, v 161, p 777-778, 15 May 1948

[Gass, 2003] J. Gass; A. Dakoff; M.K. Kim. "Phase imaging without 2π ambiguity by multiwavelength digital holography" Opt. Lett.s, 28, 1141-3(2003)

[Gillespie, 1989] Gillespie, J.; King, R.A. “The use of self-entropy as a focus measure in digital holography” Pattern Recognition Letters, v 9, n 1, p 19-25, Jan. 1989

[Goodman, 1996] J.W. Goodman “Introduction to Fourier Optics”, 2nd ed (New York, McGraw-Hill, 1996)

[Goodman, 2006] Goodman, J. W. “Speckle Phenomena in Optics: Theory and Applications” Roberts & Company Publishers, 2006

[Groen, 1985] Groen, F. C.; Young, I. T.; Ligthart, G. “A comparison of different focus functions for use in autofocus algorithms” Cytometry 6, 81-91, 1985

[Guo, 2010] Guo, Lixin; Wang, Rui; Wu, zhensen “Theory and methods of random rough surface scattering”, Beijing: Science Press 2010 (in Chinese)

[Guyon, 2003] Guyon, O. “Phase-induced amplitude apodization of telescope pupils for extrasolar terrestrial planet imaging” Astronomy & Astrophysics, v 404, n 1, p 379-87, June 2003

[Guyon, 2005] Guyon, O.; Pluzhnik, E.A.; Galicher, R.; Martinache, F.; Ridgway, S.T.; Woodruff, R.A. “Exoplanet imaging with a phase-induced amplitude apodization coronagraph. Part I. Principle” Astrophysical Journal, v 622, n 1, pt.1, p 744-58, 20 March 2005

[Guyon, 2006] Guyon, O.; Pluzhnik, E.A.; Kuchner, M.J.; Collins, B.; Ridgway, S.T. “Theoretical limits on extrasolar terrestrial planet detection with coronagraphs” Astrophysical Journal Supplement Series, v 167, n 1, p 81-99, Nov. 2006

[Haddad, 1992] Haddad, W.S.; Cullen, D.; Solem, J.C.; Longworth, J.W.; McPherson, A.; Boyer, K.; Rhodes, C.K. “Fourier-transform holographic microscope” Applied Optics, v 31, n 24, p 4973-8, 20 Aug. 1992

[Hanisch, 1997] Hanisch, R. J.; White, R. L.; Gilliland, R. L.; “Deconvolution of Hubble Space Telescope Images and Spectra” in “Deconvolution of Images and Spectra” Edited by: Jansson, P.A. 2nd edition, Academic Press, CA, 1997

[Hausler, 1972] Hausler, G. “A method to increase the depth of focus by two step image processing” Optics Communications, v 6, n 1, p 38-42, Sept. 1972

[Hoge, 2003] Hoge, W.S. “A subspace identification extension to the phase correlation method [MRI application]” IEEE Transactions on Medical Imaging, v 22, n 2, p 277-80, Feb. 2003

[Hogenboom, 1998] Hogenboom, D.O.; DiMarzio, C.A.; Gaudette, T.J.; Devaney, A.J.; Lindberg, S.C. "Three-dimensional images generated by quadrature interferometry" Optics Letters, v 23, n 10, p 783-5, 15 May 1998

[Howard W. Sams & Co. Engineers, 1975] "Reference data for radio engineers" Howard W. Sams & Co. Engineers INC., 46-7, 1975

[Huang, 2006] Huang, Zhenhua; "3D laser holographic interferometry measurements" Ph.D. Dissertation, Sam. Wu Manufacturing Research Center, University of Michigan, 2006

[Hyvarinen, 2000] Hyvärinen, A.; Oja, E. "Independent component analysis: Algorithms and applications" Neural Networks, v 13, n 4-5, p 411-430, June 2000

[Hyvarinen, 2007] Hyvarinen, A.; Koster, U. "FastISA: a fast fixed-point algorithm for independent subspace analysis" 14th European Symposium on Artificial Neural Networks, ESANN 2006, p 371-6, 2007

[Jacquinot, 1964]Jacquinot, P.; Roizen-Dossier, B. "Apodisation" Progress in Optics, p 31-186, 1964, pt. 3

[Jansson, 1984] P. A. Jansson "Deconvolution with Applications in Spectroscopy" Academic, 1984

[Javidi, 2006] Javidi, B.; Cuong Manh Do; Hong, Seung-Hyun; Nomura, T. "Multi-spectral holographic three-dimensional image fusion using discrete wavelet transform" Journal of Display Technology, v 2, n 4, p 411-17, Dec. 2006

[Jin 2006] Jin, Jonghan; Kim, Young-Jin; Kim, Yunseok; Kim, Seung-Woo; Kang, Chu-Shik "Absolute length calibration of gauge blocks using optical comb of a femtosecond pulse laser" Optics Express, v 14, n 13, p 139-145, June 26, 2006

[Jolliffe, 2002] Jolliffe, I.T.; "Principal Component Analysis" 2nd edition, Springer, 2002

[Kandulla, 2004] J. Kandulla; B. Kemper; S. Knoche; G. von Bally "Two-wavelength method for endoscopic shape measurement by spatial phase-shifting speckle-interferometry" Appl. Opt., 43, 5429-37(2004)

[Kasdin, 2003] Kasdin, N.J.; Vanderbei, R.J.; Spergel, D.N.; Littman, M.G. "Extrasolar planet finding via optimal apodized-pupil and shaped-pupil coronagraphs" Astrophysical Journal, v 582, n 2, pt.1, p 1147-61, 10 Jan. 2003

[Kasdin, 2005] Kasdin, N. Jeremy; Vanderbei, Robert J.; Littman, Michael G.; Spergel, David N. "Optimal one-dimensional apodizations and shaped pupils for planet finding coronagraphy" Applied Optics, v 44, n 7, p 1117-1128, March 1, 2005

[Kebbel, 2001] Kebbel, Volker; Hartmann, Hans-Jürgen; Jüptner, Werner P.O. “Application of digital holographic microscopy for inspection of micro-optical components” Proceedings of SPIE - The International Society for Optical Engineering, v 4398, p 189-198, 2001

[Kemper, 2007] Kemper, B.; Langehanenberg, P.; Bredebusch, I.; Schnekenburger, J.; von Bally, G. “Techniques and applications of digital holographic microscopy for life cell imaging” Proceedings of the SPIE - The International Society for Optical Engineering, v 6633, p 66330D-1-9, 2007

[Kemper, 2009] Kemper, Björn; Kosmeier, Sebastian; Langehanenberg, Patrik; Przibilla, Sabine; Remmersmann, Christian; Stürwald, Stephan; Von Bally, Gert “Application of 3D tracking, LED illumination and multi-wavelength techniques for quantitative cell analysis in digital holographic microscopy” Progress in Biomedical Optics and Imaging - Proceedings of SPIE, v 7184, 2009, Three-Dimensional and Multidimensional Microscopy: Image Acquisition and Processing XVI

[Khmaladze, 2008] Alexander Khmaladze; Myung Kim; Chun-Min Lo. "Phase imaging of cells by simultaneous dual-wavelength reflection digital holography" Opt. Express, 16, 10900-10911(2008)

[Kierkegaard, 1996] Kierkegaard, P. “Reflection properties of machined metal surfaces” Optical Engineering, v 35, n 3, p 845-57, March 1996

[Kim, 1999] M.K. Kim. "Wavelength-scanning digital interference holography for optical section imaging" Opt. Lett., 24, 1693-5(1999)

[Kim, 2000] M.K. Kim. "Tomographic three-dimensional imaging of a biological specimen using wavelength-scanning digital interference holography" Opt. Express, 7, 305-310(2000)

[Kim, 2006] Kim, Taegeun; “Optical sectioning by optical scanning holography and a Wiener filter” Applied Optics, v 45, n 5, p 872-9, 10 Feb. 2006

[Kim, 2009] Kim, Young-Jin; Kim, Yunseok; Chun, Byung Jae; Hyun, Sangwon; Kim, Seung-Woo “Multi-wavelength interferometry based on the frequency comb of a femtosecond laser” 2009 Conference on Lasers & Electro Optics & The Pacific Rim Conference on Lasers and Electro-Optics (CLEO/PACIFIC RIM), p 2 pp., 2009

[Ko, 1991] Ko, Sung-Jea; Lee, Yong Hoon “Center weighted median filters and their applications to image enhancement” IEEE transactions on circuits and systems, v 38, n 9, p 984-993, Sep 1991

[Koliopoulos, 1981] Koliopoulos, C. "Interferometric Optical Phase Measurement Techniques," Ph.D. Dissertation, Optical Sciences Center, U. Arizona 1981

[Kostinski, 2005] Kostinski, Alexander B.; Yang, Weidong “Pupil phase apodization for imaging of faint companions in prescribed regions” *Journal of Modern Optics*, v 52, n 17, p 2467-2474, November 20, 2005

[Kuhn, 2007] Jonas Kuhn; Tristan Colomb; Frédéric Montfort; Florian Charrière; Yves Emery; Etienne Cuche; Pierre Marquet; Christian Depeursinge. "Real-time dual-wavelength digital holographic microscopy with a single hologram acquisition" Opt. Express, 15, 7231-7242(2007)

[Kuhn, 2009] J. Kuhn; F. Montfort; T. Colomb; B. Rappaz; C. Moratal; N. Pavillon; P. Marquet; C. Depeursinge. "Submicrometer tomography of cells by multiple-wavelength digital holographic microscopy in reflection" Opt. Lett., 34, 653-5(2009)

[Kumar, 2008] Kumar, U. Paul; Mohan, N. Krishna; Kothiyal, M.P. “Multiple wavelength interferometry for surface profiling” Proceedings of SPIE - The International Society for Optical Engineering, v 7063, 2008, Interferometry XIV: Techniques and Analysis

[Langehanenberg, 2007] Langehanenberg, P.; Kemper, B.; von Bally, G. “Autofocus algorithms for digital-holographic microscopy” Proceedings of the SPIE - The International Society for Optical Engineering, v 6633, p 66330E-1-9, 2007

[Langehanenberg, 2008] Langehanenberg, Patrik; Kemper, Björn; Dirksen, Dieter; Von Bally, Gert “Autofocusing in digital holographic phase contrast microscopy on pure phase objects for live cell imaging” Applied Optics, v 47, n 19, p D176-D182, July 1, 2008

[Langehanenberg, 2009] Langehanenberg, P.; Ivanova, L.; Bernhardt, I.; Ketelhut, S.; Vollmer, A.; Dirksen, D.; Georgiev, G.; von Bally, G.; Kemper, B. “Automated three-dimensional tracking of living cells by digital holographic microscopy” Journal of Biomedical Optics, v 14, n 1, p 014018 (7 pp.), Jan. 2009

[Lebrun, 2003] Lebrun, D.; Benkouider, A.M.; Coëtmellec, S.; Malek, M. “Particle field digital holographic reconstruction in arbitrary tilted planes” Optics Express, v 11, n 3, p 224-229, February 2003

[Lee, 2009] Lee, Kwangchun; Ryu, Sung Yoon; Kwak, Yoon Keun; Kim, Soohyun; Lee, Yun Woo “Separation algorithm for a 2D refractive index distribution and thickness profile of a phase object by laser diode-based multiwavelength interferometry” Review of Scientific Instruments, v 80, n 5, p 053114 (5 pp.), May 2009

[Lewis, 1994] Lewis, Andrew “Measurement of length, surface form and thermal expansion coefficient of length bars up to 1.5 m using multiple-wavelength

phase-stepping interferometry" Measurement Science and Technology, v 5, n 6, p 694-703, Jun 1994

[Liebling, 2003] Liebling, M.; Blu, T.; Unser, M. "Fresnelets: new multiresolution wavelet bases for digital holography" IEEE Transactions on Image Processing, v 12, n 1, p 29-43, Jan. 2003

[Liebling, 2004] Liebling, Michael; Unser, Michael "Autofocus for digital Fresnel holograms by use of a Fresnelet-sparsity criterion"Journal of the Optical Society of America A: Optics and Image Science, and Vision, v 21, n 12, p 2424-2430, December 2004

[Liu, 2009 (1)] Liu, Jingbo; Song, Xiufa; Huang, Min; Wang, Huaying "Digital holography used for shape measurement of microscopic object" 2009 International Conference on Measuring Technology and Mechatronics Automation (ICMTMA), p 58-61, 2009

[Liu, 2009 (2)] Liu, Jingbo; Song, Xiufa; Han, Rui; Wang, Huaying "Autofocus method in digital holographic microscopy" Proceedings of SPIE - The International Society for Optical Engineering, v 7283, 2009, 4th International Symposium on Advanced Optical Manufacturing and Testing Technologies: Optical Test and Measurement Technology and Equipment

[Lu, 2002] Lu, Sheng-Hua; Lee, Cheng-Chung "Measuring large step heights by variable synthetic wavelength interferometry" Measurement Science & Technology, v 13, n 9, p 1382-7, Sept. 2002

[Luo, 2006(1)] Luo, Wenbin "Efficient removal of impulse noise from digital images"IEEE Transactions on Consumer Electronics, v 52, n 2, p 523-7, May 2006

[Luo, 2006(2)] Luo, W. "An efficient detail-preserving approach for removing impulse noise in images"IEEE Signal Processing Letters, v 13, n 7, p 413-16, July 2006

[Ma, 2004] Ma, Lihong; Wang, Hui; Li, Yong; Jin, Hongzhen "Numerical reconstruction of digital holograms for three-dimensional shape measurement" Journal of Optics A: Pure and Applied Optics, v 6, n 4, p 396-400, April 2004

[MacDonald, 2002] MacDonald, Michael E.; Ryan-Howard, Danette P.; Wack, Edward C. "Pupil apodization as a means of mitigating diffraction effects in remote sensing instruments" Proceedings of SPIE - The International Society for Optical Engineering, v 4483, p 258-268, 2002

[Malkiel, 1999] Malkiel, E.; Alquaddoomi, O.; Katz, J. "Measurements of plankton distribution in the ocean using submersible holography" Measurement Science &

Technology, v 10, n 12, p 1142-52, Dec. 1999

[Mann, 2008] Mann, Christopher J.; Bingham, Philip R.; Paquit, Vincent C.; Tobin, Kenneth W. "Quantitative phase imaging by three-wavelength digital holography" Optics Express, v 16, n 13, p 9753-9764, June 23, 2008

[Martinez, 2007] Martinez, P.; Boccaletti, A.; Kasper, M.; Baudoz, P.; Cavarroc, C. "Optimization of apodized pupil Lyot coronagraph for ELTs" Astronomy and Astrophysics, v 474, n 2, p 671-678, November 2007

[Martinez, 2008] Martinez, P.; Vernet, E.; Dorrer, C.; Carpentier, E.A.; Boccaletti, A.; Kasper, M.; Baudrand, J.; Chaumont, C. "Phase and Lyot-type coronagraphs for the high order testbench: prototyping and first laboratory results" Proceedings of the SPIE - The International Society for Optical Engineering, v 7015, p 70156B (10 pp.), 2008

[Martinez, 2009(1)] Martinez, P.; Dorrer, C.; Aller Carpentier, E.; Kasper, M.; Boccaletti, A.; Dohlen, K.; Yaitskova, N. "Design, analysis, and testing of a microdot apodizer for the Apodized Pupil Lyot Coronagraph" Astronomy and Astrophysics, v 495, n 1, p 363-370, February 2009

[Martinez, 2009(2)] Martinez, P.; Dorrer, C.; Kasper, M.; Boccaletti, A.; Dohlen, K. "Design, analysis, and testing of a microdot apodizer for the apodized pupil Lyot coronagraph (Research Note): II. Impact of the dot size" Astronomy and Astrophysics, v 500, n 3, p 1281-1285, June 2009

[Martinez, 2010] Martinez, P.; Dorrer, C.; Kasper, M.; Boccaletti, A.; Dohlen, K. "Design, analysis, and testing of a microdot apodizer for the apodized pupil Lyot coronagraph: III. Application to extremely large telescopes" Astronomy and Astrophysics, v 520, n 16, October 12, 2010

[Martinez-Corral, 2003] Martínez-Corral, M.; Caballero, M.T.; Pons, A.; Andrés, P "Sidelobe decline in single-photon 4Pi microscopy by Toraldo rings" Micron. 2003;34(6-7):319-25.

[Mc Elhinney, 2005] Mc Elhinney, C.P.; Maycock, J.; Naughton, T.J.; McDonald, J.B.; Javidi, B. "Extraction of three-dimensional shape information from a digital hologram" Proceedings of the SPIE - The International Society for Optical Engineering, v 5908, n 1, p 590805-1-1, 18 Aug. 2005

[Molina, 2001] Molina, R.; Nunez, J.; Cortijo, F.J.; Mateos, J. "Image restoration in astronomy: a Bayesian perspective" IEEE Signal Processing Magazine, v 18, n 2, p 11-29, March 2001

[Montfort, 2006] F. Montfort; T. Colomb; F. Charriere; J. Kuhn; P. Marquet; E.

Cuche; S. Herminjard; C. Depeursinge. "Submicrometer optical tomography by multiple-wavelength digital holographic microscopy" Appl. Opt., 45, 8209-17(2006)

[Nilsson, 1998] Nilsson, Bengt; Carlsson, Torgny E. “Direct three-dimensional shape measurement by digital light-in-flight holography” Applied Optics, v 37, n 34, p 7954-7959, Dec 1 1998

[Nisenson, 2001] Nisenson, P.; Papaliolios, C. “Detection of Earth-like planets using apodized telescopes” Astrophysical Journal, Letters, v 548, n 2, pt.2, p L201-5, 20 Feb. 2001

[Nodes, 1982] Nodes, Thomas A.; Gallagher Jr., Neal C. “MEDIAN FILTERS - SOME MODIFICATIONS AND THEIR PROPERTIES” IEEE Transactions on Acoustics, Speech, and Signal Processing, v ASSP-30, n 5, p 739-746, Oct 1982

[Nouvel, 2004] Nouvel, J.-F.; Herique, A.; Kofman, W.; Safaeinili, A. “Radar signal simulation: Surface modeling with the Facet Method” Radio Science, v 39, n 1, p 162-177, January/February 2004

[Ogilvy, 1987] Ogilvy, J.A. “Wave scattering from rough surfaces” Reports on Progress in Physics, v 50, n 12, p 1553-608, Dec. 1987

[Ogilvy, 1991] Ogilvy, J. A. “Theory of wave scattering from random rough surface” Bristol: Adam Hilger, 1991

[Ozgen, 2004] Ozgen, Mehmet Tankut; Tuncer, Temel Engin “Object reconstruction from in-line Fresnel holograms without explicit depth focusing” Optical Engineering, v 43, n 6, p 1300-1310, June 2004

[Paturzo, 2009] Paturzo, M.; Ferraro, P. “Creating an extended focus image of a tilted object in Fourier digital holography” Optics Express, v 17, n 22, p 20546-52, Oct. 2009

[Pieper, 1983] Pieper, R.J.; Korpel, A. “Image processing for extended depth of field” Applied Optics, v 22, n 10, p 1449-53, 15 May 1983

[Pitas, 1990] Pitas, I.; Venetsanopoulos, A. “Nonlinear Digital Filters: Principles and Applications” Boston, MA: Kluwer, 1990.

[Popescu, 2004] Popescu, Gabriel; Deflores, Lauren P.; Vaughan, Joshua C.; Badizadegan, Kamran; Iwai, Hidenao; Dasari, Ramachandra R.; Feld, Michael S. “Fourier phase microscopy for investigation of biological structures and dynamics” Optics Letters, v 29, n 21, p 2503-2505, November 1, 2004

[Rees, 1990] Rees, W. G.; “Physical Principles of Remote Sensing” Cambridge Univ. Press, New York

[Remmersmann, 2009] Remmersmann, C.; Sturwald, S.; Kemper, B.; Langehanenberg, P.; von Bally, G. “Phase noise optimization in temporal phase-shifting digital holography with partial coherence light sources and its application in quantitative cell imaging” Applied Optics, v 48, n 8, p 1463-72, 10 March 2009

[Rice, 1951] Rice, S.O.. “Reflection of electyromagnetic waves from slightly rough surfaces” Communications on Pure and Applied Mathematics, 4, 351-378, 1951

[Rinehart, 2010] M.T. Rinehart; N.T. Shaked; N.J. Jenness; R.L. Clark; A. Wax. "Simultaneous two-wavelength transmission quantitative phase microscopy with a color camera" Opt. Lett., 35, 2612-14, 2010

[Schodel, 2002] Schodel, R.; Nicolaus, A.; Bonsch, G.; “Phase-stepping interferometry: methods for reducing errors caused by camera nonlinearities”; Applied Optics, 41, 55-63, 2002

[Schnars, 1994(1)] Schnars, U.; Juptner, W. “Direct recording of holograms by a CCD target and numerical reconstruction” Applied Optics, v 33, n 2, p 179-81, 10 Jan. 1994

[Schnars, 1994(2)] Schnars, Ulf “Direct phase determination in hologram interferometry with use of digitally recorded holograms” Journal of the Optical Society of America A: Optics and Image Science, and Vision, v 11, n 7, p 2011-2015, July 1994

[Schnars, 2002] Schnars, U.; Juptner, W.P.O. “Digital recording and numerical reconstruction of holograms” Measurement Science & Technology, v 13, n 9, p R85-101, Sept. 2002

[Schwider, 1983] Schwider, J.; Burow R.; Elssner, K.-E.; Grzanna, J.; Spolaczyk, R.; Merkel, K. "Digital Wave-Front Measuring Interferometry: Some Systematic Error Sources," Appl. Opt. 22, 3421 1983.

[Sivaramakrishnan, 2008] Sivaramakrishnan, A.; Soummer, R.; Pueyo, L.; Wallace, J.K.; Shao, M. “Sensing phase aberrations behind Lyot coronagraphs” Astrophysical Journal, v 688, n 1, p 701-8, 20 Nov. 2008

[Srinivasan, 2007] Srinivasan, K.S.; Ebenezer, D. “A new fast and efficient decision-based algorithm for removal of high-density impulse noises” IEEE Signal Processing Letters, v 14, n 3, p 189-92, March 2007

[Sun, 2004] Sun, Y.; Duthaler, S.; Nelson, B. J. “Autofocusing in computer microscopy: selecting the optimal focus algorithm” Microsc. Res. Tech. 65, 139-149, 2004

[Tachiki, 2008] Tachiki, M.L.; Itoh, M.; Yatagai, T. “Simultaneous depth determination of multiple objects by focus analysis in digital holography” Applied Optics, v 47, n 19, p D144-53, 1 July 2008

[Tanner, 1976] Tanner, L.H.; Fahoum, M. “A study of the surface parameters of ground and lapped metal surfaces, using specular and diffuse reflection of laser light” Wear, v 36, n 3, p 299-316, March 1976

[Thelen, 2005] Thelen, Andrea; Bongartz, Jens; Giel, Dominik; Frey, Susanne; Hering, Peter “Iterative focus detection in hologram tomography” Journal of the Optical Society of America A: Optics and Image Science, and Vision, v 22, n 6, p 1176-1180, June 2005

[Tian, 1986] Tian, Qi; Huhns, Michael N. “ALGORITHMS FOR SUBPIXEL REGISTRATION” Computer vision, graphics, and image processing, v 35, n 2, p 220-233, Aug 1986

[Tridhavee, 2004] Tridhavee, T.M.; Santhanam, B.; Brueck, S.R.J. “Optimization and apodization of aerial images at high NA in imaging interferometic lithography” Proceedings of the SPIE - The International Society for Optical Engineering, v 5377, n 1, p 1544-54, 2004

[Towers, 2004] Towers, Catherine E.; Towers, David P.; Jones, Julian D. C. “Generalized frequency selection in multifrequency interferometry” Optics Letters, v 29, n 12, p 1348-50, 15 June 2004

[Ulaby, 1982] Ulaby, F. T.; Moore, R. K.; Fung, A. K.; “Microwave Remote Sensing” Vols. 1 & 2, Artech House, Norwood, Mass.

[Vanderbei, 2003a] Vanderbei, R.J.; Spergel, D.N.; Kasdin, N.J. “Spiderweb masks for high-contrast imaging” Astrophysical Journal, v 590, n 1, pt.1, p 593-603, 10 June 2003

[Vanderbei, 2003(2)] Vanderbei, R.J.; Spergel, D.N.; Kasdin, N.J. “Circularly symmetric apodization via star-shaped masks” Astrophysical Journal, v 599, n 1, pt.1, p 686-94, 10 Dec. 2003

[Voronovich, 1985] Voronovich, A.G. “Small-slope approximation in wave scattering by rough surfaces” Soviet Physics – JETP, 62, 1985

[Wang, 2009] Wang, Huaying; Qin, Aili; Huang, Min “Autofocus method for digital holographic reconstruction of microscopic object” 2009 Symposium on Photonics and Optoelectronics, p 4 pp., 2009

[Wang, 2010] Wang, Fei; Zhang, Xin-Liang; Yu, Yu; Huang, Xi “82-channel

multi-wavelength comb generation in a SOA fiber ring laser" Optics and Laser Technology, v 42, n 2, p 285-8, March 2010

[Wu, 1972] Wu, S.T.; Fung, A.K.. "A noncoherent model for microwave emissions and backscattering from the sea surface" Journal of Geophysical Research, 77, 5917-29, 1972

[Xu, 2007] Xu, Li; Yang, Huaidong; Chen, Kexin; Tan, Qiaofeng; He, Qingsheng; Jin, Guofan "Resolution enhancement by combination of subpixel and deconvolution in miniature spectrometers" Applied Optics, v 46, n 16, p 3210-3214, June 1, 2007

[Xu, 2011] Xu, Li; Mater, Mike; Ni, Jun; "Focus detection criterion for refocusing in multi-wavelength digital holography", Optics Express, 19, 14779-14793 2011

[Xu, 2012(1)] Xu, Li; Aleksoff, Carl C.; Ni, Jun; "High precision 3D shape reconstruction via digital refocusing in multi-wavelength digital holography" accepted by Applied Optics, 2012

[Xu, 2012(2)] Xu, Li; Aleksoff, Carl C.; Mater, Mike; Ni, Jun; "Pupil apodization in multi-wavelength digital holographic metrology" Submitted, to Optics Letters, 2012

[Yamaguchi, 1997] Yamaguchi, Ichirou; Zhang, Tong "Phase-shifting digital holography" Optics Letters, v 22, n 16, p 1268-1270, Aug 15 1997

[Yamaguchi, 2001] Yamaguchi, Ichirou; Kato, Jun-ichi; Ohta, Sohgo; Mizuno, Jun "Image formation in phase-shifting digital holography and applications to microscopy" Applied Optics, v 40, n 34, p 6177-6186, Dec. 2001

[Yamaguchi, 2006] Yamaguchi, Ichirou; Ida, Takashi; Yokota, Masayuki; Yamashita, Kouji "Surface shape measurement by phase-shifting digital holography with a wavelength shift" Applied Optics, v 45, n 29, p 7610-7616, October 10, 2006

[Yang, 2004] Yang, W.; Kostinski, A.B. "One-sided achromatic phase apodization for imaging of extrasolar planets" Astrophysical Journal, v 605, n 2, pt.1, p 892-901, 20 April 2004

[Yang, 2007] Yang, Yan; Kang, Bo-seon; Choo, Yeon-jun "Focal plane location in digital holography" Proceedings of the SPIE - The International Society for Optical Engineering, v 6723, n 1, p 672365-1-6, 3 Dec. 2007

[Yang, 2008] Yang, Yan; Kang, Bo-seon; Choo, Yeon-jun "Application of the correlation coefficient method for determination of the focal plane to digital particle

holography" Applied Optics, v 47, n 6, p 817-24, 20 Feb. 2008

[Yu, 2001] Yu, Lingfeng; Cai, Lilong "Iterative algorithm with a constraint condition for numerical reconstruction of a three-dimensional object from its hologram" Journal of the Optical Society of America A (Optics, Image Science and Vision), v 18, n 5, p 1033-45, May 2001

[Yu, 2009] Yu, Lingfeng; Chen, Zhongping "Multi-wavelength digital holographic tomography based on spectral interferometry" Proceedings of the SPIE - The International Society for Optical Engineering, v 7184, p 71840P (5 pp.), 2009

[Yu, 2011] Hao Yu; Carl Aleksoff; Jun Ni; "A multiple height transfer interferometric technique" Opt. Express, 19, 16365-10374, 2011

[Zhang, 1998] Zhang, Tong; Yamaguchi, Ichirou "Three-dimensional microscopy with phase-shifting digital holography" Optics Letters, v 23, n 15, p 1221-1223, Aug. 1998

[Zhang, 2002] Zhang, Shuqun; Karim, M.A. "A new impulse detector for switching median filters" IEEE Signal Processing Letters, v 9, n 11, p 360-3, Nov. 2002

[Zhang, 2008] Zhang, Xin; Lam, E.Y.; Poon, Ting-Chung "Reconstruction of sectional images in holography using inverse imaging" Optics Express, v 16, n 22, p 17215-26, 2008

[Zhang, 2009] Zhang, Xin; Lam, E.Y.; Kim, Taegeun; Kim, You Seok; Poon, Ting-Chung "Blind sectional image reconstruction for optical scanning holography" Optics Letters, v 34, n 20, p 3098-100, 15 Oct. 2009

[Zou, 1996] Yunlu Zou; G. Pedrini; H. Tiziani. "Surface contouring in a video frame by changing the wavelength of a diode laser" Opt. Engineering, 35, 1074-9 (1996)